Chain dynamics in complex polymer architectures probed by rheology and NMR

Dissertation

zur Erlangung des Doktorgrades der Naturwissenschaften
(Dr. rer. nat.)

der
Naturwissenschaftlichen Fakultät II
Chemie, Physik und Mathematik

der Martin-Luther-Universität
Halle-Wittenberg

vorgelegt von

Farhad Shahsavan

geboren am 21. Mai 1988 in Teheran

Erstgutachter: Prof. Dr. Kay Saalwächter

Zweitgutachter: Prof. Dr. Mario Beiner

Drittgutachter: Prof. Dr. Manfred Wilhelm

Tag der öffentlichen Verteidigung: 07.11.2023

Table of Contents

1. Introduction

Polymers have existed on this planet since the beginning of life as they form the basis of life. Nevertheless, the first synthetic polymer, nitrocellulose, was discovered by Christian Frederick Schönbein in 1846 and was first produced from natural cellulosic material by Alexander Parkes in 1862. The commercial production of polymer materials started with the second synthetic plastic, developed by Dr. Leo Baekeland in 1907 and commercially produced in 1910. In the 1930s and 1940s, the development of new polymers speeded up, and some other polymers, such as Polyvinylchloride (PVC), polystyrene, and polyethylene, were discovered in this period [1–3]. During this time, the main focus was on the chemical composition of these materials, and the molecular structure remains unregarded.

Meanwhile, the German chemist Hermann Staudinger introduced his theory which considered polymer materials as giant molecules and used the word, *macromolecule,* to express them [4–6]. A better understanding of the polymer molecular structure as a consequence of Staudinger's theory resulted in a growing number of commercialized polymeric products between 1925-1950. In March 1933, ethylene was polymerized unintentionally by Eric Fawcett and Reginald Gibson for the first time at high temperature and under high pressure. Then the commercial production of Polyethylene (PE) started in 1938. Two main types of polyethylene exist, High-density polyethylene (HDPE), a linear polymer with a low number of branches, and low-density polyethylene (LDPE), a branched polymer with a high number of branches. With 100 million tons of annual production (in 2018) and over 31% of the global plastic market share, polyethylene is "the world's leading synthetic macromolecule" [7,8]. Due to the importance of PE, it is the main focus of the current thesis.

The word *polymer* is a Greek word that means many parts. A polymer is a set of repeated chemical units (monomers) connected end to end via covalent bonds. The chemical units can include the same type, named homopolymer, or possibly different types, named copolymer. The number of monomers that form a polymer chain is called the degree of polymerization and defines the length of a polymer chain. This

length can be expressed by molecular weight that equals to $M_0 \times N$. M_0 and N are the monomer molecular weight and degree of polymerization, respectively. The final polymeric product's properties are defined not only by the chemical nature of the monomers but even by the degree of polymerization.

The polymer materials can be categorized diversely based on the different classification types. In this work, according to our demand, we categorize polymers based on chain structure into linear, branched, star-shaped, and network. Figure 1.1 depicts a schematic representation of these kinds of chain structures.
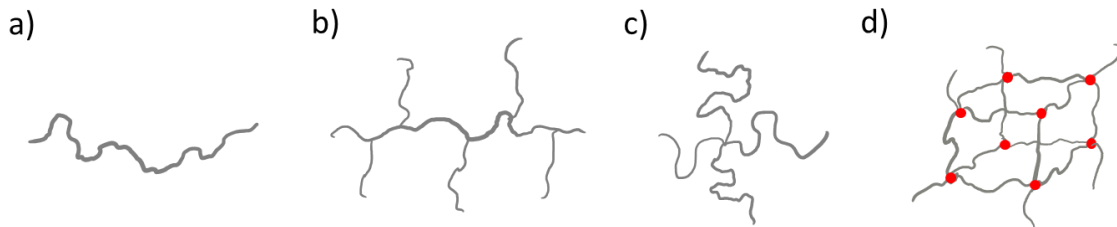
Figure 1.1: Different forms of a polymer chain, a) linear polymer, b) branched polymer, c) star polymer, d) polymer network (the mentioned network structure is not the actual structure, but due to the limitations, it is depicted in this manner. According to the definition, the shortest path to returning to a crosslink should contain many crosslinks.)

After Staudinger's well-known macromolecular hypothesis, the basics of polymer physics, including the size of the macromolecules, thermodynamics, and behavior of a polymer chain in good and theta solvents, rubber elasticity, single polymer chain dynamics, and the tube model were introduced [9–12]. Via expanding knowledge about polymer physics, polymer scientists have been capable of tuning the physical and mechanical properties without changing the chemical nature of polymers. Among the modification approaches, forming the cross-links between polymer chains to make a three-dimensional network is highly used in the rubber and polyolefins industries.

The cross-linking of high-molecular-weight PE chains via high-energy irradiation was first reported from changes in the stress- strain behavior of the PE samples after being irradiated in the heavy water pile of the Argonne National Laboratory near Chicago in 1947. The crosslinks were produced in the semi-crystalline state at

room temperature without making any changes in the shape of the samples [13]. It was also deduced that the final product has a memory effect [14], which means it keeps and recovers its permanent shape. Beyond the shape memory effect (SME) [15–17], crosslinking of PE enhances the mechanical properties and prevents the undesirable hot flow (flowing of PE in high-temperature usage) and cold flow (creep) [18–20]. Due to this property, cross-linked PE is highly used in power cable insulation [21–23], piping [24–26], the automobile industry [7], and medical implants [27–30].

Cross-linking of PE can be carried out via a peroxide agent [31–38] or silane grafting [39–46] or by using the electron-induced reactive process (EIReP) [14,47–51]. Since no chemical agent is used in the irradiation technique, it is a clean and practical approach that can be used for the specimens at room temperature and molded parts.

The relevent architectures of crosslinked PE via irradiation are shown in figure 1.2. In the first stages of irradiation, some branched and star polymers are produced by irradiation, whereas in the final stages, these structures connect and form the final network. In the final product, the system contains a mixture of a network structure, star, branched and linear polymers.

a)   b)   c)   d)
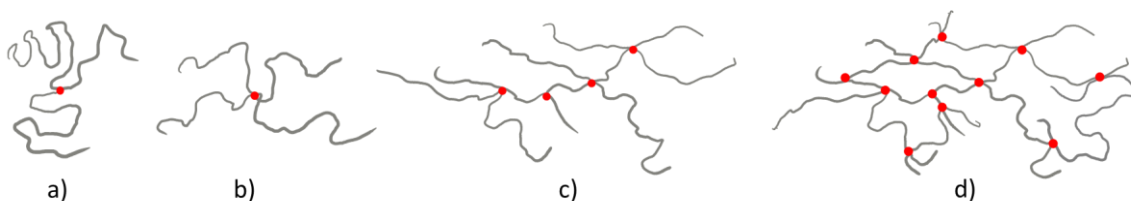
Figure 1.2: possible chain structures of PE produced by irradiation. According to reactions 1.4, 1.5, after irradiation, different types of polymer chain structures can be produced in the system, including (a) a three-arm star polymer (by a CH_2 radical), (b) a four-arm star polymer, (c) a branched polymer, (d) a polymer network. It is noted that in the first steps, three-arm or four-arm star polymers are produced. Then via producing more radicals, they turn into the branched polymer and eventually a polymer network

Although the gel content measurement is the most common method to probe the efficiency of the cross-linking process in this class of materials [52–54], swelling tests based on the Flory-Rehner theory [55,56], mechanical measurements based on

the rubber elasticity [20,57] and dynamic mechanical measurements based on the gelation theories [58–64] are also used to investigate the network structure. Due to difficulties of the current approaches, like safety issues and the precision of the obtained parameters, finding an alternative approach is of interest to the current research.

In addition to probing the network structure for studying the crosslinking efficiency, investigation of the entangled defects like branched polymers (see figure 1.2) can be practical. Incorporating some concepts such as constraint release, primitive path fluctuations, branch-arm retraction, and dynamic tube dilation (DTD) into the original tube model has enabled to predict of the rheological properties of the monodisperse star [65–68], comb [69–72], H [73,74] and Cayley-tree polymers [75–77] and even some polymer blends [78–80]. According to the DTD model, a relaxed segment is considered an effective theta solvent, and by its dilution effect, the remaining segments move in a dilated tube.

As well as the macroscopic properties expressed in mentioned methods, network structure can be probed in terms of molecular dynamics via solid-state NMR. One of the first works in probing crosslinking in chemically crosslinked PE was done by Jurkiewicz al. [81], measuring the proton spin-lattice relaxation time. His method is an indirect qualitative measurement of the chain dynamics based on changes in the overall time scale and conformational restrictions of fast segmental fluctuations. Orientation-dependent nature of the dipolar coupling interaction between neighboring protons provides the opportunity for a direct study of chain dynamics due to access to the anisotropy of segmental motions of the constrained chains. An averaged residual dipolar coupling (D_{res}), appearing as a result of the fast anisotropic motions, is proportional to the inverse number of segments between two topological constraints [82,83]. D_{res} and its distribution can be measured precisely via time-domain double-quantum (DQ) NMR to study the network structure and defects in the rubbers and hydrogels [84–87]. In more general studies for the case of monodisperse polymer melts [88–91] and transient networks [92,93], DQ NMR has been used to probe the segmental dynamics in terms of orientation auto-correlation function (OACF) of the second Legendre polynomial $C(t) = 5 < P_2(\cos\theta(t +$

τ))P$_2$(cos$\theta(t)$)>, where θ represents the instantaneous segmental orientation with respect to the magnetic field.

The demand for precise microscopic access to chain dynamics in more complex architectures of polymers, particularly partially crosslinked PE and polymer comb for which the DQ NMR is applied for the first time, is the primary motivation of the given thesis. In this work, we intend to introduce DQ NMR as the molecular rheology tool of choice for complex polymer architecture by establishing consistency between DQ NMR results and rheological measurements. We also look for a replacement for the classical experiments relying on hazardous solvents at high temperatures, such as gel content and swelling test. This research also focuses on understanding comb-polymer chain dynamics and the DTD model's interpretation in the NMR-based OACF.

The given thesis is structured as follows. In chapter 2, the polymer chain conformation and the basics of the polymer chain size are presented. In the following, rubber elasticity, the Rouse motion, and reptation as part of the tube model are discussed. In the final part, the tube model for branched polymers and gelation in dynamic-mechanical tests are reviewed. The theories and basics of solid-state NMR and all used NMR techniques are explained in detail in chapter 3. In this chapter, the OACF and its importance in the DQ NMR will be introduced. Afterward, the different forms of OACF function and interpretation of the DTD model in DQ NMR measurements will be discussed. The experimental details about the samples and used techniques are described in chapter 4. The experimental results of studying the irradiated HDPEs (key results are published in Ref. [94]) and PI-comb via rheology and DQ NMR technique are discussed in chapters 5 and 6, respectively. In chapter 7, a summary, conclusion, and outlook of the current work will be presented.

2. Polymer chains: properties and motions

2.1. Single-chain conformations

A polymer material is an aggregation of high molecular-weight polymer chains composed of many connected low-molecular-weight units called monomers. In order to understand the macroscopic properties of the polymer materials, it is necessary to have a clear picture of single-chain dynamics. Although the monomers within a polymer chain interact with each other, the essential starting point of most models in polymer dynamics is the conformation of an ideal chain, with no interaction between the monomers. Let us consider a polyethylene molecule as an example (figure 2.1). There are two types of motions within a molecule. The first group of motions includes changes in valance angles and bond lengths during molecular vibrations in high frequencies and does not affect the overall form of the molecule. The second group concerns the rotational motions around C-C bonds, which have the potential to change the form of the molecule. For example, a transition between different conformational states can lead to a conversion of planar molecular form into a coil [95]. The rotational angle of bond i is defined as the angle between two planes, including the plane defined by bonds i-2 and i-1 and the one defined by bonds i-1 and i. Three possible states can be defined based on the potential energy level (figure 2.1). Trans state is the planar zigzag conformation with the lowest energy level where the rotational angle is zero. Gauche+ and gauche- states are defined for the rotational angle of ±120°.
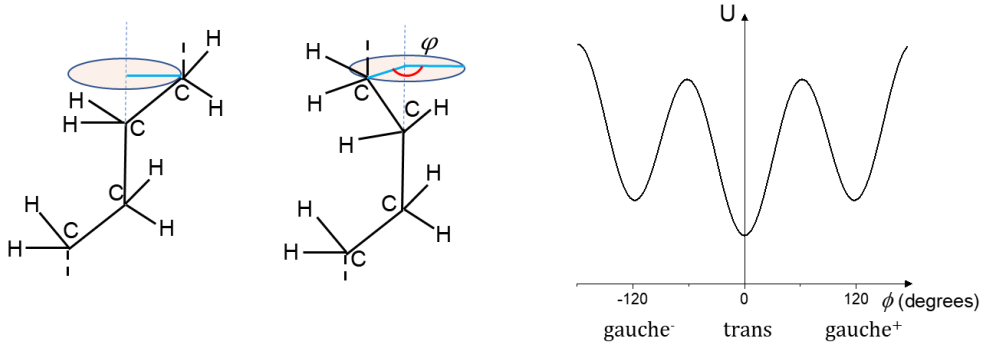
Figure 2.1: The potential energy associated with rotational motion around the C-C bond. According to the minima in the potential energy, three possible states, including trans (0°), gauche+ (+120°), and gauche- (-120°), can be occupied by the bonds.

A polymer chain with n bonds has the longest possible end-to-end distance only if all rotational angles of the whole chain are in trans conformation. This maximum end-to-end distance which is called contour length can be written as

$$R_{max} = nl \cos\frac{\theta}{2}, \tag{2.1}$$

where l and θ are the bond length and the angle between neighboring bonds, respectively. In a polymer chain with n bonds oriented freely to each other, the end-to-end vector is zero because their orientations are statistically independent. Thus, to explain the size of such a polymer chain, we use the mean-square end-to-end distance [96]:

$$\langle R^2 \rangle = \sum_{i=1}^{n}\sum_{j=1}^{n} \langle \vec{r}_i \cdot \vec{r}_j \rangle = \sum_{i=1}^{n} \langle \vec{r}_i^2 \rangle + 2l^2 \sum_{i=1}^{n-1}\sum_{j=i+1}^{n} \langle \cos\theta_{ij} \rangle = nl^2 + 2l^2 \sum_{i=1}^{n-1}\sum_{j=i+1}^{n} \langle \cos\theta_{ij} \rangle \tag{2.2}$$

In the case of a freely jointed chain, the second term would be zero, but in real polymer chains, as c-c bonds can only occupy the positional orientation with solid angle $d\theta$, $\langle \cos\theta_{ij} \rangle \neq 0$. Therefore, the second term can represent a deviation from freely jointed behavior by defining the characteristic ratio C_∞. The mean-square end-to-end distance can be approximated for long chains:

$$\langle R^2 \rangle \cong C_\infty n l^2 \tag{2.3}$$

The characteristic ratio depends on the local stiffness of the polymer chain and ranges from 4 to 12 for typical polymers. Via defining the effective bond length as $l_k^2 = C_\infty l^2$, which is called Kuhn length, and N as the number of freely jointed effective bonds; the modified chain can be assumed as a freely jointed chain. The mean square end-to-end distance and contour length can be written as:

$$R_{max} = N l_k \tag{2.4}$$

$$\langle R^2 \rangle = n l_k^2 \tag{2.5}$$

The Kuhn model assumes that Kuhn segments take all orientations randomly, thus the mean square end-to-end distance change continuously and can be described by a Gaussian distribution function $P(R, N)$ according to the central limit theorem:

$$P(R, N) = \left(\frac{3}{2\pi N l^2} \right)^{\frac{3}{2}} \exp\left(\frac{3R^2}{2N l^2} \right) \tag{2.6}$$

This distribution is only valid for the end-to-end distance much shorter than the maximum extension of the polymer chain. For real chains, $P(N, R) = 0$ for $R > Nb$, whereas the distribution function provides a non-zero probability in such a case. The self-similarity characteristic of polymer chains can be derived from the possibility of rescaling a freely jointed chain. Self-similarity means, independent of the chosen length, any part of the polymer chain exhibits the same internal structure, and internal distance vectors follow a Gaussian distribution [95].

2.2. Crystallization in polymers

Polymer chains can form crystalline structures by orienting themselves parallel to other chains in a regular and fixed low-energy conformation (helical, all-trans for PE). This ability, being much reduced in polymers with non-regularity of structure, such as polymers with side chains and heteropolymers with random sequence configuration, can provide some characteristic properties for a polymer material.

Since the formation of crystalline structure reduces the entropy significantly, from the thermodynamic aspect of view, this structure can be formed at lower temperatures (below the melting point). The kinetics of crystallization is governed by nucleation and growth processes. The transport term of the growth process is governed by chain mobility and correlates with temperature, whereas the nucleation process is proportional to the inverse of temperature. Accordingly, the crystallization of a polymer system at low temperatures is governed by nucleation, while at high temperatures, the transport process becomes dominant [97,98].

In this chapter, from now on, we focus on the dynamics of the polymer chains in the molten state.

2.3. Rubber elasticity

Although the trans-state is an energetically favorable state (for PE), it reduces the number of available conformations in a chain and, consequently, the entropy. In a stretched chain, an entropic nature retractive force rises to keep the chain ends in the unperturbed state (recoiling). This phenomenon, called rubber elasticity, is discussed in both cases of a single chain extension and a polymer network. In the case of a Gaussian chain, the external force f required to keep the ends of a polymer chain at a fixed distance of R is given by

$$f = \frac{3kT}{R_0{}^2} \Delta R \; . \tag{2.7}$$

Here, R_0, $\Delta R (=R\text{-}R_0)$, T, and k are the mean-squared end-to-end distance of the unperturbed chain, the magnitude of extension, the temperature, and the Boltzmann constant, respectively. This equation shows the linear relation of the force with the distance between two chain ends which reminds one of Hooks law for springs. The temperature dependency of the elastic force demonstrates its entropic nature.

On the macroscopic scale, polymer networks can be assumed to be a large group of chains fixed by cross-links. The affine network model is the simplest in rubber

elasticity that assumes the relative deformation of each network strand is equal to the macroscopic relative deformation. Based on this model, the stress exerted on the rubber material upon uniaxial stretching can be written as [95]

$$\sigma_{eng} = nRT \left(\lambda - \frac{1}{\lambda^2} \right), \tag{2.8}$$

where n is the number of crosslinks per volume, R is the gas constant, and λ is the extension ratio. This equation is only valid for an incompressible Gaussian polymer chain network with affine deformation and fixed cross-links. Consequently, the shear modulus can be obtained as

$$G = \frac{\rho RT}{M_c}. \tag{2.9}$$

Here, ρ is the polymer network density, and M_c is the number-average molar mass between two crosslinks.

In real polymer networks, the crosslinks are not fixed in space, and also entanglements can carry some load. These two aspects are not reflected in the affine network's assumptions and make it an unrealistic model. Other models, such as the phantom model, should be employed for a more realistic description.

2.4. Rouse model

As explained in the rubber elasticity part, when a polymer chain deforms from its coiled conformation, an entropic force pulls back the polymer segments and returns them to the initial coiled form. This force is linearly dependent on the extension amount and can be simulated by an extended spring. Moreover, when a polymer segment in a melt starts moving through the surroundings, set up by other chains, every monomer experiences a frictional force. In order to simplify the motion of the segments, Rouse [99] considered the polymer chain as a set of beads connected via springs (figure 2.2) and then developed the first successful molecular model of polymer dynamics. In this model, beads and springs represent frictional and elastic forces, respectively. A polymer chain is subdivided into N Rouse sequences which

are sufficiently long to obey the Gaussian chain statistics. Each sequence is characterized by its friction coefficient ξ, and the total friction coefficient of the whole Rouse chain is

$$\xi_R = N\xi .$$

<div align="right">(2.10)</div>

The time that a polymer chain needs to diffuse a distance of the order of its size is called Rouse time τ_R:

$$\tau_R = \frac{R^2}{D_R} = \frac{R^2}{3\pi^2 \frac{kT}{N\xi}} = NR^2 \frac{\xi}{3\pi^2 kT}$$

<div align="right">(2.11)</div>

R^2 is the mean-squared end-to-end distance, and D_R is the diffusion coefficient of the Rouse chain obtained from the Einstein relation. By replacing $R \approx bN^{1/2}$, the Kuhn segment relaxation (shortest relaxation time) and the whole chain relaxation time (longest relaxation time) of an ideal chain can be written as

$$\tau_0 = \frac{\xi b^2}{3\pi^2 kT} ,$$

<div align="right">(2.12)</div>

$$\tau_R = \tau_0 N^2 .$$

<div align="right">(2.13)</div>
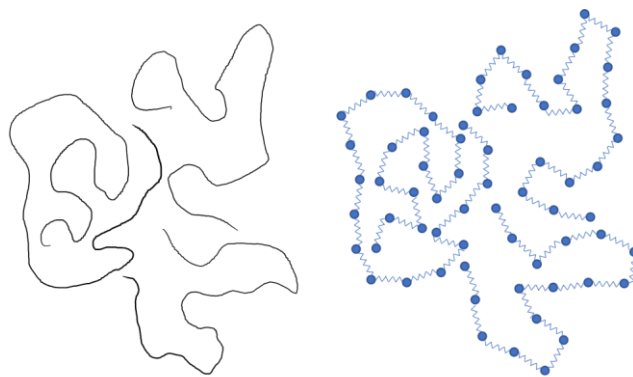
Figure 2.2: In the Rouse model, a chain of N monomers is considered a chain of N beads connected by springs.

According to the self-similarity of the polymer chains, the relaxation of an unentangled chain can be described by different relaxation modes, which are assigned by mode index p = 1, 2, 3, ..., N. These mode indices demonstrate the number of subdivided chains in the relaxation mode. For example, p=1 is the relaxation mode of the whole chain, and p=N refers to the relaxation of a single Kuhn segment (τ_0). Since the pth mode consists of N/p segments, the relaxation time of the pth mode is similar to the relaxation time of a chain with N/p segments:

$$\tau_p = \tau_0 \left(\frac{N}{p}\right)^2 \tag{2.14}$$

In p^{th} mode, the whole chain is divided into p sections, and each relaxes independently. From the definition of the Rouse time, one can conclude that the mean-square displacement of a chain section with N/p monomer is proportional to the size of a chain with N/p monomers, which equals $b(N/p)^{1/2}$. The following relation can be written:

$$\langle [\vec{r}_j(t) - \vec{r}_j(0)]^2 \rangle \approx b^2 \left(\frac{t}{\tau_0}\right)^{1/2} \text{ for } \tau_0 < t < \tau_R \tag{2.15}$$

This relation expresses that the motion on a faster time scale than the Rouse time is sub-diffusive and has an exponent of 0.5, whereas, for a diffusive motion, the mean square displacement must be linear in time [100].

Also, for the stress relaxation modulus, the following equation was derived by Rouse:

$$G(t) = kT \frac{\varphi}{Nb^3} \sum_{p=1}^{N} \exp\left(-t/\tau_p\right) \tag{2.16}$$

2.5. Tube model

The Rouse model expressed the chain motions in unentangled polymers, assuming chain motion is not hindered by the existence of other chains. In high molecular weight polymers, chains start interpenetrating each other and pose constraints. The

constraints arise from the nature of the polymer chains, which are one-dimensional connected objects and cannot cross each other. The constraints impose restrictions on polymer motions, it is thus impossible for a polymer chain to move freely. Thus, the free diffusion that the Rouse model suggests after Rouse time (the longest Rouse mode) is unrealistic in high MW polymers.

The entanglement time τ_e, is defined as the Rouse time of an entanglement strand with N_e segments. After this time, chain motions affected by the imposed constraints and in very high molecular weight polymers lead to a rubber-elastic plateau in time or frequency-dependent mechanical response functions.

de Genes and Edwards [10,11] suggested considering the motion of a single-chain polymer within a confining tube. The tube is defined by the spatial constraints imposed by the surrounding polymer chains, and its diameter is assumed $a = N_e b^2$. Along the tube, the polymer chain can diffuse by reptation, like a snake or a worm.
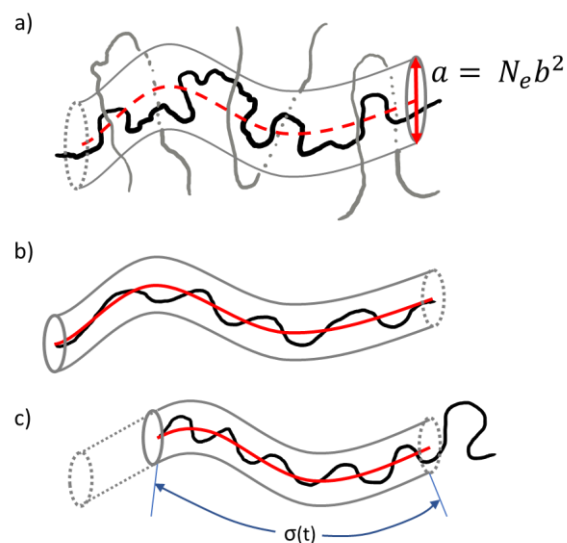
Figure 2.3: schematic representation of tube model. a) The entangled chain is constrained by a hypothetical confining tube formed by the surrounding chains. As it is seen, the tube diameter is proportional to the entanglement spacing (N_e), and the primitive path is assigned with the red dashed line. b) The initial conformation of the chain in the confining tube. c) Effect of the motion of the chain into the right-hand side, where parts of the chain leave the initial tube. The empty parts of the tube left by the chain disappear (be assigned by a dotted line). The length of the remaining tube is denoted by $o(t)$, being a function of time which correlates with the tube survival probability, $\psi(t)$.

For understanding the reptation motion, let's assume a single chain moving within a fixed tube. The reptation can be considered as a Rouse motion of a chain consisting of N segments with length b with the friction constant of ξ in the tube imposed by the entanglements. The primitive path (primitive chain) is defined as the shortest path connecting the two chain ends with the same topology of the confined tube (figure 2.3). On short time scales, the polymer chain motion is a rapid wriggling around the primitive path, which is negligible. On longer time scales, the motion can be described by the time-dependent evolution of the primitive path. Since the motion of the primitive chain is analogous to the overall translational of the Rouse chain along the tube, the curvilinear diffusion coefficient D_c can be written as the diffusion coefficient of a Rouse chain [100]:

$$D_c = \frac{kT}{N\xi} \tag{2.17}$$

The reptation time is defined as the time takes for a chain to escape from its original tube. For this purpose, the chain needs to diffuse the distance equal to the contour length of the original primitive path, which is

$$\langle L \rangle \approx \frac{Nb^2}{a} \approx \frac{bN}{\sqrt{N_e}}, \tag{2.18}$$

where a is the step length size of the primitive chain and equals the size of a chain with N_e monomers. The reptation time can be found as:

$$\tau_{rep} \approx \frac{L^2}{D_c} \approx \frac{\xi b^2}{kT} N_e{}^2 \left(\frac{N}{N_e}\right)^3 \tag{2.19}$$

According to figure 2.3, the tube disappears when it is passed by the end of the primitive chain. Hence, the fraction of tube remaining after time t can be represented by the tube survival probability [11]:

$$\psi(t) = \sum_{p;odd} \frac{8}{p^2\pi^2} \exp\left(-p^2 t/\tau_{rep}\right) \qquad (2.20)$$

Accordingly, the stress relaxation modulus is:

$$G(t) = G_e \psi(t) \qquad (2.21)$$

Over a wide time range, the dynamics of the polymer chains can be subdivided into different regimes. At very short times, the segment does not feel the presence of the confining tube and moves as a free Rouse chain. At $t > \tau_e$, the Rouse motion of the polymer segments is constrained perpendicular to the primitive path, whereas, along the primitive path, the motion is unrestricted. The constrained Rouse dynamics perpendicular to the primitive path scaled with $t^{1/4}$.

At this point, we can divide the polymer chain dynamics into a subdivision of motional regimes based on scaling laws in terms of mean-squared displacement of the polymer segments [101]:

$$\Phi(t) = \langle [R_n(t) - R_n(0)]^2 \rangle \qquad (2.22)$$

I) Free Rouse motion:

$$t \lesssim \tau_e \qquad \Phi(t) \sim t^{1/2} \qquad (2.23)$$

II) Constrained Rouse motion:

$$\tau_e \lesssim t \lesssim \tau_R \qquad \Phi(t) \sim t^{1/4} \qquad (2.24)$$

III) Reptation:

$$\tau_R \lesssim t \lesssim \tau_{rep} \qquad \Phi(t) \sim t^{1/2} \qquad (2.25)$$

IV) Free diffusion:

$$\tau_{rep} \lesssim t \qquad \Phi(t) \sim t^1 \tag{2.26}$$

2.6. Contour length fluctuation and constraint release

The reptation relaxation times are obtained under the fixed tube length assumption. In reality, the contour length fluctuates with time, changing the dynamical processes. Contour length defines the distance the polymer chain diffuses along the tube. When this distance is shortened, the relaxation time would be shorter than predicted by the reptation model. The reptation time including contour length fluctuation, $\tau_{rep}{}^{CF}$, can be found as

$$\tau_{rep}{}^{CF} \approx \tau_{rep}\left[1 - \mu\sqrt{\frac{N_e}{N}}\right]^2, \tag{2.27}$$

where τ_{rep} is the reptation time without contour length fluctuation and μ is a numerical constant.

Moreover, the surrounding chains are not fixed chains, which means the chains that form the tube can move away, and another chain comes in and forms another constraint. The change in the neighboring chains leads to the constraint release process [100]. Constraint release shortens the reptation relaxation time and increases the exponent of the mean-square displacement in the constrained Rouse regime.

2.7. Time-Temperature superposition

So far, the different relaxation regimes are expressed and distinguished by relaxation times. Since these can be written as the product of a temperature-independent factor and the monomer relaxation time (shortest Rouse mode relaxation time), all the relaxation modes follow the same temperature dependency, which is governed by the ratio of friction coefficient and absolute temperature ($\tau \sim \frac{\xi}{T}$). By defining a shift factor, it is possible to superimpose different data taken at

different temperatures into the reference temperature (T_{ref}) and provide a master curve of the response function. The shift factor a_T is

$$a_T = \frac{\xi(T)/T}{\xi(T_{ref})/T_{ref}}. \qquad (2.28)$$

By using the shift factor, the stress relaxation modulus can also be written as

$$G(T,t) = b_T G\left(T_{ref}, \frac{t}{a_T}\right). \qquad (2.29)$$

Here, $b_T = \frac{\rho T}{\rho_0 T_0}$ is the modulus shift factor that has a weak temperature dependence and recovers the entropic temperature dependence of the modulus.

The shift factor can be obtained by the well-known empirical equation called Williams-Landel-Ferry (WLF)

$$\log a_T = -C_1 \frac{T - T_{ref}}{T - T_{ref} + C_2}, \qquad (2.30)$$

where C_1 and C_2 are the empirical constants depending on the choice of T_{ref}.

2.8. Tube model in long-branched polymers

In linear polymers, the polymer motions are restricted to diffusion along the tube formed by the neighboring chains. In a long-branched polymer, the reptation along the tube is not simply linear. In this material class, multiple tubes must be considered since the branches are also constrained by their neighboring chains. For the relaxation of the backbone, the arms must be relaxed first. The first models for predicting the dynamical behavior of the branched polymers [69] were constructed based on the dynamic tube dilation (DTD) models developed for the star polymers[66,102].

The set of arm's tubes localizes the central branch point of a star. By imagining an arm confined inside a tube, it can be understood that the star polymer relaxes stress by arm retraction. This is the process in which the free ends of the star arms retract

back along their primitive path and orient themselves into a new tube (a tube belongs to another arm to make the reptation motion possible). Figure 2.4 shows the arm retraction process in a star and a comb polymer. This process is not entropically favorable as the number of available conformations for the arm chain highly reduces during arm retraction. Thus, thermal tension pushes the arm's end outward to explore new conformations. The retraction process would be unlikely if the arm's length is much longer than the entanglement spacing. Pearson and Helfand [103] considered a star polymer confined in a fixed network of entanglements. They defined a potential $U(x)$ as a function of the segmental curvilinear dimensionless coordinate that an arm segment must pass this barrier during the retraction process,

$$U(x) = \frac{15}{8}\frac{N}{N_e}x^2, \tag{2.31}$$

$$\tau(x) = \tau_0 \exp(U(x)), \tag{2.32}$$

where x is the segmental curvilinear dimensionless coordinate, and τ_0 is a time constant. They assumed a hierarchy of single exponential relaxations based on the segmental curvilinear dimensionless coordinate. This model, however, predicted an incorrect relaxation spectrum when applied to star polymer melts. It predicts far too strong an exponential dependence on N/N_e in compare to experiments [66,103].
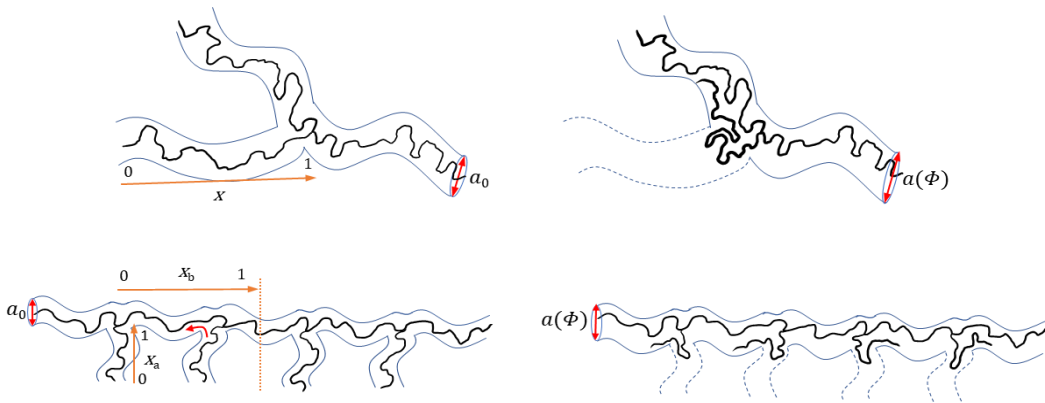
Figure 2.4: Arm retraction process as represented schematically in a star polymer (a, b) and a comb-polymer (c, d). it is seen that the retracted arm orients itself toward the dilated tube (the dilated tube has been expanded due to the relaxation of the arms). The segmental curvilinear dimensionless coordinate starts from 0 at the chain ends and goes to 1 at the branch point.

2.9. Dynamic tube dilation (DTD) model

For modeling the arm retraction process, it is necessary to check whether the assumption of a fixed network of entanglements is valid. Because of the broad spectrum of relaxation times, at time $\tau(x)$, only a segment with the segmental curvilinear dimensionless coordinate of x from the free end is relaxing, while all the chain segments with $x'<x$ have already relaxed. In other words, at time $\tau(x)$, x fraction of the arm has just relaxed, and the entanglements regarding this part of the chain disappeared. Accordingly, during the arm retraction process, the remaining unrelaxed segments are constrained by a diluted entanglement network. At any time $\tau(x)$, the fraction of the unrelaxed polymer segments equals *1-x*.

The tube assumption that considers the entanglements as binary events involving two chains implies $N_e(\Phi) = N_e\Phi^{-1}$, when Φ is the fraction of unrelaxed segments [102]. On the other hand, Colby and Rubenstein [104], who studied the effect of the dilution on the screening length and tube diameter, found that the tube diameter correlates with the concentration by an exponent of -2/3 in a θ solvent. Based on the self-similarity properties of polymer chains (i.e., $a^2 \sim N_e b^2$), $N_e(\Phi)$ can be found as:

$$N_e(\varphi) = N_e\Phi^{-\alpha}, \qquad \alpha = 4/3 \tag{2.33}$$

Accordingly, shear modulus can be written as:

$$G(\Phi) = \frac{kT\Phi}{N_e(\Phi)b^3} \Rightarrow G(\Phi) \sim G_0\Phi^{\alpha+1} \tag{2.34}$$

To describe the hierarchy of relaxation time regarding arm retraction, consider the relaxation of $x + \Delta x$ segment. This segment has to pass the additional potential barrier to retract:

$$\tau(x + \Delta x) = \tau(x)\exp(U(x + \Delta x, N_e(x + \Delta x)) - U(x, N_e(x))) \tag{2.35}$$

For small Δs:

$$\frac{d}{dx}\ln\,\tau(x) \sim \frac{dU_{eff}}{dx}(x) \sim \frac{\partial U(x, N_e(x))}{\partial x} \tag{2.36}$$

2.9.1. Full spectrum of arm relaxation in polymer combs

The outermost part of the arm follows constrained Rouse motion, whereas the retraction process of the intermediate and innermost segments is governed by diffusion over the potential barrier $U_{eff}(x_a)$. The entire relaxation spectrum of the arms is derived by smoothly crossing over from the early rouse-like relaxation time $\tau_{ae}(x_a)$ to the slower "activated" relaxation time $\tau_{al}(x_a)$. Hence the full spectrum reads:

$$\tau_a(x_a) = \frac{\tau_{ae}(x_a)\exp(U_a(x_a))}{1 + \tau_{ae}(x_a)\exp(U_a(x_a))/\tau_{al}(x_a)} \tag{2.37}$$

$\tau_{ae}(x_a)$, $\tau_{al}(x_a)$ and $U_a(x_a)$ are:

$$\tau_{ae}(x_a) = \frac{225\pi^3}{256}Z_a{}^4 x_a{}^4 \tau_e \tag{2.38}$$

$$\tau_{al}(x_a) = \frac{\tau_e x_a{}^{3/2}\left(\frac{2\pi^5}{15}\right)\exp(U_a(x_a))}{x_a(1 - \varphi_a x_a)^\alpha} \tag{2.39}$$

$$U_a(x_a) = \frac{15Z_a(1 - (1 - \varphi_a x_a)^{\alpha+1}(1 + (1 + \alpha)\varphi_a x_a))}{4(1 + \alpha)(2 + \alpha)\varphi_a{}^2} \tag{2.40}$$

Here x_a, Z_a, τ_e, φ_a and α are the segmental curvilinear dimensionless coordinate in an arm, the number of entanglement strands along the dangling arm, the Rouse relaxation time of an entanglement strand, the volume fraction of arms, and dilution exponent (=1 or 4/3), respectively. For small x_a, U_a and $\tau_{ae}(x_a)/\tau_{al}(x_a)$ goes to zero, then $\tau_{ae}(x_a)$ governs the relaxation hierarchy, while for intermediate values of x_a, $\tau_{ae}(x_a)\exp(U_a(x_a))/\tau_{al}(x_a)$ >>1 and consequently $\tau_{al}(x_a)$ is dominant. The equations 2.37-2.40 were derived from the Milner and Mcleish theory for the star polymers and modified for the polymer comb [66,69,73].

2.9.2. Backbone relaxation in polymer combs

In this part, the dynamics of the polymer comb backbone will be discussed beyond the arm retraction time. Two different relaxation methods govern the motion of the backbone: a) contour length fluctuation and b) reptation motion. On short time scales, the polymer comb backbone behaves like a star arm corrected with extra friction due to the presence of the arms at the branch points. On longer time scales, the reptation dynamics dominate and control the system's dynamic behavior. From another viewpoint, the segments near the free ends (x_b close to zero) relax through CLF, and the segments close to the center of the polymer backbone (x_b close to 1) follow reptation relaxation, which is the terminal relaxation time. Eventually, the backbone relaxes by whichever relaxation method is faster.

The CLF relaxation of the backbone is calculated by using the same cross-over function as used in the retraction process from an early relaxation time, $\tau_{be}(x_b)$, to a late one, $\tau_{bl}(x_b)$:

$$\tau_b(x_b) = \frac{\tau_{be}(x_b)\exp(U_b(x_b))}{1 + \tau_{be}(x_b)\exp(U_b(x_b))/\tau_{bl}(x_b)} \tag{2.41}$$

The form of the early relaxation time depends on the number of branch points. In the case of H-polymers, pom-poms, and lightly branched combs, the early-time relaxation reads:

$$\tau_{be}(x_b) = \frac{25}{64p^2}fZ_b{}^2x_b{}^2\tau_a(1)\varphi_b{}^{2\alpha}\,, \tag{2.42}$$

where f, $\tau_a(1)$, and φ_b are the number of free arms at one branch point, the arm retraction time at the branch point, and the volume fraction of backbone segments, respectively. p is an empirical constant of order unity which corresponds to the mean distance that the branch point hops along the tube at the time scale of the relaxation of an arm. McLeish et al. [72] have assumed p^2 as a fixed parameter with a value of 1/12. In contrast, Frischknecht et al. [67] found that the value of p^2 needs to be adjusted for each hierarchy separately to reach a reasonable agreement with the

experiment. Also, a value of p^2 =1/40 has been reported in work on the stress moduli of the PI asymmetric star and H polymers that provide a good agreement with experimental data [105]. For highly branched combs, the early relaxation time is controlled by the frictional dynamics that arise from more than one branch point and can be written approximately as

$$\tau_{be}(x_b) = \frac{375\pi}{8192\,p^2}qZ_b{}^3x_b{}^4\tau_a(1)\varphi_b{}^{3\alpha}.$$
(2.43)

Here, q is the number of branches along the backbone. The late relaxation time and the effective potential felt by the backbone in the CLF process are calculated as follows:

$$\tau_{bl}(x_b) = \frac{25Z_b{}^2\varphi_b{}^{2\alpha}q\tau_a(1)\exp(U_b)\sqrt{\frac{2\pi}{U"_b(x_b=0)}}}{8\,U'_b(x_b)\,p^2}$$
(2.44)

$$U_b(x_b) = \frac{15Z_b\varphi_b{}^{\alpha}(1-(1-x_b)^{\alpha+1}(1+(1+\alpha)x_b))}{8(1+\alpha)(2+\alpha)}$$
(2.45)

It is noted that the backbone is considered a two-armed star chain of length $Z_b/2$, which explains the factor of $\frac{1}{2}$ compared to equation 2.40. The CLF relaxation time increases significantly as x shifts to the central part of the chain. As it exceeds the reptation time, the dominant relaxation process changes into reptation. The reptation relaxation time of the backbone polymer comb is

$$\tau_{rep} = \frac{25(1-x_d)^2Z_b{}^2\varphi_b{}^{2\alpha}\tau_a(1)q}{8\pi^2p^2},$$
(2.46)

where x_d is the dimensionless distance from the chain-free end at which the reptation becomes the dominant relaxation process. This distance can be obtained by solving $\tau_{rep}(x_d) = \tau_b(x_d)$.

2.9.3. Stress Relaxation

As explained, the effective modulus of a diluted entanglement network can be written as follows:

$$G(\Phi) = G_0 \Phi^\beta \tag{2.47}$$

Here Φ is the fraction of unrelaxed segments. It can be defined at any $\tau(x)$, as a function of the segmental curvilinear dimensionless coordinate $\Phi(x) = 1 - x$. Thus, for stress relaxation modulus, a general expression can be written:

$$G(t) = \int_0^1 \frac{\partial G[\Phi(x)]}{\partial x} \exp\left(-\frac{t}{\tau(x)}\right) dx \tag{2.48}$$

This expression assumes that the effective modulus at time t depends on the fraction of the unrelaxed tube. The above equation can be divided into two contributions for a comb polymer [73]:

$$G(t) = G_0 \beta \left\{ \begin{array}{l} \int_0^1 \varphi_b^{\,\beta} (1 - x_b)^{\beta-1} \exp\left(\frac{-t}{\tau_b(x_b)}\right) dx_b \\ + \int_0^1 \varphi_a (1 - \varphi_a x_a)^{\beta-1} \exp\left(\frac{-t}{\tau_a(x_a)}\right) dx_a \end{array} \right. \tag{2.49}$$

The equation's first term represents the backbone's contribution and the second term expresses the arms' contribution to stress relaxation. Equation 2.49 has usually been written in terms of $\alpha = \beta - 1$ for simplicity, but in the current work that we will use this model to describe DQ NMR data, it is essential to emphasize the differences between β and α. The stress relaxation for the different regimes can be found as follows:

Rouse regime: The chain motion below the length scale of an entanglement strand is expressed by the Rouse model and, beyond this length scale, is described by the longitudinal dynamics within the confined tubes:

$$G(t) = \left(\frac{G_0 \varphi_a}{Z_a}\right)\left[G_{Rouse,a}(t) + \frac{G_{long,a}(t)}{5}\right] + \left(\frac{G_0 \varphi_b}{Z_b}\right)\left[G_{Rouse,b}(t) + \frac{G_{long,b}(t)}{5}\right] \quad (2.50)$$

$$G_{long,a}(t) = \sum_{p=1}^{\frac{5Z_a}{4}-1} \exp\left(-\frac{p^2 t}{Z_a{}^2 \tau_e}\right) \quad (2.51)$$

$$G_{Rouse,a}(t) = \sum_{p=\frac{5Z_a}{4}-1}^{\infty} \exp\left(-\frac{2p^2 t}{Z_a{}^2 \tau_e}\right) \quad (2.52)$$

The factor of 5/4 in the summation limits is taken from the Milner-MCleish definition of the number of entanglements [106]. The factor of 2 in the relaxation time of the sub-tube Rouse arises because the stress relaxes with half of the Rouse relaxation time [72,107]. In the backbone, the presence of the branches suppresses the motion for Rouse modes less than q, thus:

$$G_{long,b}(t) = \sum_{p=q}^{\frac{5Z_b}{4}-1} \exp\left(-\frac{p^2 t}{Z_b{}^2 \tau_e}\right) \quad (2.53)$$

$$G_{Rouse,b}(t) = \sum_{p=\frac{5Z_b}{4}-1}^{\infty} \exp\left(-\frac{2p^2 t}{Z_b{}^2 \tau_e}\right) \quad (2.54)$$

Arm retraction:

$$G_{arm\,retraction} = G_N(1 + \alpha)\, \varphi_a \int_0^1 (1 - \varphi_a x_a)^\alpha \exp\left(\frac{-t}{\tau_a(x_a)}\right) dx_a \quad (2.55)$$

Contour length fluctuation (in backbone):

$$G_{CLF} = G_N(1 + \alpha)\, \varphi_b{}^{1+\alpha} \int_0^{x_d} (1 - x_b)^\alpha \exp\left(\frac{-t}{\tau_b(x_b)}\right) dx_b \quad (2.56)$$

Reptation:

$$G_{reptation} = G_N(\varphi_b(1 - x_d))^{1+\alpha} \sum_{p=odd} \frac{8}{p^2\pi^2} \exp\left(-\frac{p^2 t}{\tau_d(x_d)}\right) \qquad (2.57)$$

2.10. Polymer chain dynamics at the gel point

Gelation is a transition from liquid-like behavior into solid network behavior, which happens at a critical extent of cross-linking reaction (p_c). The divergence of the zero-shear viscosity can also express the gel point during the crosslinking process [63]. It was experimentally observed that the critical gels exhibit a characteristic relaxation behavior that represents itself in a self-similar relaxation modulus [108,109]

$$G(t) = St^{-n}, \qquad (2.58)$$

where S is named gel stiffness and n is the critical relaxation exponent. The self-similar relaxation behavior is valid in the terminal zone at long times. As the longest relaxation time diverges at the gel point, the self-similar behavior has to be valid to infinite time. In branched polymers, self-similar behavior is of course observed on a finite time range. In contrast, the terminal flow will be observed for these polymers at very long times due to the constraint disengagement.

Theoretical [110–113] and experimental [114–119] works reveal that the rheological properties of a polymer system at rather low frequencies in the vicinity of the gel point follow a scaling law. It means that at the gel point, the correlation of G*(ω) with time is power-law:

$$G' \sim G'' \sim \omega^n \qquad (2.59)$$

$$\frac{G''}{G'} = \tan\delta = constant \qquad (2.60)$$

According to previous studies, the relaxation exponent decreases by progressing cross-linking reaction after the gel point and does not show any universality feature at the gel point in different systems [63,64].

3. NMR fundamentals

The starting point of nuclear magnetic resonance (NMR) spectroscopy goes back to December 1945 and January 1946, when Felix Bloch and Edward M. Purcell, respectively, independently reported the first successful observation of the phenomenon of NMR in solids and liquids. Their findings brought them the Noble prize in physics in 1952. Since then, the applications of NMR spectroscopy have become vast and have led to other Noble prizes for scientists who developed NMR spectroscopy into new fields. Nowadays, the characterization of the molecular structure of a moiety without NMR spectroscopy seems impossible. Particularly in polymer science, NMR spectroscopy's application is not limited to the molecular characterization of polymer chains (chemical structure and tacticity). Actually, it even assists polymer physicists in studying fast and slow chain dynamics [120].

The basis of NMR spectroscopy relies on an intrinsic property of atomic nuclei called nuclear spin *I*, specified by nuclear spin quantum number. Protons and neutrons that form the atomic nuclei have a spin. According to the number of nucleons (protons and neutrons) in atomic nuclei, a net nuclear spin denotes every nucleus. For example, ^{1}H and ^{13}C, as the most utilized NMR-active nuclei, have spin $\frac{1}{2}$ while ^{12}C is an inactive-NMR nucleus (*I*=0).

Spins possess the lowest energy level, called the ground state. In an external magnetic field $\vec{B}_0$, the interaction of the spin with the magnetic field leads splitting of the ground energy level into *2I+1* energy levels (Zeeman splitting), which are characterized by another quantum number *m* that is restricted to the values *-I* to *+I*. In the case of ^{1}H and ^{13}C, $m = \pm\frac{1}{2}$ which denotes to α and β states. The energy difference between these two states is equal to the Larmor frequency $\omega_0 = -\gamma B_0$ [121].

As the α state has lower energy than the β state, more spins possess the α state based on Boltzmann statistics. The difference in the population of spins in these two states results in a net magnetic moment (macroscopic longitudinal magnetization) in the same direction as $\vec{B}_0$. This macroscopic magnetization can be altered by a radio frequency (RF) pulse oscillating at the Larmor frequency. When the RF pulse is applied over a specific time (pulse length), the original longitudinal magnetization starts rotating around the pulse axis (in the rotating frame, see below) during pulse length at nutation frequency ω_{nut}.

Rotating the magnetization by 90° about the *y*-axis results in a net magnetization along the *x*-direction, called transverse magnetization. Once the RF pulse is turned off, the spins start precessing around the *z-axis*, leading to the macroscopic net magnetization rotation in the *xy* plane (fig 3.1). The frequency of this rotational motion is equal to the nuclear Larmor frequency. The time-dependent function of transverse magnetization is [122]:

$$M_x = M_{eq} \cos(\omega_0 t) \exp(-t/T_2) \tag{3.1}$$

$$M_y = -M_{eq} \sin(\omega_0 t) \exp(-t/T_2) \tag{3.2}$$
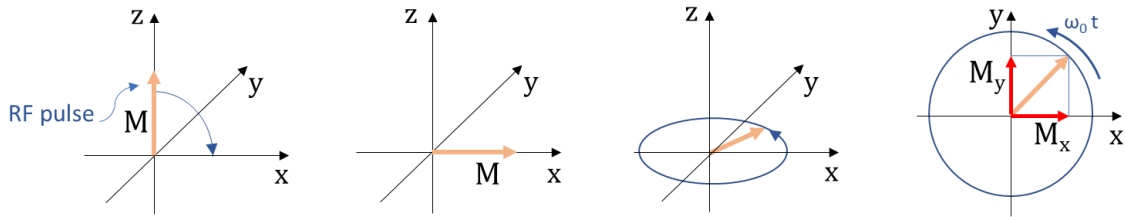
Figure 3.1: The magnetization flips 90° via RF pulse around the *y*-axis. The magnetization along the *x*-axis starts precessing around the z-axis in the *xy* plane, providing two projections on the *x* and *y*-axis as a function of time.

The transverse magnetization decays with the time constant T_2 which is called the transverse relaxation time. For liquids, T_2 can be several seconds, whereas, in solids, it can be as short as milliseconds or even microseconds. In order to simplify the transverse magnetization time dependency, one can remove the oscillating term by using a rotating frame. In the rotating frame, the observer (receiver) is rotating with

the same frequency as ω_0. In this frame, the transverse magnetization appears static, and consequently, equation 3.1 turns into:

$$M_x{}^{rot} = M_{eq}\exp(-t/T_2) \tag{3.3}$$

Meanwhile, in the z-axis, magnetization grows gradually towards the equilibrium value:

$$M_z = M_{eq}(1 - \exp(-t/T_1)) \tag{3.4}$$

Here T_1 is the exponential time constant called spin-lattice relaxation or longitudinal relaxation time. In the current work, we mainly focus on transverse relaxation.

3.1. Spin-half interactions

Among the spin interactions, chemical shift and direct dipole-dipole coupling are the most relevant ones in ^{1}H NMR in solids. Electron clouds around the atoms due to the state in a magnetic field induce a secondary local sub-molecular magnetic field $\vec{B}_{loc}$, which opposes the applied field at the center of motion and changes the magnetic field experienced by nuclei and the Larmor frequency of the nucleus. This effect, called chemical shift interaction denoted by δ, depends on the strength of the main magnetic field and the molecule's orientation with respect to the magnetic field vector [123].

Dipole-dipole coupling is a mutual interaction between the spins through their generated magnetic field in the surrounding space. The dipole-dipole coupling for an isolated spin pair depends on the distance between two spins and the orientation of the internuclear vector with respect to the magnetic field with the second Legendre polynomial $P_2(\cos\theta) = (3\cos^2\theta - 1)/2$ (θ is the angle between the internuclear vector and $\vec{B}_0$, which is shown in figure 3.2). A spin-pair interaction changes the Lorrentzain peak shape into a Pake powder pattern, while an extra broadening occurs in multispin systems due to the interaction between distant spins and turns the shape into a Gaussian spectrum (figure 3.2). Dipole-dipole coupling is

averaged to zero for isotropic motions like in liquids or dilute solutions, but in solids, anisotropic motion leads to a preaveraged residual dipolar coupling, D_{res}. The maximum magnitude of static-limit dipolar coupling is about 30 kHz as seen in rigid solids [123,124], depends on the typical proton desnsity.
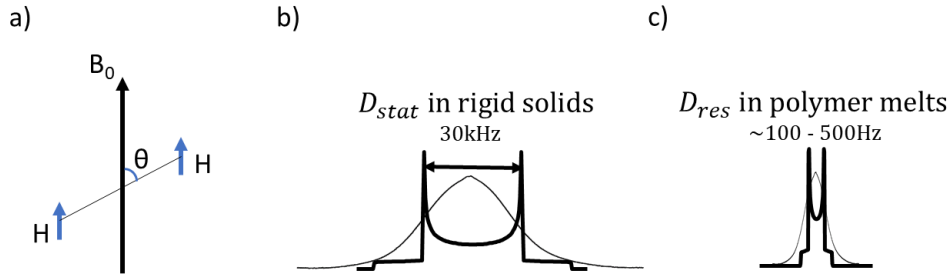
Figure 3.2: a) The angle between the magnetic field and the internuclear vector. In liquids with isotropic motions due to tumbling motions, this angle takes all the values between 0°-90°, and consequently, the dipolar coupling is time-averaged to zero. b) In solids like crystals in which the segmental motion is absent or highly restricted, the dipolar coupling attains its maximum value. c) In polymer melts, due to topological constraints, it is impossible that θ covers all the angles like in a liquid. This restricted motion leads to a residual dipolar coupling of hundreds of Hz.

3.2. Free induction decay (FID)

The free induction decay of protons in solids is governed mainly by the dipole-dipole coupling. The various chain motions in a system lead to different dipolar coupling and T_2^* relaxation. The segments in a semicrystalline polymer can be categorized into three phases based on the chain dynamics. These phases consist of a crystalline phase (denoted as c) with very high D_{res}, an amorphous phase (denoted as a) with much lower dipolar coupling, and an intermediate phase (denoted as i) that is located between these two phases. Since T_2^* correlates with the inverse D_{res}, the crystalline phase signal decays with a much shorter T_2^* than the amorphous phase. One can estimate the fraction of each phase by measuring the time domain FID and decomposing it based on the different relaxation times. For this purpose, the following equation can be used [125]:

$$I_{FID} = f_c e^{-(a^2 t^2)} \frac{\sin(bt)}{bt} + f_i e^{-(t/T_{2,i}^*)^{\nu_i}} + f_a e^{-(t/T_{2,a}^*)^{\nu_a}} \qquad (3.5)$$

Here, f, T^*_2, and v are the fraction of the corresponding phase, the apparent transverse relaxation time, and the shape exponent, respectively. a and b are the Abragam-function parameters that relate to the second moment with the following equation:

$$M_2 = a^2 + \frac{b^2}{3} = \frac{9}{20} D_{res}{}^2 \qquad (3.6)$$

Due to the so-called dead time of the spectrometer, which is usually of the order of 10 μs, the initial fast-decaying signal is not fully accessible. In order to avoid losing this part of the signal, the so-called Magic Sandwich Echo (MSE) can be used before detecting the FID signal. The MSE sequence refocuses fast-decaying NMR signals, governed by the strong dipolar coupling interaction via reversing the dipolar dephasing. Detailed information can be found in Ref. [125].

3.3. Proton double-quantum NMR

Proton double-quantum (DQ) NMR is a sensitive method for measuring residual dipolar coupling, particularly in polymer melts and networks. The presence of entanglements and cross-links as topological constraints in a polymer structure causes an anisotropic motion of chains that leads to a residual dipolar coupling. In the fast-motion limit where the segments move fast enough to occupy all the possible conformations on the time scales of hundreds of microseconds and ms, D_{res} reflects the local dynamic order parameter S_b via this equation:

$$S_b = \langle P_2(\cos\theta) \rangle = k \frac{D_{res}}{D_{stat}} = \frac{3}{5} \frac{r^2}{N} \qquad (3.7)$$

D_{stat} is the static dipolar coupling constant, k is a constant that corrects static dipolar coupling for very fast intra-segmental motions, r is the ratio of the end-to-end distance of the polymer chain to its unperturbed averaged value in the molten state, and N is the number of Kuhn monomers between two topological constraints.
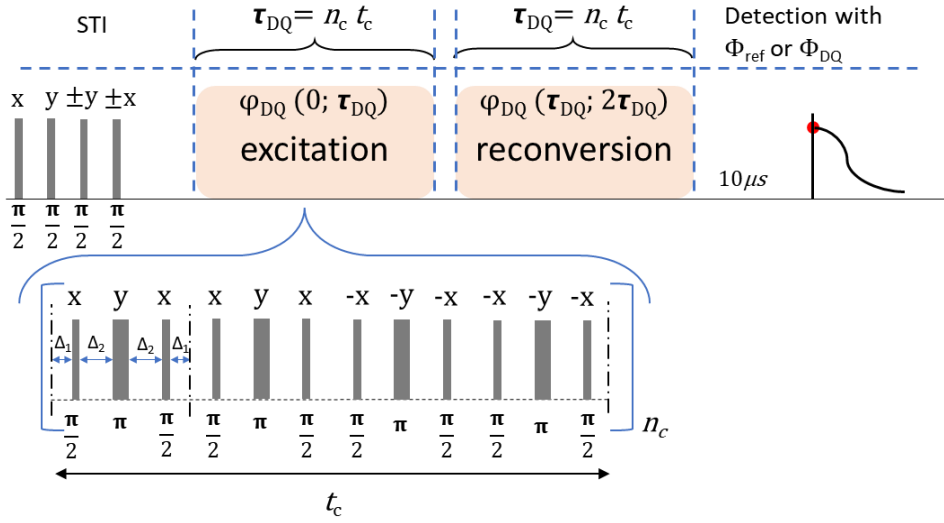
Figure 3.3: Schematic representation of the DQ NMR sequence used in this work. Spin-temperature inversion (STI) is used to remove T_1-related artifacts. The excitation and reconversion part consists of 4 cycles of the improved Baum-pines pulse sequence with different phases. The reference and DQ signals are recorded with an appropriate receiver phase in the detection part.

In this work, an optimized Baum-Pines pulse sequence [126,127] has been used for DQ NMR analysis. As depicted in figure 3.3, the MQ coherences were excited in the first part (excitation) and reconverted into detectable magnetization in the second part (reconversion). The DQ evolution time τ_{DQ} can be altered by increasing the delays between pulses (on low-field machines) or by repetition of the block (on high-field machines). By phase cycling, two signals, I_{ref} and I_{DQ}, are recorded as a function of DQ evolution time. The double-quantum intensity I_{DQ} contains signals from coupled protons which correspond to the chains with anisotropic motions, whereas the reference intensity I_{ref} carries the signal from all protons, including anisotropic moieties (coupled protons) and isotropic moieties. The amount of isotropically mobile defects (see figure 3.4) is usually reflected by a mono- or bi-exponential long-time tail of I_{ref}. In the "DQ NMR in networks" part, we will discuss the data analysis to remove the relaxation effect from DQ intensity.
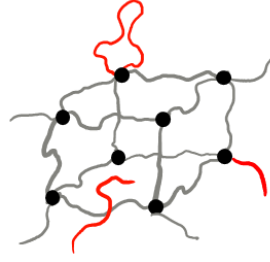
Figure 3.4: schematic representation of isotopically mobile defects in a network structure. Defects can be a dangling chain, a loop, or an entanglement-free chain

Following a spin-pair-based quantum-mechanical treatment [83],

$$I_{DQ} = \langle \sin \phi_1 \sin \phi_2 \rangle,$$ (3.8)

$$I_{ref} = \langle \cos \phi_1 \cos \phi_2 \rangle,$$ (3.9)

$$I_{\sum MQ} = I_{ref} + I_{DQ} = \langle \sin \phi_1 \sin \phi_2 \rangle + \langle \cos \phi_1 \cos \phi_2 \rangle,$$ (3.10)

with:

$$\phi_1 = \frac{D_{stat}}{k} \int_0^{\tau_{DQ}} P_2(\cos \theta(t)) \, dt,$$ (3.11)

$$\phi_2 = \frac{D_{stat}}{k} \int_{\tau_{DQ}}^{2\tau_{DQ}} P_2(\cos \theta(t)) \, dt.$$ (3.12)

θ expresses the instantaneous angle between the segmental orientation and the external magnetic field.

The Andersson-Weiss (AW) approximation [128] assumes a Gaussian distribution for the local magnetic field to analytically express NMR signals in the presence of molecular motions. The frequency distribution of an isolated spin-pair with anisotropic motion is of course Pake-like but, due to the interaction between distant spins in multispin systems, the actual spectrum shape turns into a Gaussian spectrum (figure 3.2). In the middle of the spectrum, which reflects the contribution of isotropic moieties, the distribution of the interaction frequency is Lorentzian and

deviates from the Gaussian shape. In the time domain NMR, this part of the spectrum corresponds to the signals at longer times. Due to this deviation from the Gaussian distribution, the validity of the AW approximation is limited to short times (where the decaying signal is mainly governed by the anisotropic moieties).

According to the AW approximation, the above equations turn into:

$$I_{DQ} = \sinh\langle\phi_1\phi_2\rangle \, e^{-\langle\phi_1{}^2\rangle} \tag{3.13}$$

$$I_{ref} = \cosh\langle\phi_1\phi_2\rangle \, e^{-\langle\phi_1{}^2\rangle} \tag{3.14}$$

$$I_{\sum MQ} = e^{\langle\phi_1\phi_2\rangle} e^{-\langle\phi_1{}^2\rangle} \tag{3.15}$$

In the second step of the AW approximation, the time and ensemble averages are determined in terms of the orientation autocorrelation function (OACF) via simple time integrals [101,129,130]:

$$\langle\phi_1(0,\tau)^2\rangle = \frac{4}{9}M_{2eff} \times 2\int_0^\tau (\tau - t') \, C(t') \, dt' \tag{3.16}$$

$$\langle\phi_1(0,\tau)\,\phi_2(\tau,2\tau)\rangle = \frac{4}{9}M_{2eff}\left[\int_0^\tau t' \, C(t') \, dt' + \int_\tau^{2\tau} (2\tau - t') \, C(t') \, dt'\right] \tag{3.17}$$

$C(t)$ is the probability of finding a segment in the same orientation after a specific time. The above equations are entirely independent of the choice of OACF, which will be discussed in the following sections.

3.3.1. DQ NMR in networks

In polymer networks far above the glass transition temperature, the absence of the reptation motion due to permanent topological constraints results in a plateau in OACF, proportional to the order parameter and thus the cross-link density. In order to determine the order parameter, it is necessary to remove the relaxation effect due to the segmental motion from the DQ signal. Since the relaxation in the I_{DQ} and $I_{\Sigma MQ}$ is almost equal for anisotropic moieties, it can be removed via point-by-point

normalization. Before the normalization, the contribution of isotropic moieties (defects) has to be subtracted from $I_{\Sigma MQ}$. For this purpose, $I_{\Delta MQ} = I_{ref} - I_{DQ}$[1] is plotted as a function of time, and the long-time tail is fitted with a single or bi-exponential decay function, as it is seen in figure 3. 5 [131].
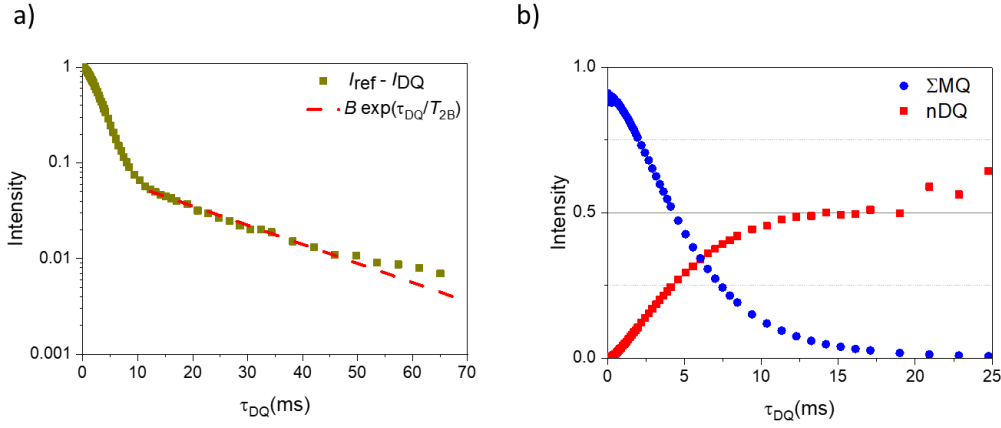
Figure 3.5: The DQ NMR data of PI melt with a molecular weight of 157 kDa at 100°C. a) $I_{\Delta MQ} = I_{ref} - I_{DQ}$ plotted as a function of DQ evolution time. The long-time tail is fitted with a single exponential decay. b) Point-by-point normalization cancels the relaxation effect, and the build-up curve to 0.5 can be seen. In a polymer melt that entanglements as physical constraints form a temporary network structure, D_{res} reflects the number of entanglements per volume.

The normalized DQ intensity I_{nDQ} can be written as:

$$I_{nDQ} = \frac{I_{DQ}}{I_{\Sigma MQ} - f_{def}\exp\left(-\frac{2\tau_{DQ}}{T_{2,iso}}\right)}$$

(3.18)

For networks, I_{nDQ} is a relaxation-free build-up curve to 0.5 that contains only the structural information (figure 3.5). By substituting $C(t) \approx S_b{}^2 = \left[\frac{D_{res}\,k}{D_{stat}}\right]^2$ and

---

[1] Since without tails $I_{DQ}=I_{ref}$ in the long-time limit, it is more reliable to fit the tails with the I_{ref}-I_{DQ} curve which is free of the coupled-proton contribution at long times.

$M_{2eff} = \frac{9}{20}\left(\frac{D_{stat}}{k}\right)^2$ into equations 3.16 and 3.17, the following function is obtained [127,132]:

$$I_{nDQ}\left(\tau_{DQ}, D_{res}\right) = 0.5\left[1 - \exp\left(-\frac{2}{5}D_{res}{}^2\tau_{DQ}{}^2\right)\right] \tag{3.19}$$

This equation is valid for fitting the data at short and intermediate times up to $I_{nDQ} \approx 0.45$. An empirical equation called *Abragam-like* (A-l) function was derived for fitting the entire build-up curve. A-l function is a modified version of the equation 3.19 [84]:

$$I_{nDQ}^{Al}\left(\tau_{DQ}, D_{res}\right) = 0.5\left[1 - \exp\left\{-\left(0.378\,D_{res}\,\tau_{DQ}\right)^{1.5}\right\}\right]\cos\left(0.583D_{res}\,\tau_{DQ}\right) \tag{3.20}$$

With this function, the fitting range of the I_{nDQ} curve can be extended up to longer times. As discussed, D_{res} is proportional to the inverse number of segments between two constraints. In real polymer networks, this parameter is not fixed. Thus, a distribution function can be assumed for the D_{res} value that can be determined by the following function

$$I_{nDQ}\left(\tau_{DQ}\right) = \int P(D_{res})\,I_{nDQ}\left(\tau_{DQ}, D_{res}\right)dD_{res}\,, \tag{3.21}$$

where $P(D_{res})$, is the predefined distribution function. Although a Gaussian distribution can be a good choice for the distribution function, the possible negative values for D_{res}, when the width is large, are physically meaningless. Hence the log-normal distribution function is a better choice:

$$P_{log}(\ln(D_{res})) = \frac{1}{\sigma_{ln}\sqrt{2\pi}}exp\left[\frac{-(\ln(D_{res}) - \ln(D_{med}))^2}{2\sigma_{ln}{}^2}\right] \tag{3.22}$$

The probability distribution depends on the median D_{res} and dimensionless distribution width σ_{ln}. The signal function for fitting the data can be obtained by numerical integration over the distribution:

$$I_{nDQ}(\tau_{DQ}) = \int P(\ln(D_{res})) \, I_{nDQ}(\tau_{DQ}, D_{res}) \, dln(D_{res}) \qquad (3.23)$$

In addition to the tail subtraction and point-by-point normalization, it is feasible to consider the relaxation effect by simultaneously fitting the $I_{\Delta MQ}$ and I_{DQ} signals with an exponential decay (representing the transverse relaxation). For the A-l function, it reads [87]:

$$I_{DQ}(\tau_{DQ}) = \frac{1}{2}\sum_{i=1}^{3} a_i \left[1 - \exp\left(-\left(0.378 \ 2\pi D_{res}^i \tau_{DQ}\right)^{1.5}\right)\right.$$
$$\left. \times \cos\left(0.583 \ 2\pi D_{res}^i \tau_{DQ}\right)\right] \exp\left[-\left(\frac{\tau_{DQ}}{T_{2i}}\right)^{\beta_i}\right] \qquad (3.24)$$

$$I_{\Sigma MQ}(\tau_{DQ}) = \sum_{i=1}^{3} a_i \exp\left[-\left(\frac{\tau_{DQ}}{T_{2i}}\right)^{\beta_i}\right] \qquad (3.25)$$

Here, i represents the moieties (isotropic or anisotropic), a and β are the fraction and the shape exponent, respectively. This method is suitable for cases the build-up curve to 0.5 is not accessible.

3.3.2. DQ NMR in polymer melts: Anderson-Weiss power-law model (AWPl)

When talking about polymer melts, we mean the polymer chains above their glass transition temperature without any crosslinks between the chains. In polymer melts, unlike polymer networks, all the topological constraints can be disengaged at long times. In other words, the polymer chain can free itself from the entanglements over a long time due to the reptation motion, as discussed in chapter 2. In terms of the scaling law, four characteristic subdivisions are predicted for the MSD of the polymer segments according to the tube model beyond the glassy state. Figure 3.6 demonstrates the schematic representation of the OACF and MSD in different regimes. In the Rouse regime, the OACF decays with a scaling exponent of 1, twice the corresponding value in the MSD. The reason for this discrepancy arises from the different nature of OACF and MSD; while the MSD presents a first-order correlation function and OACF corresponds to a second-order correlation function [133]. In the

constrained Rouse and Reptation regimes, the OACF will reflect the return-to-origin (RTO) and tube survival probabilities, respectively, which scales as the inverse of the MSD [101]. The tube model predicts the characteristic exponent value for these two regimes as 1/4 and 1/2, respectively.
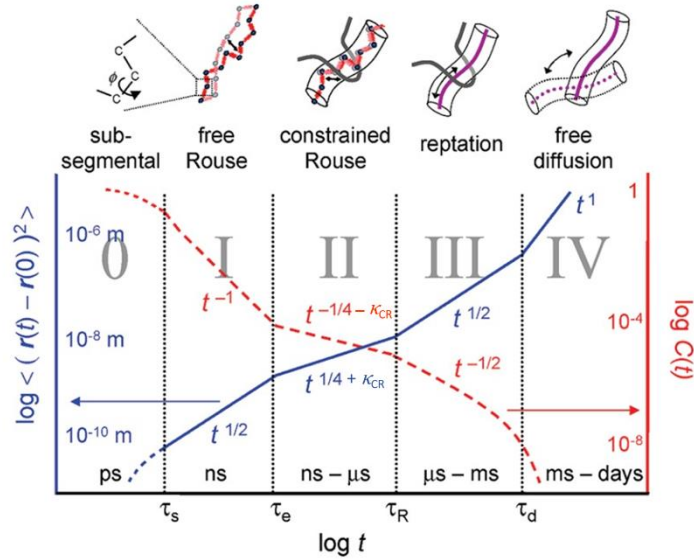
Figure 3.6: Schematic representation of the predicted OACF and the MSD in different regimes according to the tube model in a polymer melt far above T_g. In the free Rouse regime, due to the different nature of MSD and OACF, there is a factor of 2 between the detected NMR-based OACF exponent and the inverse of the MSD exponent. Due to the constraint release in the constrained Rouse regime, the detected exponents exceed the predicted absolute values. This is shown by a sum with constraint release contribution. Reproduced from Ref. [90]with permission from the ACS.

According to the scaling law, the OACF can be assumed as a power-law function for a polymer melt:

$$C(t) = \begin{cases} S_b^2 & for\ |t| < t_0 \\ S_b^2\ (t/t_0)^{-\kappa} & for\ |t| \geq t_0 \end{cases} \tag{3.26}$$

The signal functions turn into (by substituting $C(t)$ in equations 3.16, 3.17):

$$I_{DQ} = \exp\left\{-\frac{\frac{1}{5}D_{res}^2}{(\kappa-2)(\kappa-1)}\left((\kappa-\kappa^2)t_0^2 + (2\kappa^2-4\kappa)\tau_{DQ}t_0 + 2\tau_{DQ}^{2-\kappa}t_0^\kappa\right)\right\}$$

$$\times \sinh\left\{\frac{\frac{1}{5}D_{res}^2}{2(\kappa-2)(\kappa-1)}\left((\kappa^2-\kappa)t_0^2 + (2^{3-\kappa}-4)\tau_{DQ}^{2-\kappa}t_0^\kappa\right)\right\} \quad (3.27)$$

$$\times \exp\left(-\frac{\tau_{DQ}}{T_2}\right)$$

$$I_{\Sigma MQ} = \exp\left\{-\frac{\frac{1}{5}D_{res}^2}{(\kappa-2)(\kappa-1)}\left(\frac{3}{2}(\kappa-\kappa^2)t_0^2 + (2\kappa^2-4\kappa)\tau_{DQ}t_0\right.\right.$$

$$(3.28)$$

$$\left.\left. + (4-2^{2-\kappa})\tau_{DQ}^{2-\kappa}t_0^\kappa\right)\right\} \times \exp\left(-\frac{\tau_{DQ}}{T_2}\right)$$

Here, $S_b \sim D_{res}$ defines the amplitude of the $C(t)$ at time t_0, which is the power-law decay onset time and can be taken to be very close to the lower end of the fit interval, and κ is the power-law exponent of the OACF [134]. These two functions are used for the simultaneous fitting of the defects-free signals by considering an exponential decay for coupled protons which is multiplied by the signal functions. The tails can be considered explicitly in a simultaneous fit, like what has been shown for the Al function (equation 3.24), to avoid the ambiguity of tail subtraction in polymer melts.

It has to be noted that the current model neglects spin displacements between the actual RF pulses. This displacement (expressed by OACF) modifies the signal functions, in particular at very short times. Brekotkin et al. [135] recently suggested a model to determine this contribution for the power-law OACF and proved that this contribution is almost negligible for $\kappa < 0.5$.

3.3.3. DQ NMR in comb polymers: Anderson-Weiss exponential model (AWexp)

In this part, we will look at the polymer comb as a complex polymer hierarchy and map out the chain dynamics based on the DTD model discussed in chapter 2. As indicated, stress relaxation is governed at short times by the arm retraction process and contour length fluctuations (in the backbone) and at longer times by reptation

motion. In the first two processes, a relaxation time spectrum is defined as a function of segmental curvilinear dimensionless distance from the free end.

DQ NMR can probe the hierarchy of the relaxation times in terms of OACF. According to the DTD model, tube dilation results from the relaxation of segments. Thus, an explicit relation between the OACF and the fraction of unrelaxed segments seems necessary. According to equation 3.7, which is valid for linear polymer melts as well as networks, the order parameter correlates with the inverse entanglement spacing. Consequently, we can write:

$$C(t) \approx S_b(t)^2 \approx N_e(t)^{-2} \approx \Phi(t)^{2\alpha} \tag{3.29}$$

On the other hand, Lang and Sommer [136] have shown by computer simulation that in lowly cross-linked systems with many entanglements between permanent constraints, the order parameter scales with $(N\,N_e)^{-0.5}$, where N is the number of segments between two permanent strands. The inner part of the polymer comb backbone states between two branch points temporarily immobilized by the long arms. Due to the described analogy, the OACF can be written in terms of the entanglement spacing as:

$$C(t) \approx S_b(t)^2 \approx N_e(t)^{-1} \approx \Phi(t)^{\alpha} \tag{3.30}$$

Since we are using the DTD model to describe DQ NMR signals for the first time in the current work, both exponents in equations (3.29) and (3.30) are considered for analyzing the data in chapter 6. From now on, the OACF-related dilution exponent is denoted by β to avoid any misunderstanding:

$$C(t) \approx \Phi(t)^{\beta} \tag{3.31}$$

A characteristic OACF can be defined for every segment based on the relaxation time spectrum:

$$C(t, x_{a,b}) = S_b(\Phi)^2 \exp\left(-\frac{t}{\tau(x_{a,b})}\right) \tag{3.32}$$

Here, S_b depends on the fraction of unrelaxed segments. The fraction of relaxed segments is equal to the segmental coordinate at any time according to the suggested interpretation of the DTD model for monodisperse comb (and H) polymers by McLeish et al. [73]. In this interpretation, it is assumed that when a segment relaxes, all segments with shorter relaxation times have already relaxed [69,73,137]. Thus the fraction of relaxed segments is defined only based on the segmental coordinate (e.g. for a segment in an arm at x_a position, the fraction of relaxed segment is $\varphi_a x_a$.) at any time whereas, this is only valid at times longer than the corresponding relaxation time. In rheology, although fits predict the tube model parameters perfectly, this assumption leads to an overestimation of the arms' contribution in the storage modulus at short times. In the DQ NMR, it causes physically meaningless correlation functions for arms and backbone. This will be discussed in detail in chapter 6.

The OACF for arm segments and backbone segments can be written, respectively:

$$C(t, x_a) = S_{b,0}^2 (1 - \varphi_a x_a)^\beta \exp\left(-\frac{t}{\tau(x_a)}\right) \tag{3.33}$$

$$C(t, x_b) = S_{b,0}^2 \varphi_b (1 - x_b)^\beta \exp\left(-\frac{t}{\tau(x_b)}\right) \tag{3.34}$$

$S_{b,0}$ is defined as the order parameter corresponding to the rubbery plateau in OACF (that would arise if constraints were fixed).

Using the Andersson-Weiss approximation, the signal functions for a simple exponential decay read [88]:

$$I_{DQ}(\tau_{DQ}, \tau_p, D_{res}) = exp\left\{-0.4{D_{res}}^2{\tau_p}^2\left(e^{-\frac{\tau_{DQ}}{\tau_p}} + \frac{\tau_{DQ}}{\tau_p} - 1\right)\right\}$$
$$\times sinh\left\{0.2{D_{res}}^2{\tau_p}^2\left(e^{-\frac{2\tau_{DQ}}{\tau_p}} - 2e^{-\frac{\tau_{DQ}}{\tau_p}} + 1\right)\right\}$$

(3.35)

$$I_{\Sigma MQ}(\tau_{DQ}, \tau_p, D_{res}) = exp\left\{-0.2{D_{res}}^2{\tau_p}^2(4e^{-\frac{\tau_{DQ}}{\tau_p}} - e^{-\frac{2\tau_{DQ}}{\tau_p}} + \frac{2\tau_{DQ}}{\tau_p} - 3)\right\}$$ (3.36)

Here, τ_p is the relaxation time of a single segment corresponding to the relevant process (p denotes arm retraction or CLF processes).

The above equations are valid for arm retraction and CLF until $t= \tau_d$ when the reptation process becomes dominant. The OACF in the reptation regime can be expressed as:

$$C(t) = {S_{b,0}}^2(\varphi_b(1 - x_d))^{\beta} \sum_{p=odd} \frac{8}{p^2\pi^2} \exp\left(-\frac{p^2 t}{\tau_d(x_d)}\right)$$ (3.37)

The corresponding signal functions read:

$$I_{DQ}(\tau_{DQ}, \tau_d, D_{res}) = \exp\left\{\sum_{p=odd} \frac{-8}{p^2\pi^2} 0.4{D_{res}}^2(\frac{\tau_d(x_d)}{p^2})^2(e^{-\frac{p^2\tau_{DQ}}{\tau_d(x_d)}} + \frac{p^2\tau_{DQ}}{\tau_d(x_d)} - 1)\right\}$$
$$\times \sinh\left\{\sum_{p=odd} \frac{8}{p^2\pi^2} 0.2{D_{res}}^2(\frac{\tau_d(x_d)}{p^2})^2(e^{-\frac{2p^2\tau_{DQ}}{\tau_d(x_d)}} - 2e^{-\frac{p^2\tau_{DQ}}{\tau_d(x_d)}} + 1)\right\}$$

(3.38)

$$I_{\Sigma MQ} = \exp\left\{\sum_{p=odd} \frac{-8}{p^2\pi^2} 0.2{D_{res}}^2\left(\frac{\tau_d(x_d)}{p^2}\right)^2 (4e^{-\frac{p^2\tau_{DQ}}{\tau_d(x_d)}} - e^{-\frac{2p^2\tau_{DQ}}{\tau_d(x_d)}} + \frac{2p^2\tau_{DQ}}{\tau_d(x_d)} - 3)\right\}$$

(3.39)

The overall signal can be written as the sum of the segmental contributions of arms and backbone:

$$I_{DQ} = \varphi_a \int_0^1 I_{DQ}^a\big(\tau_{DQ}, \tau(x_a), D_{res}(x_a)\big)dx_a + \varphi_b \left[\int_0^{x_d} I_{DQ,CLF}^b\big(\tau_{DQ}, \tau(x_b), D_{res}(x_b)\big)dx_b\right.$$

$$\left. + (1 - x_d)I_{DQ,rept}^b\big(\tau_{DQ}, \tau(x_d), D_{res}(x_d)\big)\right] \tag{3.40}$$

$$I_{\Sigma MQ}$$

$$= \varphi_a \int_0^1 I_{\Sigma MQ}^a\big(\tau_{DQ}, \tau(x_a), D_{res}(x_a)\big)dx_a + \varphi_b \left[\int_0^{x_d} I_{\Sigma MQ,CLF}^b\big(\tau_{DQ}, \tau(x_b), D_{res}(x_b)\big)dx_b\right. \tag{3.41}$$

$$\left. + (1 - x_d)I_{\Sigma MQ,rept}^b\big(\tau_{DQ}, \tau(x_d), D_{res}(x_d)\big)\right]$$

By considering the T_2 relaxation effect arising from faster motions that are not modeled explicitly and assuming a component representing the isotropic moieties (tail), the DQ signals can be fitted to extract the structural information of a branched polymer (e.g. a comb). In our argument, the total DQ NMR signals ($I_{\Sigma MQ}$, I_{DQ}) are a sum of contributions from each segment, each of which has its own specific correlation function that depends on its position in the hierarchical structure.

4. Experimental details

In this chapter, detailed information about the samples and experimental work is introduced. In the given thesis, the samples can be categorized into two groups, HDPE grades and a comb-polyisoprene. These two groups' experimental details are different and will be introduced separately.

4.1. Materials

Two grades of HDPE were irradiated by an electron beam to form crosslinks. Hostalen ACP 6031D with melt flow rate = 0.35 g/10min at 190°C/2.16kg, density = 0.96 g/cm^3 obtained under ISO 1183-1, produced by LyondelBasel Co., with a broad molecular weight distribution was used in this work. The mentioned grade contains antioxidants and is suitable for blow molding and packaging applications. This grade will be denoted in the following chapters as B-HDPE, in which '*B*' represents 'broad molecular weight distribution'.

Total Lumicene® mPE M5510 EP (a second-generation metallocene HDPE) with flow rate = 1.2 g/10min at 190C/2.16kg, density = 0.955 g/ml obtained under ISO 1183-1, M_n = 27,700 g/mol, PDI = 2.8, produced by TOTAL Co., was used as the second grade and will be refered to as N-HDPE which 'N' represents 'narrow molecular weight distribution'.

A polyisoprene comb polymer was synthesized via anionic polymerization by Dr. Jonas Sebastian Keller in Professor Dr. Manfred Wilhelm's research group. In the fully protonated comb polymer structure, the backbone and the arm length are 68 kg/mol and 13.8 kg/mol, respectively. On average, each backbone carries 8.5 arms.

Also, a backbone-deuterated sample with an almost identical structure was produced (the average molecular weight of the backbone and the arm are 72.6 kg/mol and 13.8 kg/mol, respectively and each backbone carries 8.5 arms on

average). According to the obtained DQ NMR data (see Appendices part A), this sample unfortunately degraded during the experiment.

4.2. Irradiation of the samples

The electron beam treatment at STERIS-AST (Bitterfeld, Germany) was carried out at room temperature on polymer sheets (10×10 cm^2) with a thickness of 2.3 mm using their 10 MeV IBA Rhodotron TT200 J116 accelerator. The applied doses varied from 28 kGy to 168 kGy in 28 kGy steps.

4.3. Characterization techniques

4.3.1. Gel content

Sol-gel analysis was performed by IKTR (Weißandt-Gölzau, Germany) to extract the amount of soluble parts in the material. Approximately 250 mg of the sample with 1.5% stabilizer was kept in boiling xylene for 8 hours. After extraction, the sample was dried in vacuum in two steps: 16 hours at room temperature and 2 hours at 90 °C. Two replicates were tested for each sample, and the average value was reported. The gel content value was calculated according to

$$\text{Gel content (\%)} = \frac{m_1}{m_0} \times 100\% \,,$$

where m_1 and m_0 are the sample masses after and before extraction, respectively.

4.3.2. Rheological measurements

a) Irradiated HDPEs:

Dynamic shear measurements were done using Anton Paar MCR 501 rheometer with 8 mm parallel-plate geometry. Frequency sweeps from 0.1 to 100 rad/s are performed on rubbery samples at 130°C -190°C, well above the melting point of PE.

b) PI-comb:

Small-amplitude oscillatory shear measurements were carried out using ARES-G2 rheometer with a 13 mm parallel plate geometry by Dr. Jonas Sebastian Keller.

4.3.3. NMR measurements:

a) x-HDPEs:

NMR measurements were carried out on a Bruker minispec mq20 benchtop spectrometer operating at a Larmor frequency of 20 MHz (B_0 = 0.47 T), with 90° pulse and 180° pulses of 1.6 or 2.8 μs and a receiver dead time of 14 μs. The sample temperature was controlled using a Bruker BVT 3000 temperature controller with an accuracy of ±0.5 K.

The DQ-NMR experiments were conducted using a compensated version of the Baum-Pines pulse sequence to probe the time evolution of the dipolar coupling interaction in HDPE samples. The samples in the form of 8mm disks were placed into the 10mm NMR glass tube filled with argon and flame-sealed to prevent degradation. For measuring DQ NMR at 130°C, the samples were heated up to 150°C to be sure that all the crystals disappeared, and then they were cooled down to 130°C.

The samples crystallized by first heating up to 150°C to be sure that all the crystals disappeared, then they were cooled down to 100°C with a cooling rate of 2 K/min. After keeping them at 100°C for 1 hour, the FID and MSE signals were measured for FID decomposition method (to assess the crystallinity).

b) PI-comb:

The PI-comb samples were measured in a sealed 5mm NMR glass tube on a 400 MHz (9.4 T) AvanceIII-Bruker spectrometer with 90° pulse and 180° pulses of 4 and 8 μs, respectively, using a static probe. A temperature controller unit regulated the sample temperature with an accuracy of 0.5 K.

5. Chain dynamics in electron-beam irradiated HDPEs

In this chapter, two different grades of irradiated HDPE (in a semi-crystalline state at room temperature) are characterized via probing chain dynamics and gel fraction. First, the gel content results will be presented to evaluate the amount of network formed in each sample due to the irradiation crosslinking process. Then the samples are characterized in the melt via rheological and DQ NMR measurements to map out the chain dynamics and network structure of the irradiated polymers. The key results of this part are published in Ref. [94].

In the second part of this chapter, the correlation between the chain dynamics observables (DQ NMR and rheological results) and the gel fraction is discussed to find a potential replacement technique for the classical experiments relying on hazardous solvents used at high temperatures.

5.1. Irradiation of the samples and gel content values

Two grades of HDPE samples (N-HDPE: narrower molecular weight distribution, B-HDPE: broad molecular weight distribution) were irradiated in a semi-crystalline state with a crystallinity of more than 70%. In the electron-induced reactive process (EIReP), the electron beam can break hydrogen-carbon or carbon-carbon bonds and form two radicals [138]:

$$-\mathrm{CH_2}- \xrightarrow{\text{\textit{irradiation}}} -\dot{\mathrm{C}}\mathrm{H}- \ + \dot{\mathrm{H}} \qquad\qquad (5.1)$$

$$-\mathrm{CH_2}-\mathrm{CH_2}- \xrightarrow{\text{\textit{irradiation}}} -\dot{\mathrm{C}}\mathrm{H_2} \ + \ \dot{\mathrm{C}}\mathrm{H_2}- \qquad\qquad (5.2)$$

The former can form a bond with another chain and produce a 4-arm star PE, which eventually results in a network structure. The latter, called chain scission, reduces the chain's molecular weight but can also react with another radical and form a branched PE with a higher molecular weight. The associated reactions are:

$$-CH_2 - + \dot{H} \longrightarrow - \dot{C}H - + H_2 \tag{5.3}$$

$$2 - \dot{C}H - \longrightarrow \quad \begin{matrix} -CH- \\ | \\ -CH- \end{matrix} \tag{5.4}$$

$$-\dot{C}H - + - \dot{C}H_2 \longrightarrow \quad \begin{matrix} -CH- \\ | \\ -CH_2 \end{matrix} \tag{5.5}$$

It must be noted that the possible reactions in the system are much more than that listed here, but as they are not relevant to our research focus, they were not mentioned. More details about the reactions can be found in Ref. [138].

During the electron beam irradiation of HDPE in the semi-crystalline state, radicals are produced in the crystalline as well as the amorphous phase. Though, the crosslinking reactions are assumed to mainly take place in the amorphous phase. The lack of mobility of the chains in the crystalline phase reduces the reactions between radicals significantly [139,140]. Consequently, the final product would be a network with non-uniform distributed cross-links, as depicted in figure 1.2. The results of the gel content experiment, which was performed to determine the fraction of network chains in the irradiated samples, were summarized in Table 5.1. In both grades, the gel content values increase with increasing irradiation dose in low irradiated samples (below 84 kGy). In x-B-HDPE-1, irradiated with 28 kGy, 10% of the chains formed a network structure, whereas, in another grade with the same irradiation dose, no gel-like structure was found.

Moreover, another difference between the two grades can be seen in the highest network fraction formed at very high irradiation doses. The highest gel fraction in B-HDPEs is around 70%wt, while 92% of irradiated N-HDPE chains are part of the gel at 140 kGy. The existence of the very short-unentangled chains in broad HDPE can be a reason for the lower maximum gel content value. This will be discussed in detail in the following parts.

As discussed, the cross-linking reaction occurs mainly in the amorphous phase. Since most segments are located in the crystalline region, only a limited part of the chain is available for cross-linking. Therefore, the gel content value increases

significantly at low irradiation doses until it reaches a regime that, even by further irradiation, does not change significantly. This behavior can be seen for both samples in irradiation doses above 84 kGy. In conclusion, the cross-linking and chain scission reactions are in equilibrium at high irradiation doses, and further irradiation results in degradation that is revealed in the samples irradiated with 168 KGy due to a slight drop in gel content values.

Table 5.1: Irradiation dose and gel content values for two different HDPE grades. The 'B' and 'N' represent broad and narrow molecular weight distribution, respectively.

Samples	Irradiation dose (kGy)	Gel content	NMR network fraction (Al)	NMR network fraction (AWPl)
x-B-HDPE-1	28	10% ± 2.7%	0.27	0.68
x-B-HDPE-2	56	51% ± 4.6%	0.3	0.68
x-B-HDPE -3	84	70% ± 0.1%	0.3	0.67
x-B-HDPE -4	112	68% ± 1%	0.34	0.69
x-B-HDPE-5	140	73% ± 1%	0.36	0.68
x-B-HDPE-6	168	72% ± 0.1%	0.36	0.68
x-N-HDPE-1	28	< 1%	0.19	0.85
x-N-HDPE-2	56	40% ± 10%	0.24	0.82
x-N-HDPE-3	84	85% ± 1%	0.29	0.85
x-N-HDPE-4	112	87% ± 1%	0.32	0.83
x-N-HDPE-5	140	92% ± 2%	0.32	0.83
x-N-HDPE-6	168	88% ± 1%	0.33	0.81

5.2. Rheological measurements

Frequency-dependent shear data measured at 190°C is demonstrated in figure 5.1 for two series of HDPE samples. It is noted that the experiments at lower temperatures (starting at 140 °C) above T_m were conducted, but due to weakly temperature-dependent segmental dynamics at such high temperatures above the nominal T_g, constructing a master curve using TTS did not expand the frequency range for more than half a decade. Therefore, only in the isothermal frequency sweeps are shown.

The moduli of the non-crosslinked sample in both HDPE grades show the typical behavior of a polydisperse polymer melt in the flow region. In N-HDPE-0, the storage and loss moduli cross each other at around 100 rad/s frequency, whereas in B-HDPE-0, the crossover is at around 10 rad/s. In figures 5.1b and d, the crossovers can be seen in $\tan(\delta)$ passing unity. Due to the broader molecular weight distribution in B-HDPE grade, this can reveal the existence of longer chains with a slower relaxation process in this sample.

According to the gel content values in Table 5.1, the lowest irradiated N-HDPE did not form a gel, while x-B-HDPE-1 has already passed the gel point and formed a network structure. For x-B-HDPE-1, irradiation causes a power-law behavior in storage and loss moduli decay which is a characteristic behavior close to and above the gel point [64,114]. Moreover, $\tan(\delta)$ becomes independent of angular frequency at a low-frequency range. x-N-HDPE-1 shows identical behavior to x-B-HDPE-1 at the high-frequency range, though, unlike x-B-HDPE-1, a rise in $\tan(\delta)$ toward one is observed at low frequencies.

According to the crosslinking mechanism in the early stages, x-N-HDPE-1 can be considered a mixture of the star and branched polymers that extend the Rouse regime due to postponing the reptation and the free-diffusion regime and consequently shows a branched polymer incipient-gel behavior [64]. The incipient-gel behavior in x-N-HDPE-1 rheological data confirms the presence of branched structures in the irradiated samples. In this sample, this delay shifts the crossover of storage and loss moduli to lower frequencies out of the accessible frequency range.

However, it can be claimed that in the very initial stages of irradiation, the mechanical gelation (according to the scaling law) occurs due to the long chain branching (sample x-N-HDPE-1). Afterward, these structures are connected via chemical bonds by further irradiation and become a part of the permanent network.
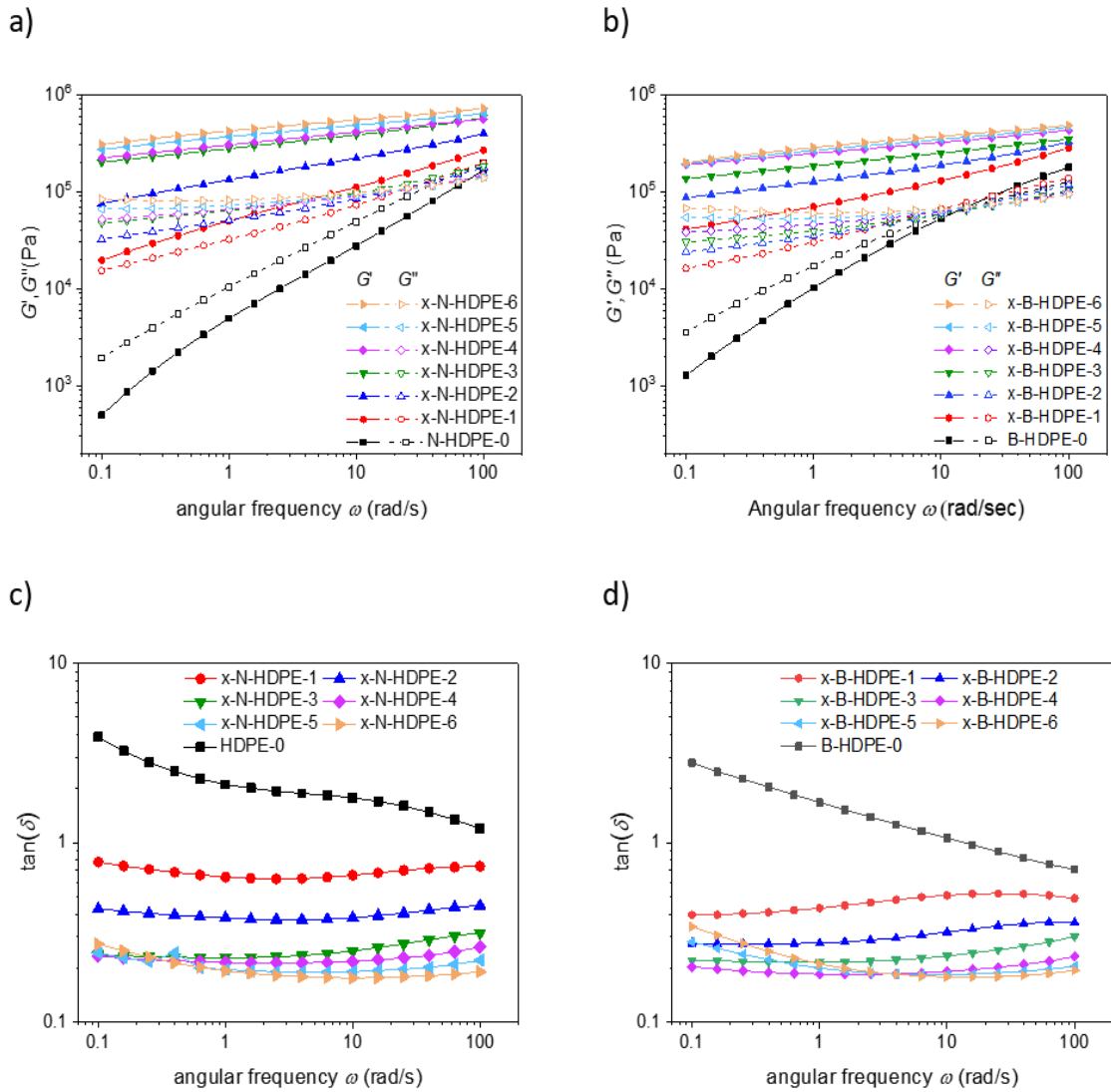
Figure 5.1: Rheological frequency sweeps of the irradiated and non-irradiated samples at 190°C; the storage and loss moduli of a) N-HDPE and c) B-HDPE samples. tanδ for b) N-HDPE and d) B-HDPE samples

A systematic increase of storage modulus with irradiation dose is observed in all the irradiated samples. In general, a transition from free diffusion into power-law and a gradual decrease in the rheological power-law exponent toward a plateau as a

consequence of irradiation can be addressed for all the samples though a plateau is not observable in the given frequency range. A continuous decay of the storage modulus is even seen in highly irradiated samples.

A polymer network mainly contains a contribution of elastically inactive moieties incapable of taking a mechanical load. These moieties, such as soluble fraction (including high molecular weight star-polymers, branched polymers, and linear polymers), long dangling chain ends, and trapped entanglements add relaxational contributions to the system, which is reflected in significant loss moduli and non-constant storage moduli in all irradiated samples. The loss modulus is always below the storage modulus and $\tan(\delta)$ remains below unity in the studied frequency range.

Therefore, the irradiated samples are far from a perfect network and contain a significant amount of imperfections. Although drawing a conclusion about the gel point based on the rheological data alone is tricky, the continuous increase of the storage modulus that highlights the increase of crosslinks facilitates a comparative conclusion. It is noted that the increase in the number of crosslinks in highly irradiated samples does not increase the gel content values, so it may increase the average molecular weight of the defects, or in other words, it slows down the relaxation of defects.

5.3. DQ NMR measurements

As explained in chapter 3, to extract the structural information from DQ NMR data, the signal contribution of isotropic moieties should be subtracted. The contribution of the isotropic moieties is reflected in the ΔMQ signal as an along-time tail that is fitted with a bi-exponential decay function (see section 3.3.1). Subtraction of the defect contribution from the ΣMQ signal leads to a visibly single exponential decay curve (see figure 5.2a).

Figure 5.2b shows the relaxation-free I_{nDQ} build-up curve obtained via point-by-point normalization. Unlike in well-developed networks, the I_{nDQ} build-up curve does not reach a long-time limiting intensity of 0.5. This behavior has been observed for a polymer melt in the reptation and free-diffusion regimes. In our samples being

partial networks, one reason to see this behavior may be the presence of a large number of defects and short uncross-linked chains, which can be classified as coupled defects (have an anisotropic motion) but relax on the time scale of the experiment.

As an alternative option, the simultaneous fitting of ΣMQ and DQ signals with an exponential decay for transverse relaxation, described in chapter 3, is used to extract the structural information from DQ NMR data. The signal functions are obtained based on the defined OACF function according to the sample's characteristics (polymer melt or network).
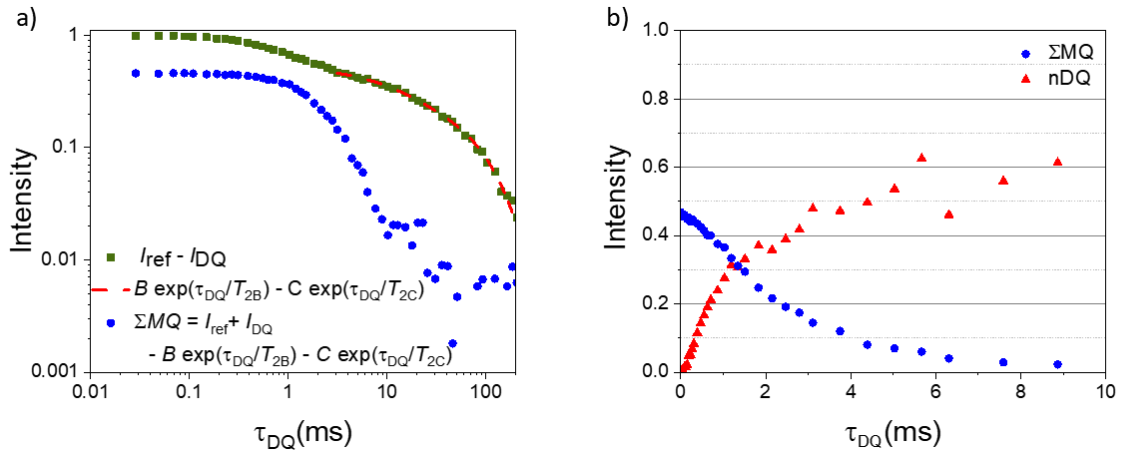
Figure 5.2: a) fitting the slow decaying signal at long times with a bi-exponential function for x-N-HDPE-6 measured at 170°C. The best-fit line is assigned with the red dashed line. b) the tail subtracted ΣMQ, and point-by-point normalized DQ is shown. Unlike the well-developed network, the normalized DQ build-up curve did not reach 0.5 value.

In this study, the irradiated samples are investigated in two different ways of thinking. In the first one, the irradiated samples are considered polymer networks described by the Abragam-like (A-l) model diluted with a large number of defects. The defects as the moieties with isotropic motion are reflected in the slow decaying signal, whereas coupled protons show a faster decay. In this approach, the OACF is assumed to exhibit a plateau, although this plateau may not be accessible in the investigated time range of the DQ NMR necessarily.

In the second approach, the whole system is assumed as a polymer melt with a spectrum of relaxation times. In this approach, short linear chains relax faster than the chains with higher molecular weight (network chains can be considered a polymer with a molecular weight of infinity). The OACF associated with this complex polymer melt can be approximated by a power-law function. Figure 5.3 shows the simultaneous signals fitting with the A-l function and the Andersson-Weiss power-law (AWPl) function. As seen, with the A-l function, it is possible to fit the I_{DQ} at longer times, whereas with the AWPl model, the fit interval is limited to the maximum of I_{DQ}.
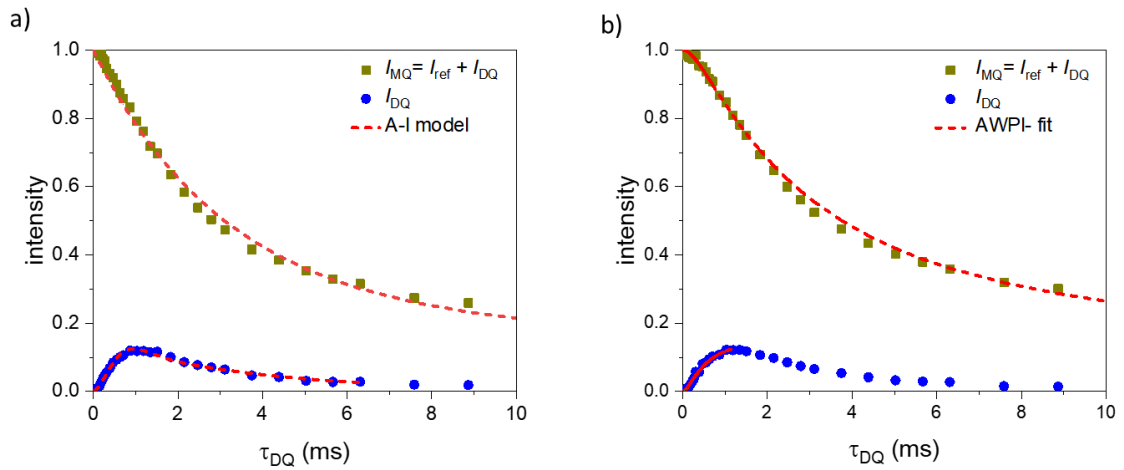
Figure 5.3: Simultaneous fitting of the DQ NMR signals via a) A-l function and b) AWPL model. with the A-l function, the DQ signals can be fitted to pretty long times, while in the AWPL model, the fitting range is limited to the maximum of DQ intensity.

The DQ NMR data are fitted with the A-l function with and without assuming distribution for D_{res}, and a bi-exponential function fits the defect contribution. In the AWPl model, a log-normal distribution was considered for D_{res}, and a single exponential function fits the defects contribution.

5.3.1. Abragam-like model (A-l)

D_{res} and the apparent fraction of coupled protons (network-like protons) are shown at different temperatures for two grades of HDPE in figure 5.4. Due to the anisotropic motion of the polymer segments located between two topological constraints, whether permanent (crosslink) or temporary (entanglement), a finite

D_{res} arise. In both HDPE grades, D_{res} decreases with temperature, revealing some relaxation processes on the studied timescale. These relaxation processes make it impossible to see a plateau purely arise from the crosslinks.
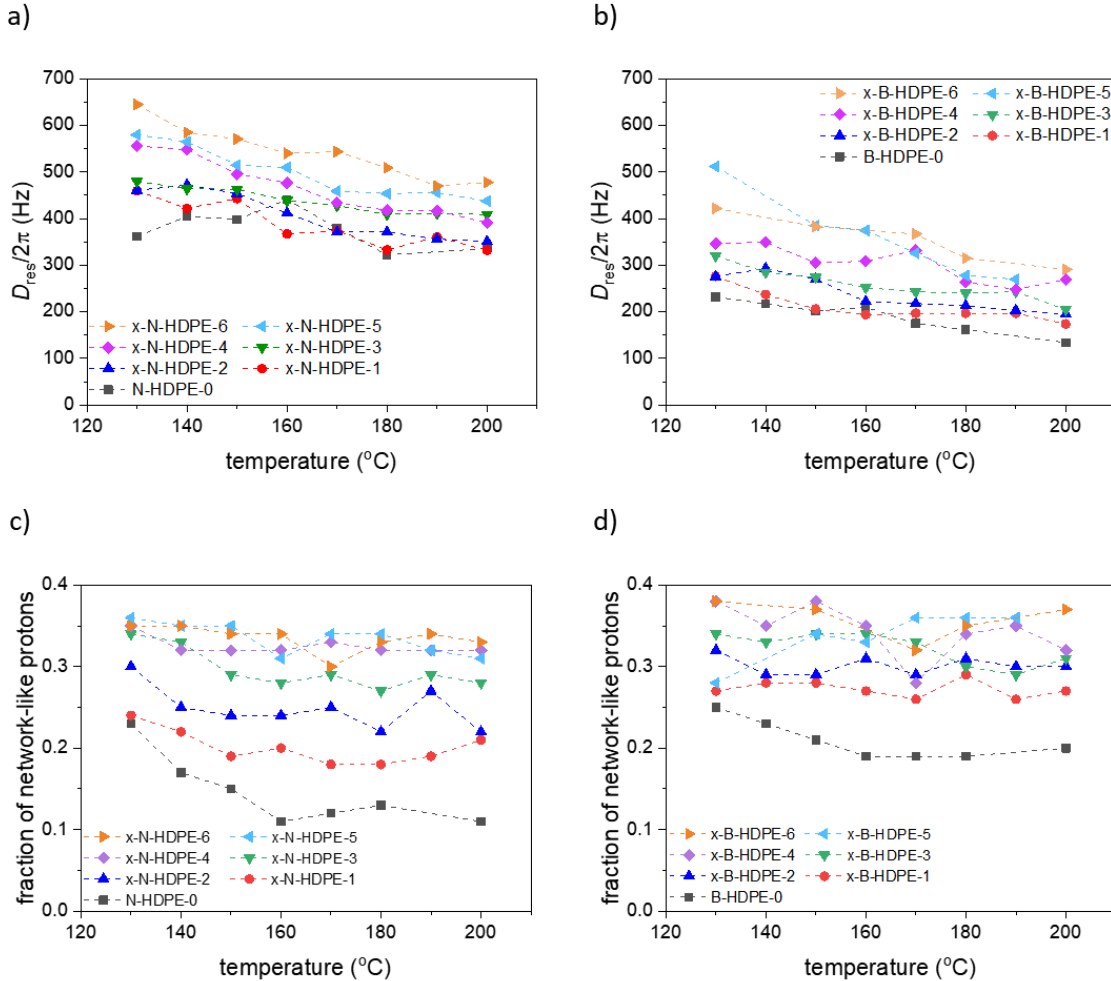
Figure 5.4: The NMR observables as a function of temperature obtained via simultaneous fitting based on the A-l function; D_{res} for a) N-HDPEs, b) B-HDPEs and the fraction of network-like protons for c) N-HDPEs, d) B-HDPEs

In non-irradiated samples, D_{res} values reflect only the average number of entanglements on the measured timescale, whereas, in irradiated ones, this value reflects the combined number of entanglements and cross-links. Distinguishing between physical and chemical constraints is tricky unless in case of a plateau in D_{res} value, which reveals that all the physical constraints have already disengaged and D_{res} arises only from chemical crosslinks. Although D_{res} does not quantitatively

reflect the number of crosslinks, the effect of irradiation on the chain dynamics can be seen in D_{res} values, particularly at temperatures above 170 °C.

Increasing the temperature enhances the segmental dynamics and increases the possibility that the segments free themselves from physical constraints. In other words, it is expected that the amount of isotropic moieties increases (= decrease of the network-like protons) with increasing temperature, as observed in figure 5.4c, d for non-irradiated samples. In irradiated samples, as the irradiation dose increases, not only the fraction of network-like protons is increasing, but even its dependency on temperature is gradually disappearing. The amount of defects (isotropic moieties) is much higher compared to well-developed networks, which confirms that the network is partially cross-linked and diluted with a considerable amount of defects.

Comparing the amount of DQ NMR defects with the fraction of defects obtained from the extraction experiments (Table 5.1), two kinds of discrepancy can be highlighted in highly and lowly irradiated samples. In highly irradiated samples amount of soluble moieties is much less than the fraction of defects measured by DQ NMR. The A-l function is originally well-suited for assessing network structure in elastomers (well-developed networks). Therefore, by using this function for a partially cross-linked network, weakly coupled protons belonging to the segments in weakly entangled chains are considered defects. This can explain the high amount of defects determined by the A-l model. In lowly irradiated samples (even non-irradiated ones), DQ NMR measured a smaller fraction of defects in comparison to the extraction experiment since DQ NMR, as well as rheology, is sensitive to the transient elasticity in their respective time/frequency window.

The inhomogeneity of the network can be probed by assuming a lognormal distribution for D_{res}. In figure 5.5, the distribution of D_{res} obtained based on the A-l model is shown for different irradiation doses at 170 °C for two series of HDPE. The effect of the irradiation is not only observed in shifting the median D_{res} into higher values, but also it enhances the distribution width. This effect is more intense in highly irradiated samples (higher than 84 kGy), where for large D_{res} values, a tail starts appearing. Based on the gel content values, samples irradiated at 84 kGy are

close to their maximum gel content, and further irradiation increases the gel content only insignificantly. The distribution data reveals that further irradiation leads to an over-crosslinking in some parts of the samples. Since less than 30% of the segments (according to the crystallinity data) can form crosslinks, this result is expected.
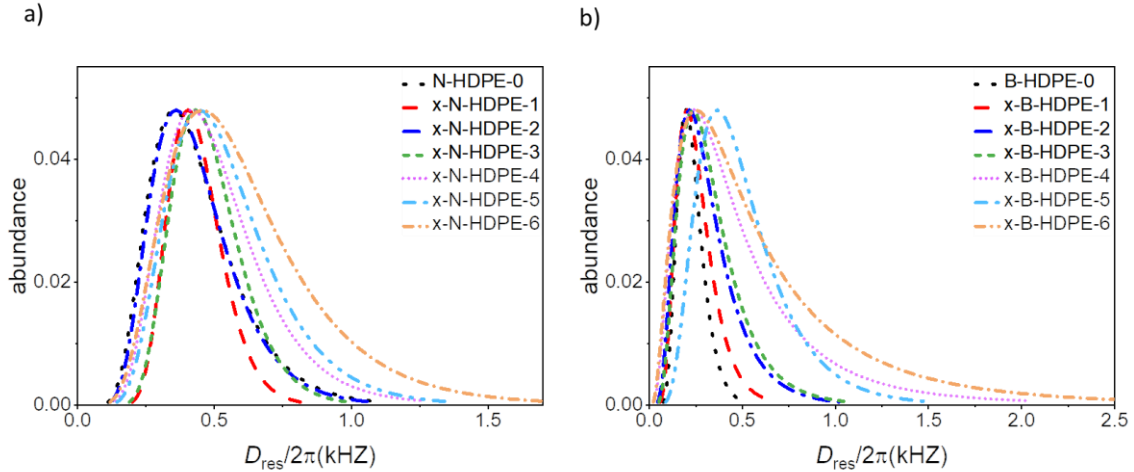
Figure 5.5: Log-normal distribution of D_{res} at 170°C obtained via simultaneous fitting based upon A-l function for a) N-HDPEs and b) B-HDPEs

5.3.2. Andersson-Weiss power-law model (AWPl)

According to the mentioned results from the extraction experiment, rheology, and DQ NMR, it is stressed again that a significant amount of defects dilutes the x-HDPE networks and adds relaxation pathways to the system. Moreover, a significant level of entanglements, some trapped between cross-links, exists in the network structure and disengages or relaxes like in a polymer melt. Also, the presence of the complex polymer structure (whether connected or not connected to the network structure), i.e., star and branched polymers, adds an extra broad relaxation spectrum (see chapter 2) to the relaxation pattern of the mentioned defects. Since the AWPl model is better suited for studying polymer melt dynamics and providing access to the actual shape of the OACF, it is a good choice for examining the irradiated HDPE networks. The best-fit results obtained via the AWPl model are shown in figure 5.6.
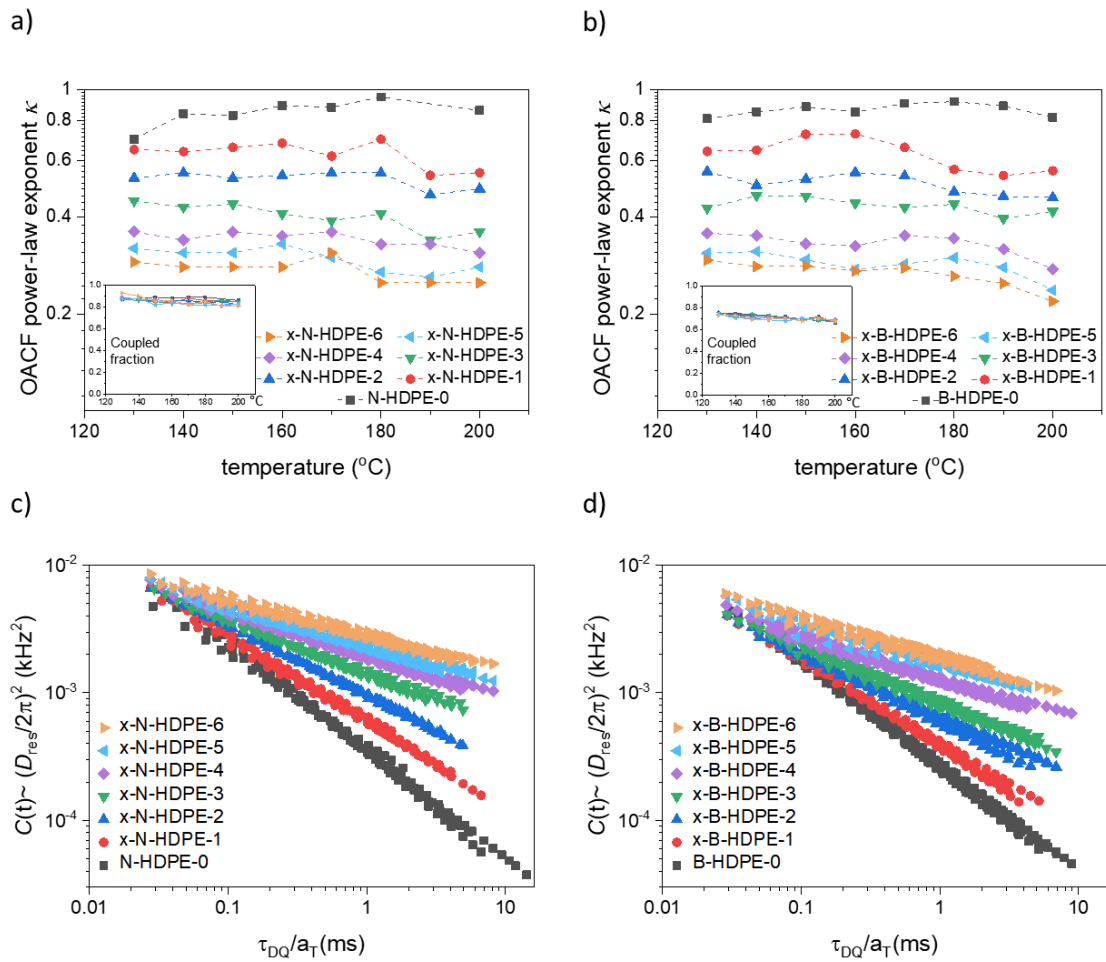
Figure 5.6: OACF exponent κ as a function of temperature, obtained via AWPl simultaneous fitting for a) N-HDPEs and b) B-HDPEs. The inset depicts the fraction of coupled protons in the AWPl model versus temperature. The fraction of coupled protons in both insets is almost independent of temperature and irradiation dose. OACF master curves at a reference temperature of 130°C according to the obtained κ and D_{res} values from the AWPl model for c) N-HDPEs and d) B-HDPEs. The constructed OACF at different temperatures were shifted using rheological shift factors.

The effect of irradiation on the chain dynamics can be observed in the power-law exponents κ (figure 5.6 a, b). In both HDPE grades, κ values associated with non-irradiated samples increase with temperature and shift into 1. This reveals a transition to the free-diffusion regime. In contrast, for other samples, the temperature dependency of κ becomes weaker even in N-x-HDPE-1, which does not form a permanent network but, due to the formation of stars and branched structures, hinders the reptation motion. In highly irradiated samples (>84 kGy), unlike gel content experiment and rheology, the decrease of κ values sensitively

demonstrates the gradual increase of the cross-linking reactions in x-HDPE-3 to x-HDPE-6.

The inset plots show the fraction of coupled protons in different temperatures. Unlike for the A-l model, this fraction varies only in a narrow range (from 80% to 90% for the N-HDPE series and 65% to 75% for the B-HDPE series) in both HDPE grades. This means that in all experiments (for the same HDPE grade), the OACF is roughly constructed for a fixed fraction of the chains at different temperatures. This is necessary for using TTS (see below) and facilitating the comparison of the data.

Figures 6c and d show the constructed OACF based on the AWPl model for different samples using TTS. Although using TTS provides no more than half an additional decade in time, monitoring small changes in the fitted κ values and representing an average power-law exponent over the fitted time interval is instructive. According to the data, we can confirm that in irradiated samples, the OACF follows a power-law decay. Above the gel point, the reptation motion is hindered, and the irradiated polymers are more network-like, whereas the associated OACF indicates a constrained Rouse motion, ultimately tending to a network-like plateau.

As discussed in the rheological measurements part, even though x-N-HDPE-1 is not a gel, due to the restriction caused by branches, the chains cannot display reptation motion and thus act like a network on the timescale of the experiment. Although the OACF increases monotonically with increasing the irradiation doses, this increase is reduced significantly above 84 kGy, where the gel content values are close to the maximum value. Similar to a slight decrease of κ values in highly irradiated samples, the gradual increase of the OACF reveals further crosslinking.

5.4. Direct comparison of rheology and DQ NMR

Table 5.2 summarizes the key parameter from rheological measurements and the DQ NMR technique for comparison. As mentioned, since the fraction of network-like protons was independent of the temperature and irradiation dose in the AWPl model, the obtained OACF can be compared to the rheology. The DQ NMR technique

assesses the chain dynamics approximately one decade faster than rheology. Therefore, for comparing these two techniques, the data obtained by DQ NMR at the highest possible temperature are used in table 5.2. The reported D_{res} value is not the fitting parameter as before, but it is obtained from the OACF curves ($D_{res}^2 \sim C(t)$) at the longest time accessible by DQ NMR, i.e., 5 ms). It is noted that rheological power-law exponents were obtained via a power-law fitting in a narrow frequency range, which makes it feasible for non-network samples.

It is seen in table 5.2 that the D_{res} increases monotonically, as the storage modulus, with increasing the irradiation dose. Nevertheless, comparing the κ values and rheological power-law exponents reveals the most significant discrepancy between the DQ NMR and rheological measurements. In the samples with a significant amount of the network, the κ values are roughly twice higher than the rheological power-law exponents. As discussed in chapter 2, this apparent NMR-rheology discrepancy is generally observed in polymer melts for the Rouse regime since the OACF is a second-order correlation function (only beyond τ_e up to constrained Rouse regime where the return-to-origin probability argument becomes relevant, according to which the exponent should be the same) [10,133].

Figure 5.7 illustrates the relation between the square root of the OACF with storage modulus at approximately comparable times/frequencies (the dynamic windows of the experiments do not entirely overlap). The plot confirms the offset-free relation of D_{res} with the storage modulus, which is consistent with the previous study on the well-entangled polymer melts and well-crosslinked elastomers [141]. It has to be considered that the storage moduli are all below the entanglement plateau modulus of PE (G'_e).

Table 5.2: Comparison between DQ NMR and rheological observables in different irradiated samples

Sample	Fraction of network-like protons (AWPl)	$D_{res}/2\pi$ [Hz] (at 5 ms)	κ (at 200°C)	Storage modulus [kPa][a]	Rheological power-law exponent
N-HDPE-0	0.86	10	0.86	166	0.9[b]
x-N-HDPE-1	0.85	14	0.55	267	0.37[b]
x-N-HDPE-2	0.82	20	0.49	397	0.24
x-N-HDPE-3	0.85	27	0.36	577	0.15
x-N-HDPE-4	0.83	35	0.31	561	0.13
x-N-HDPE-5	0.83	38	0.28	636	0.12
x-N-HDPE-6	0.81	43	0.25	722	0.12
B-HDPE-0	0.67	8	0.82	178	0.52
x-B-HDPE-1	0.68	12	0.56	282	0.34
x-B-HDPE-2	0.68	17	0.46	326	0.23
x-B-HDPE-3	0.67	20	0.42	346	0.14
x-B-HDPE-4	0.69	29	0.28	430	0.12
x-B-HDPE-5	0.68	33	0.24	460	0.12
x-B-HDPE-6	0.68	34	0.22	483	0.11

a) storage modulus measured at 190°C and 100 rad/s.

b) narrow frequency range of 5 to 100 rad/s.

A tentative direct comparison of the DQ NMR and rheological measurements is illustrated in figure 5.8. For this purpose, the OACF curves obtained from DQ NMR results are transferred to the frequency domain simplistically with $1/\tau_{DQ}$, which is the inverse of the power-law slopes. This transformation is only valid in the case of

a single power law with a constant exponent. The discussed factor of 2 difference in the exponents is considered by doubling the vertical range of the OACF axis. By looking at the figure, it is observed that G' values are indeed proportional to the square root of C(t) (due to the doubling of the $C(t)$ axis scale), as it was shown in table 5.2 and figure 5.7. In highly irradiated samples, the normalized storage modulus nicely follows the decay in the normalized OACF.
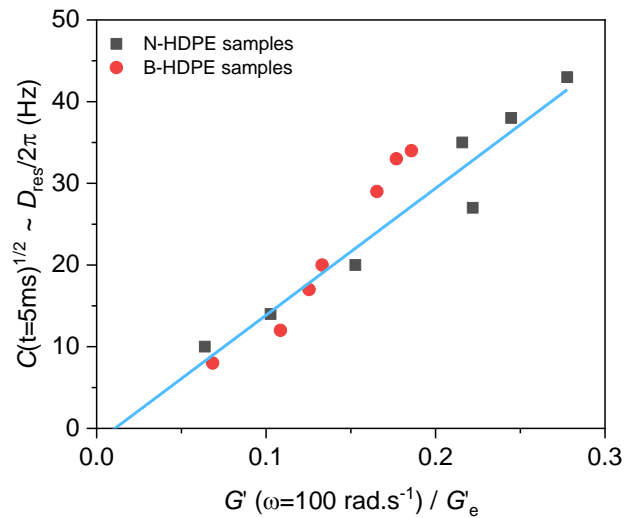
Figure 5.7: D_{res} corresponding to the OACF at 5 ms as a function of storage modulus at 100 rad/s normalized by the rheological plateau modulus for N-HDPEs (black points) and B-HDPEs (red points) with different irradiation dose. The linear fit slope and y-intercept are 155.5 and -1.69 respectively.

Since the non-irradiated samples are close to their free-diffusion regime, the direct comparison of the rheology with DQ NMR is not straightforward, and the observed discrepancies in slopes and vertical values are expected. On the one hand, crosslinking reactions effectively increase the molecular weight (even in x-N-HDPE-1 due to the formation of star and branched structures), leading to an extended Rouse regime, which enables the direct comparison of the data sets. On the other hand, a significant amount of short chains, chain ends, and branched polymers (the dynamics of the branched polymers follow a complex exponential spectrum discussed in chapter 2) in lowly irradiated samples caused a significant superposition effect. This superposition and the enhanced dynamics possibly moving into the constrained-Rouse and reptation regimes, may influence the validity of the

comparison, as in x-B-HDPE-1 and x-N-HDPE-1, the power-law exponent is not fully consistent with our argument about considering the factor of 2.
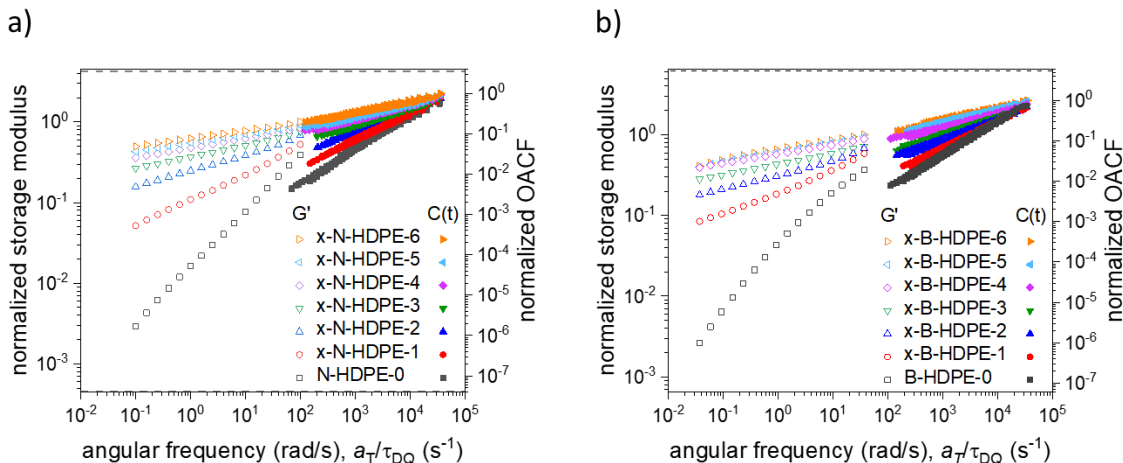
Figure 5.8: Direct visual comparison of normalized storage modulus and OACF plotted versus the inverse of DQ evolution time on a logarithmic scale at 130°C for a)N-HDPEs and b) B-HDPEs. The OACF vertical scale is extended by a power of 2 to visually cancel the different exponents of OACF and storage modulus in irradiated samples.

5.5. Relation of gel fraction with rheological and DQ NMR observables

So far, we have investigated the chain dynamics affected by irradiation in two HDPE grades using DQ NMR and rheology. In the DQ NMR technique, we examined two different methods to assess a model that can better describe the complex chain dynamics and finally showed that the results are consistent with rheological measurements. From now on, we focus on finding an empirical relation between DQ NMR and rheological observables with the extraction based gel fraction to characterize the partially cross-linked networks based on our findings for practical applications.

In figure 5.9, the fraction of network-like protons obtained from the AWPl model for non-irradiated samples is compared with the highest actual gel content value of two HDPE grades separately. At first glance, the fraction of the network-like protons in non-irradiated samples is surprisingly close to the maximum gel content values obtained in highly irradiated HDPEs (irradiated at 140kGy). In order to find a reasonable explanation for this, two questions should be answered. The first

question is regarding the reason for different maximum gel content values obtained in different samples, and the second question is how the fraction of NMR-based network-like protons can be related to the maximum gel content value in highly irradiated samples.
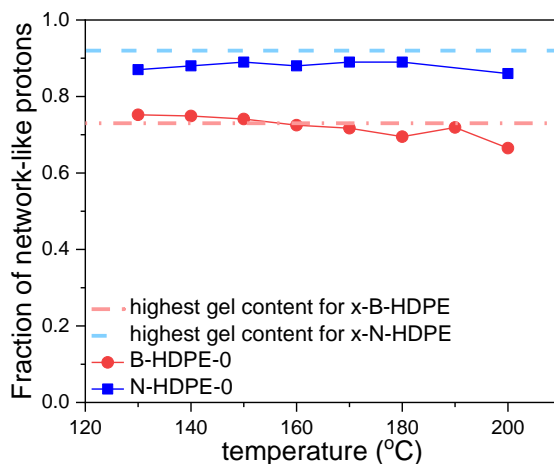
Figure 5.9: Fraction of network-like protons obtained by the AWPl model for two HDPE grades as a function of temperature. The highest gel content values of each grade (associated with the sample irradiated at 140 kGy) are shown as a dashed line.

The main reason for relatively lower gel content values in the semi-crystalline irradiated polyethylene compared to the molten irradiated ones is the presence of the crystalline region in which the cross-linking reaction is mainly surpassed due to the very restricted segmental mobility. A polymer chain needs at least one crosslink to be part of the network structure (from the gel content point of view). This means a radical should be produced in the polymer chain by absorbing the electron beam energy to react with another radical to form a crosslink. Since the reaction between the radicals relies on the segmental mobility, the crosslinking reaction in the crystalline region is not favored. Thus, the chains with smaller contributions in the crystalline phase have a higher chance of forming a chemical bond to the permanent network (see figure 5.10).
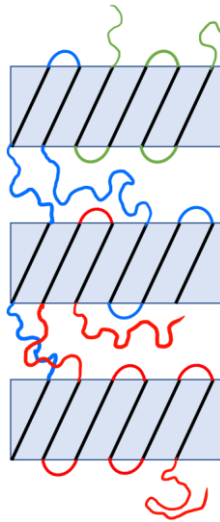
Figure 5.10: Schematic representation of the amorphous and crystalline phases. As seen for the low molecular weight green chain, most segments are mainly located in the crystalline phase. In the case of the blue and red chains, the fraction of segments located in the amorphous phase is higher than for the green chain (shorter chains are more easily included in crystalline structures). Due to the limited dynamics, only the amorphous part (shown as blue, red, and green) of the chains can form crosslinks with other chains. As it is seen, the longer chains have more chance to form crosslinks, whereas this probability is low for shorter chains (green chain). It has to be mentioned that if this chain even forms crosslinks, the number of crosslinks would be low, and most segments behave as dangling defects that eventually relax.

According to previous studies, the crystallinity and the crystallization rate of polyethylene chains increase (up to 90% crystallinity) with decreasing the average molecular weight [142,143]. This means that not only the short chains in polydisperse polyethylene tend to crystallize more fully, but also, they crystallize faster. In other words, for the low molecular weight chains, the fraction of segments placed in the crystalline region is much higher as compared to the longer chains. Therefore, shorter chains have a lower chance of making a chemical crosslink due to their higher crystallinity. In conclusion, increasing the number of low molecular weight chains in a polydisperse polymer system decreases the maximum network fraction obtained in high irradiation doses.

It is noted that a chain with just one crosslink to the network structure is not an elastically active chain, meaning that after its disengagement time, this chain moves isotropically and is considered a dangling chain in the fast-motion limit by

DQ NMR and rheology. Nevertheless, this chain is detected as part of the network structure in the gel content experiment.

The different kinds of possible defects were introduced in chapter 3. In the current system, the fraction of isotropic moieties in non-irradiated samples contains the dangling chain ends and the disengaged short chains. According to the explained minor role of short chains in the network structure, it is seen that the fraction of defects reported by DQ NMR is expected to reflect the fraction of short chains, which can hardly form a crosslink to the network.

By looking at figure 5.9 again, it is seen that by increasing the temperature in the B-HDPE-0 sample, the fraction of network-like protons gradually decreases, which is caused by the disengagement of the short chains. It can be concluded that because of the relatively higher population of short chains in the B-HDPE grade, the maximum gel content value of B-HDPE is less than the N-HDPE grade.

Figure 5.11 shows the gel content values as a function of irradiation dose. The averaged fraction of network-like protons accurately predicts the maximum gel content value. Also, the growth of the gel fraction in both samples is similar, while the maximum gel content is the main difference. In figure 5.11b, the normalized gel content (normalized with the maximum gel content value of each) values are plotted vs. irradiation dose. Both samples reach above 90% of the maximum accessible gel fraction at 84 kGy irradiation dose, then insignificant variations are seen. After 84 kGy, the relative gel fractions of the samples look identical.

a)
b)
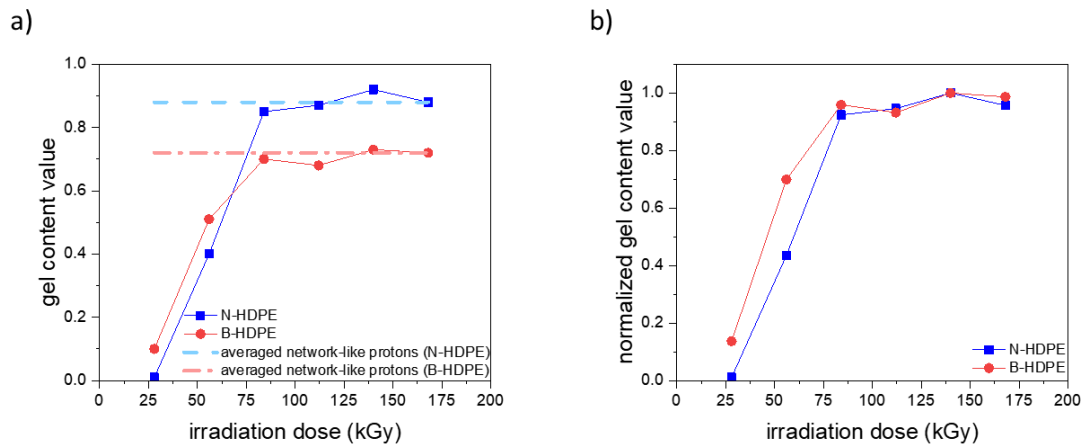
Figure 5.11: a) Gel content value as a function of irradiation dose in N-HDPEs and B-HDPEs. b) Normalized gel content value versus irradiation dose. The two HDPE grades show similar behavior in terms of normalized gel content values.

In the previous section, it was shown that the storage modulus and D_{res}, as the rheological and DQ NMR observables, are sensitive to the density of cross-links. As shown in figure 5.12, these observables increase with the irradiation dose, even in highly irradiated samples in which the gel content values do not vary significantly. On the contrary, it is observed that the rheological power-law exponents are more sensitive to the gel content value.

a)
b)
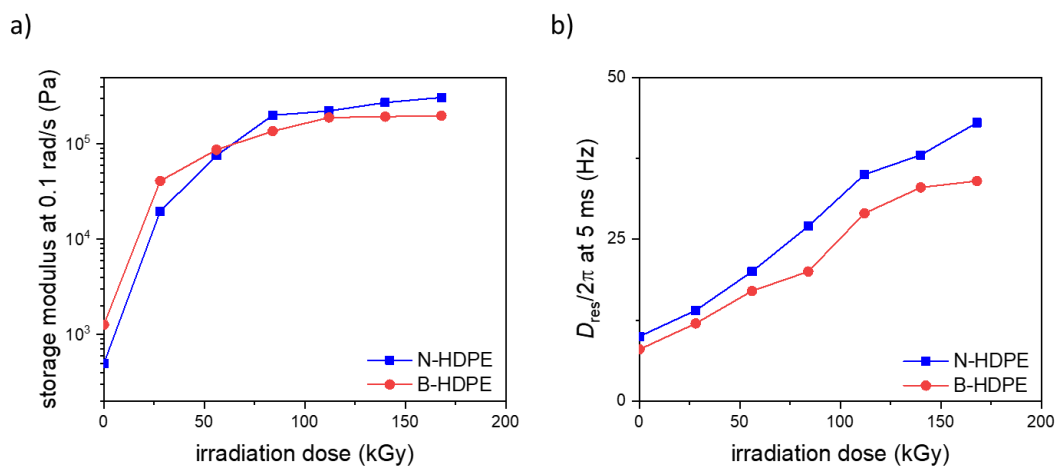
Figure 5.12: the dependency of a) the storage modulus at 0.1 rad/s and b) D_{res} at 5 ms on the irradiation dose in two HDPE grades.

Figure 5.13 shows the normalized gel content values against rheological and OACF power-law exponents, storage modulus and D_{res}. It is observed that a linear relation can be identified between the normalized gel content value and the rheological power-law exponent, unlike the case of the OACF power-law exponent, storage modulus and D_{res}. As shown, the rheological power-law exponent shows a weak dependency on the number of crosslinks whereas the OACF power-law exponent, storage modulus and D_{res} sensitively reveal the effect of further crosslinking,. This is a consequence of the different timescales probed by these methods (see figure 5.8). As seen in figure 5.13, the green line can linearly fit the data with an acceptable error according to the error bar of the normalized gel content values.
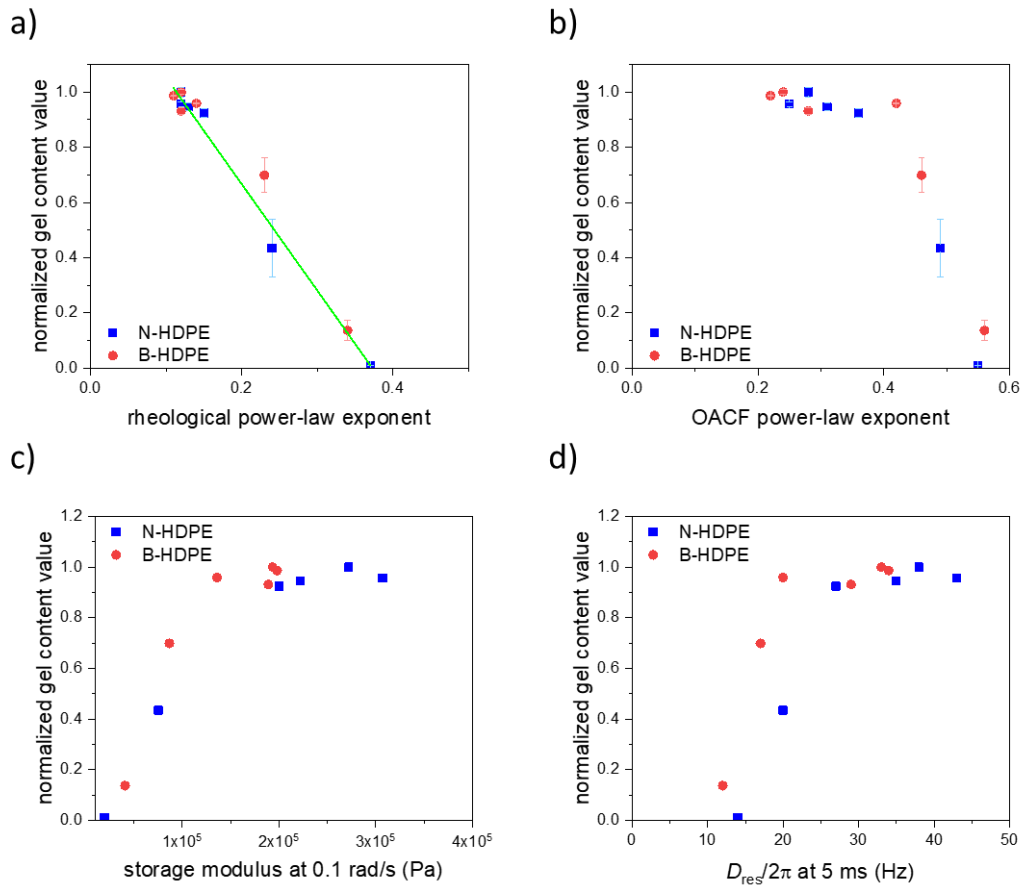
Figure 5.13: Normalized gel content value versus a) rheological power-law exponent, b) OACF power-law exponent, c) storage modulus at 0.1 rad/s and d) D_{res} at 5 ms . The green line is the best linear fit.

5.6. x-HDPEs in the semicrystalline state

Crystallization in polymers is governed by two processes, i.e., nucleation and growth which both slowdown with decreasing the undercooling, i.e. at higher temperatures. At high crystallization temperatures, the crystal growth becomes slow enough to see the effect of chain mobility on the crystallinity. Accordingly, the irradiated samples crystallized isothermally at 100 °C (where the crystal growth is slow and the chain mobility is mainly governed by the crosslinks) were probed by the FID decomposition approach (for more details, see chapter 3). In table 5.3, the main results of the FID decomposition method are summarized. It is observed that the crystallinity slightly decreases as the irradiation dose increases even in the samples with roughly the same amount of gel fraction. In conclusion, the chain dynamics are hindered due to the crosslinking, leading to a lower crystallinity at 100 °C at which the growth process is slow enough such that the crystallinity proceeds to a maximum governed by the crosslinking-induced constraints.

The NMR T_2 relaxation times of the intermediate and mobile parts, reflecting segmental mobility and constraints in the semicrystalline state, do not vary significantly by irradiation. The small changes in the relaxation times may be caused by the change in the overall crystallinity. It would be necessary to increase the temperature (higher than the melting point) to be in fast motion limit to see the influence of the cross-linking on the relaxation time associated with the mobile part ($T_{2,\ m}$). This means that the relaxation time is governed by the shorter-range segmental (Rouse) motion at the current temperature and is not reflecting the cross-links.

Table 5.3: The best-fit results obtained from FID decomposition for different irradiated samples.

samples	f_c	f_a	$T_{2,\,i}$ (μs)	$T_{2,\,m}$ (μs)	gel fraction
N-HDPE-0	0.78	0.1	58	206	0
X-N-HDPE-1	0.76	0.14	56	232	0.4%
X-N-HDPE-2	0.73	0.17	56	246	40%
X-N-HDPE-3	0.7	0.2	57	255	85%
X-N-HDPE-4	0.68	0.21	57	258	87%
X-N-HDPE-5	0.67	0.23	60	253	92%
X-N-HDPE-6	0.68	0.22	60	256	88%
B-HDPE-0	0.77	0.14	44	226	0
X-B-HDPE-1	0.76	0.15	49	250	10%
X-B-HDPE-2	0.73	0.18	47	248	51%
X-B-HDPE-3	0.71	0.2	47	263	70%
X-B-HDPE-4	0.69	0.2	50	269	68%
X-B-HDPE-5	0.67	0.22	51	282	73%
X-B-HDPE-6	0.67	0.22	54	293	72%

5.7. DQ NMR measurements on the extracted samples

The remaining network after extraction in the gel content experiment is probed in this part using DQ NMR. It needs to be mentioned that since only a tiny amount of the network remained, doing rheological measurements is not feasible. The AWPl model is used for studying the remainder network, similar to the irradiated samples. The comparison between the remainder networks and the corresponding irradiated samples in terms of constructed OACF and κ values is shown in figure 5.14.

The plots reveal that by removing the sol chains, the extracted network becomes more network-like, though the OACF still gradually decays in all the samples. This relaxation behavior confirms our argument about the trapped entanglements and branched or star polymer structure connected to the network that relaxes slowly and precludes the observation of a plateau. The growth of the network-like behavior can be seen not only by the visible increase in the OACF but also by decreasing the κ values of the remainder networks. It is also observed that both types of networks (remainder from the gel content test and diluted networks with defects) are approaching the same rubbery plateau at very short times on the left-hand side of the plots.
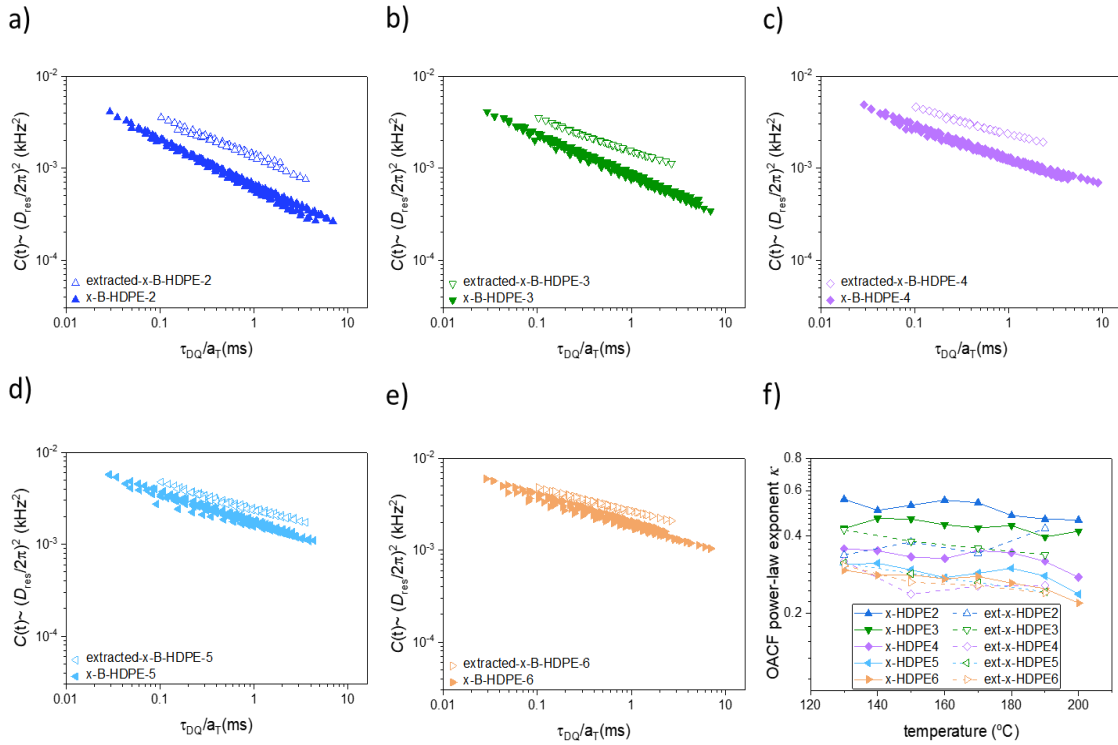
Figure 5.14: Comparing the extracted networks from the gel content experiment with the corresponding irradiated samples (before extraction) in terms of the OACF (a-e). f) The temperature dependency of the OACF exponent κ for the remainder network and irradiated samples (before extraction).

It must be noted that 50% of x-B-HDPE-2 chains have been removed via the gel extraction process, whereas this value is around 30% for other samples. This difference causes a significant drop in the κ values and a remarkable increase in the

OACF. By increasing the irradiation dose, the differences between the two types of networks (diluted and remainder networks) become insignificant. Also, the κ values and the OACF of the remainder networks from highly irradiated samples (>84kGy) are approximately identical, which confirms our argument that at very high irradiation doses, the cross-linking reaction and chain scission approach an equilibrium.

5.8. Summary

Two different grades of HDPE with broad and narrow poly-dispersity were crosslinked via electron beam irradiation. The irradiated samples were assessed using the gel-content experiment, rheological measurements, and low-field DQ NMR spectroscopy. According to the gel-content values, an equilibrium between chain scission and cross-linking reactions was observed upon increasing the irradiation doses. This equilibrium leads to a constant extractable fraction, whereas the degree of cross-linking increases slightly in the remainder of the sample. The rheological data shows a power-law behavior of the storage and loss moduli in the vicinity of the gel point.

Also, it was observed that the HDPE grade with narrower molecular weight distribution has a higher maximum gel content value than the grade with a broader distribution. The short chains in the broad molecular weight distribution sample tend to be in the crystalline structure more than the longer chains, so the possibility of making a crosslink for them becomes rather low. Consequently, a higher amount of non-network chains was measured for the sample with broader molecular weight distribution.

Two different approaches were applied to analyze the DQ NMR data. In the first approach, the system was considered a diluted permanent network with a large amount of defects distinguished into two components: isotropically mobile moieties and network-like segments. The data showed that due to the irradiation, the fraction of network-like protons increases, similar as the gel content value but with high sensitivity to distinguishing elastically active inner parts and dangling outer

parts. The residual dipolar coupling, characterizing the constraint density on the microscopic level, increases with irradiation over the whole sample series.

In the second approach, the partially cross-linked samples are considered a complex structure subject to temporary and permanent constraints with a broad relaxation spectrum resulting in a power-law correlation function, like an entangled polymer melt. Due to the consistency observed between the square-root of the correlation function amplitude characterizing D_{res} and the high-frequency limiting storage modulus, we showed that the DQ NMR data extend the frequency window of rheology by about two decades into 10 krad/s. In this range, where the transition from Rouse dynamics into developing elastic plateau can be addressed, a simple factor of 2 between the NMR-based power-law exponent and the rheological counterpart is confirmed.

The NMR-based fraction of network-like protons in the AWPl model showed the same value as the maximum gel fraction of the highly irradiated samples. It was shown that the NMR power-law exponent is sensitive to the number of cross-links and decreases continuously with irradiation. On the other hand, an empirical linear relation with gel fraction values is obtained based on the rheological power-law exponents.

By studying the remainder part from the gel content experiment, it was observed that even in such a network without any non-network-like chain, the OACF decays with time. It reveals the existence of trapped entanglements and branched polymers attached to the network structure, slowing down the relaxation of the defects. It is also understood that for determining the gel fraction of the irradiated HDPE, it is necessary to take into account the mentioned complex architecture of polymer chains in the model and consider the corresponding relaxation process to potentially be able to subtract it from the network structure. This is the motivation of the next chapter that the chain dynamics of a comb polymer is investigated by DQ NMR and rheology.

6. Chain dynamics in comb polyisoprene (PI)

In the following chapter, chain motions in a polymer comb with a molecular weight of 185 kg/mol (backbone Mw = 68 kg/mol, arm Mw = 13.8 kg/mol and the average number of arms per backbone = 8.5) are probed via rheology and DQ NMR and are analyzed according to the dynamic tube dilation (DTD) model. This model has been used to predict rheological responses of star and branched polymers with good precision based on the tube-model-related parameters. In this chapter, a DTD model developed for monodisperse comb polymers [72] has been used to fit the rheological responses. Then, we will investigate the separate contribution of arms and backbone and revisit their physical meaning. In the next part, DQ NMR data will be fitted based on the mentioned model with some necessary modifications, which will be discussed further.

According to the DTD model, a relaxed segment is considered an effective theta solvent (according to the Gaussian-chain assumption), and by its dilution effect, the remaining segments move in a dilated tube. Accordingly, it assumes a hierarchy of relaxation times depending on the segmental position and the fraction of relaxed segments. This means that the outermost segments relax much faster than the innermost segments and the relaxation of arms' segments is a prerequisite for the reptation motion of backbone chains.

In this work, by fixing the chain structure parameters (like the number of arms and the molecular weight of the arm and backbone), the obtained tube model-related constants, i.e., τ_e, entanglement time, and M_e, averaged entanglement spacing (averaged molecular weight between two entanglements) will be compared to the reported values by previous studies to assess the interpretation of the DTD as applied to NMR-based OACF.

It is noted that an identical sample (backbone Mw = 68 kg/mol, arm Mw = 13.8 kg/mol and the average number of arms per backbone = 8.5) with a deuterated

backbone were prepared to be probed with the DQ NMR. The goal was to assess the relaxation hierarchy of the arm's segments individually and investigate the possible difference in the dilution exponent with the backbone chains. Though it was recognized by analyzing the DQ NMR data that this sample unfortunately degraded during the experiment. The supplementary data regarding this sample are provided in the Appendices (part A).

6.1. Rheological measurements of comb PI

The rheological measurement of the comb PI sample has been done by Dr. Jonas Keller in the research group of Prof. Manfred Wilhelm at Karlsruhe Institute of Technology and is shown in figure 6.1. The master curve is constructed for $T_{\text{ref}} = 0$ °C using TTS and covers about seven decades.
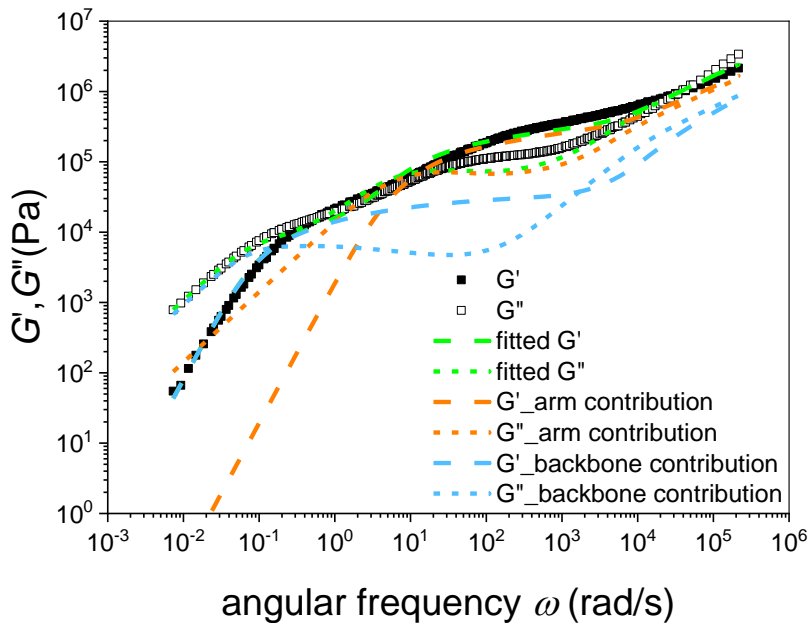
Figure 6.1: The rheological master curve constructed via TTS at a reference temperature of 0°C. The green lines correspond to the best-fit line based on the DTD model. The contribution of the arm and backbone segments are depicted separately.

At very high angular frequency, the Rouse relaxation can be seen, continuing into the entanglement rubbery plateau. In this regime, a hypothetical tube that represents the restriction applied by the neighboring chains is assumed. Since the arm's tube is perpendicular to the backbone, the reptation motion in the backbone

can be executed only after the relaxation of the arms. In the first plateau, the dynamic behavior is governed by the retraction motion of the arms and contour length fluctuation in the outer backbone segments. This regime lasts until the arms relax entirely and the backbone can start its reptation motion. This can be seen at the very low angular frequency when the chains enter the free-diffusionregime.

The DTD model explained in chapter 2 (according to equations 3.34-3.41) was applied to fit the rheological responses, using the known molecular weight and topological parameters. The best-fit values of G_N, τ_e, and M_e are listed in table 6.1.

Table 6.1: The best-fit tube parameters (obtained from fitting the rheological moduli at T_{ref} = 0°C according to the DTD model) and the reference values from previous works (The entanglement spacing is not a fitting parameter but is determined by G_0).

fitting parameter	best fit value	value from previous work[72,73]
G_0 (MPa)	0.39	0.36-0.44
τ_e (s)	$1.5*10^{-5}$	$0.7 - 1.5 * 10^{-5}$
M_e (g/mol)	4329	4000-5000

As seen in table 6.1, all the obtained parameters are in the range previously reported by other researchers. It is pointed out that M_e is not a fitting parameter but obtained based on $M_e = \frac{\rho RT}{G_0^N}$ according to Milner and McLeish [66]. According to the Doi and Edwards tube model, 1/5 of the stress is relaxed by the longitudinal Rouse motions. Therefore, the entanglement spacing would be 4/5 of their reported M_e [107]. This correction is applied to the obtained M_e in Table 6.1 to be comparable with the reference values.

Figure 6.1 also shows the best-fit model and the contributions of the backbone and arm in storage modulus. As observed, the best-fit storage and loss moduli fit the data with acceptable precision. By comparing the arms and backbone's contribution, it can be understood that the arm contribution fits the first plateau, whereas, after the relaxation of the arms, the storage modulus is governed by the backbone relaxation. If we look closely at the high frequencies, we see a significant difference between the contribution of arms and backbones.

According to the rubber elasticity and tube models, the plateau modulus is proportional to the number of entanglement strands per unit volume. As thoroughly discussed in chapter 2, the number of entanglements is assumed as a function of unrelaxed segment fraction in the DTD model. Therefore, each segment, whether in arms or backbone, is expected to take the same mechanical load at a specific time. The contribution of the backbone and arms in the moduli depends on the fraction of each. To remove this dependency, the storage modulus per segment is defined, i.e., the storage modulus contribution of the arms or backbone divided by the associated fraction, $G_{a,b}^{per\ segment} = \frac{G_{a,b}}{f_{a,b}}$. Since the mechanical behavior in the Rouse regime arises from the segmental motion shorter than the entanglement spacing, the storage modulus per segment should be identical for the backbone and arms, while in the limit of low frequencies, it should approach zero for arms. For a better understanding, figure 6.2 shows the ratio of the storage modulus per segment in the arms to the storage modulus per segment in a backbone.
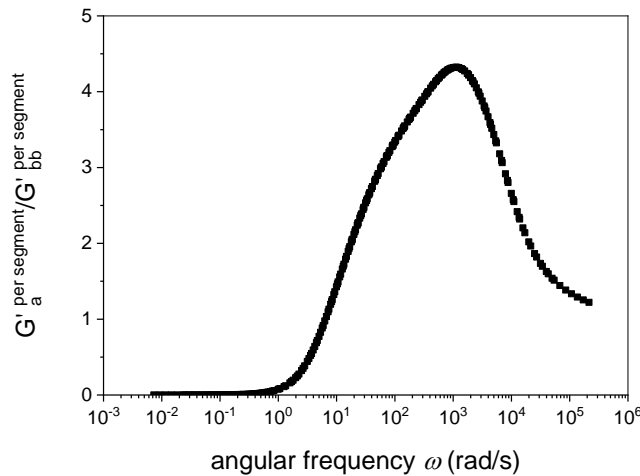
Figure 6.2: The ratio of storage modulus per segment in arms and backbone (contribution of arm segment in storage modulus per contribution of backbone segment in storage modulus) obtained from the best-fit model shown in Table 6.1 versus angular frequency.

As it is seen in figure 6.2, all the arm segments have indeed relaxed at low frequencies, and the ratio equals zero on the left-hand side of the plot. In the Rouse regime, this ratio is close to 1 at very high frequencies. At mid-range frequency, this ratio increases and passes a maximum. Considering that the backbone segments

relax much slower than the arms, the mentioned trend is physically not entirely reasonable. It is expected that the contribution of arm segments becomes weaker due to faster relaxation. This may indicate a shortcoming of the suggested interpretation of the DTD model for monodisperse comb polymers by McLeish et al. [73]. Thus, it can be concluded that the DTD model modified for comb polymers was built based on averaging and may not have physical meaning for the separated contributions.

The mentioned averaging follows from the suggested interpretation of the tube dilation by McLeish et al. [73] in a monodisperse comb polymer. They assume that when the backbone's segments start the relaxation process, the whole arms have already relaxed, which is correct. However, their model used the same unrelaxed-segments fraction for times shorter than the relaxation of the arms. In other words, a diluted modulus is used for backbone segments at high frequencies, which is incorrect. This problem results in an underestimation of the contribution of the backbone segments in storage and loss moduli. In the following, the interpretation of this method in fitting DQ NMR data will be assessed, keeping in mind this apparent shortcoming.

6.2. DQ NMR measurements of comb PI

The DQ NMR data is fitted with the NMR-modified DTD model explained in chapter 3. As seen in equation 3.34, an exponential correlation function is assumed for each segment with a unique relaxation time determined based on the segmental curvilinear dimensionless coordinate. It is assumed that the order parameter correlates with the inverse of entanglement spacing with the power of 1 or 1/2 (see chapter 3), but in this section, we only assume the power of 1 for checking the OACF.

In the DTD model modified for polymer comb, the unrelaxed-segments fraction of arms and backbone are $(1 - \varphi_a x_a)$ and $\varphi_b(1 - x_b)$, respectively. In other words, the unrelaxed segment fraction is written as a function of the segmental curvilinear dimensionless coordinate. Unlike for rheology, where the relaxed segments do not have any observable response, in DQ NMR, the relaxed segments show a slowly decaying signal tail at long times. Since the Anderson-Weiss approximation is not

accurate for isotropic moieties, a tail fraction should be defined for the relaxed segments. Accordingly, the segments with relaxation times shorter than the first recorded τ_{DQ} are considered defects with a long transverse relaxation time.

Table 6.2: The best-fit parameters resulting from the simultaneous fitting of the DQ NMR data at eight different temperatures using TTS. The parameter is reported at 25°C as the reference temperature

fitting parameter	best-fit value	value from previous work
τ_e (s)	$2*10^{-4}$	$0.7 - 1 * 10^{-5}$
M_e (g/mol)	3995	4000-5000

Table 6.2 lists the best-fit parameters obtained via fitting the DQ NMR data with the positional-dependent unrelaxed-segments fraction. It is seen that the entanglement spacing is close to the reference range; however, the entanglement equilibration time is approximately one order of magnitude slower than the reported values.
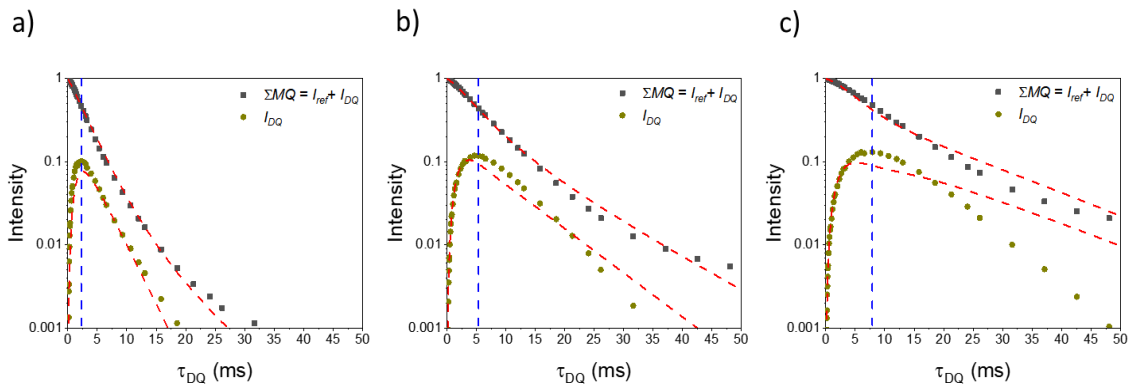
Figure 6.3: The simultaneous fitting of the DQ NMR data measured at a) 30°C, b) 60°C c) 90°C. It is noted that the data were measured at eight different temperatures, from 30°C to 90°C with 10°C intervals. The red and blue dashed lines show the best-fit model and the fitting interval of the DQ signal, respectively. Thus, the fit represents a prediction for times beyond the blue dashed line.

Figure 6.3 shows the simultaneous fitting of MQ and DQ signals measured at three different temperatures (30°C, 60°C, 90°C) using TTS at 0°C as the reference temperature. Since the Andersson-Weiss approximation is not accurate for long

experimental times, the DQ signals are fitted until the blue vertical line, marking the τ_{DQ} at which the maximum DQ intensity is read. The fraction of relaxed segments increases with increasing temperature due to the enhanced segmental dynamics. As it is observed, at 30°C, the best-fit line can fit the data in the fitting interval with good precision, whereas at higher temperatures, the fits are not precise, particularly in DQ signals around its maximum and in MQ signals at long times (tail signal).

Figure 6.4 demonstrates the constructed segmental OACF based on the best-fit parameters, shown in table 6.2. As it is highlighted on the time axis, more than five decades are covered by the DQ NMR technique using TTS. The highest OACF value belongs to the outermost segment of the arm, and the lowest one is associated with the segments relaxing via reptation motion in the backbone. At very short times in the left-hand side of figure 6.4, two orders of magnitude difference between the OACF associated with the outermost arm segment and innermost backbone segment is observed. Since the OACF is assumed to be proportional to the inverse of squared entanglement spacing, it means that the entanglement spacing in the innermost backbone part is ten times larger than in the outermost arm segments, which cannot be correct. The plotted OACF clearly illustrates the lack of physical meaning of the suggested interpretation of the DTD model [73] for monodisperse comb polymers.

In rheology, the model focused on fitting the first plateau by arm relaxation and the second one with backbone relaxation without any concern about the contribution of the backbone segments in the first plateau region. This leads to an underestimation of the backbone contribution. Though it is not an important problem in the rheology of a monodisperse comb, it provides a significant error for DQ NMR signals. Unlike the rheology, the magnitude of the OACF affects the NMR signal relaxation times and leads to a systematically shifted best-fit time constant, as seen in Table 6.2.
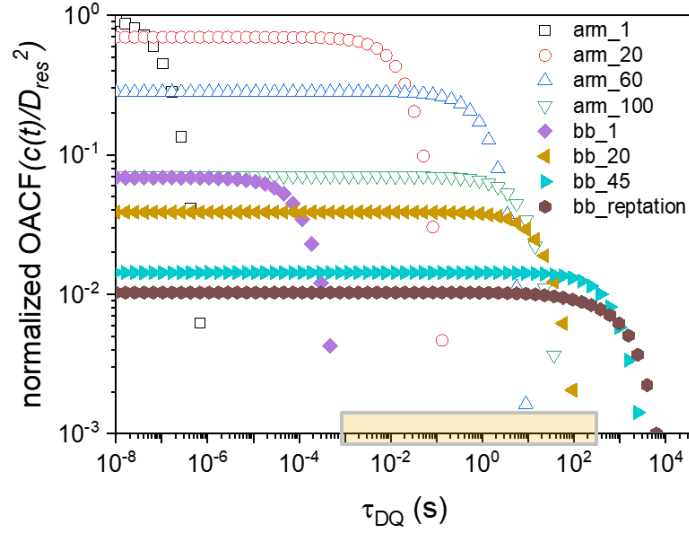
Figure 6.4: The segmental OACF based on the segmental position obtained at 0°C as reference temperature from the best-fit model shown in Table 6.2. the highlighted time axis shows the covered time range by DQ NMR data using TTS. In fitting the data, 100 segmental parts have been assumed in the arms and backbone.

Since this incorrect picture is the result of using time-independent unrelaxed-segments fraction $(\varphi_b{}^{\alpha+1}(1-s_b)^{\alpha}$ in the backbone), we now assume a time-dependent unrelaxed-segments fraction to fit the rheological and DQ NMR data in the following.

6.3. Time-dependent unrelaxed-segments fraction: rheology

In order to render the modeling of the correlation function more accurate, the unrelaxed-segments fraction can be determined as an explicit function of time. A time-dependent unrelaxed-segments fraction has in fact been used in the hierarchical relaxation model to study polydisperse branched polymer and the blend of linear and star polymers [80,105,144,145]. In the mentioned model, the potential of the arm retraction and backbone contour length fluctuation depends on the time-dependent unrelaxed segment fraction. In our case, as a monodisperse comb-polymer, it is not necessary to alter the relaxation time hierarchy because the segmental-position-dependent unrelaxed-segments fraction is valid for use in the potential function. We only need to define the time-dependent unrelaxed-segments fraction for use in moduli or correlation functions. The general expression for the time-dependent modulus is:

$$G(t) = \int_{\tau_i}^{\tau_f} \frac{\partial G_N(\tau)}{\partial \tau} \exp\left(\frac{-t}{\tau}\right) d\tau \tag{6.1}$$

Since the diluted modulus is defined as $G_N(\tau) = G_N^0 [\Phi(\tau)]^{\alpha+1}$, equation 6.1 turns into:

$$\begin{aligned}
G(t) &= G_N^0(1+\alpha) \int_{\tau_i}^{\tau_f} [\Phi(\tau)]^{\alpha} \exp\left(\frac{-t}{\tau}\right) \frac{\partial \Phi(\tau)}{\partial \tau} d\tau \\
&= G_N^0(1+\alpha) \int_0^1 [\Phi(\tau)]^{\alpha} \exp\left(\frac{-t}{\tau}\right) d\Phi
\end{aligned} \tag{6.2}$$

The Fourier transform of this expression to use for dynamical responses can be written as:

$$\frac{G'(\omega)}{G_N^0} = (1+\alpha) \int_0^1 \frac{\omega^2 t^2}{1+\omega^2 t^2} [\Phi(t)]^{\alpha} \, d\Phi(t) \tag{6.3}$$

$$\frac{G''(\omega)}{G_N^0} = (1+\alpha) \int_0^1 \frac{\omega t}{1+\omega^2 t^2} [\Phi(t)]^{\alpha} \, d\Phi(t) \tag{6.4}$$

The best-fit parameter obtained via time-dependent unrelaxed-segments fraction can be found in table 6.3. The model predicts the G_0, τ_e, and M_e in the same range reported by the previous works, illustrating the minor role of the unrelaxed-segments fraction.

Table 6.3: The best-fit parameters obtained via the fitting of rheological responses for $T_{ref} = 0°C$ based on the DTD model with time-dependent unrelaxed-segments fraction (equations 6.3, 6.4)

fitting parameter	best-fit value	value from previous work
G_0 (MPa)	0.35	0.36-0.44
τ_e (s)	$1.8 * 10^{-5}$	$0.7 - 1.5 * 10^{-5}$
M_e (g/mol)	4814	4000-5000

Figure 6.5 shows the rheological data and best-fit model according to equations 6.3 and 6.4. The best-fit line predicts the dynamic behavior of the polymer comb in the whole studied frequency range with satisfactory precision. The deviation from

experimental data is observed in the mid-range frequency in which the outermost part of the backbone and the innermost part of the arm relax simultaneously. This deviation has also been observed at the same frequency range in figure 6.1.
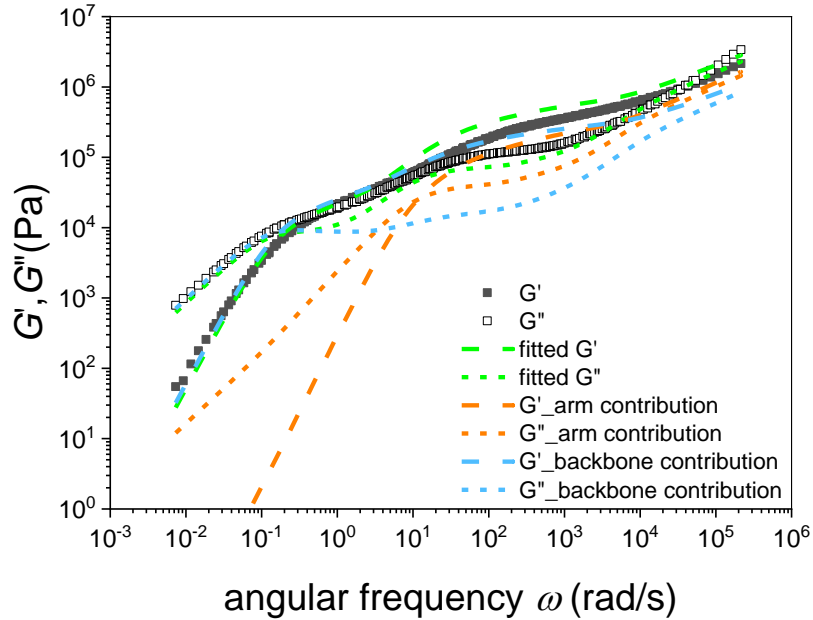
Figure 6.5: The rheological master curve constructed via TTS at a reference temperature of 0°C. The green lines correspond to the best-fit line resulting from the DTD model with time-dependent unrelaxed-segments fraction. The contribution of the arm and backbone segments are depicted separately.

At very high frequencies, the arm contribution in moduli is higher than the backbone's, which is understandable according to the higher fraction of arm segments. Due to the relaxation of arm segments, the arm contribution decreases and gradually disappears at very low frequencies. In this frequency range, the dynamic behavior is mainly governed by the backbone segments. As can be seen in figure 6.5, the current picture of the contributions of arm and backbone chains is now actually physically realistic.

Figure 6.6a shows the ratio of the storage modulus per segment in arms to the storage modulus per segment in the backbone against angular frequency. At very high frequencies, when the minority of arm segments has already relaxed, this ratio is close to unity. The arm relaxation speeds up at lower frequencies, and a decay is observed, leading to a plateau in the mid-range frequencies (5000 to 100 rad/s). This

plateau results from increasing the number of backbone segments relaxing via CLF in the mentioned frequency range. This can be seen clearly in figure 6.6b. At low frequencies, the reptation motion in the backbone becomes dominant, and the whole system enters the free-diffusion regime. This cannot be seen in figure 6.6a because the arm contribution disappears at 1 rad/s.

a)

b)
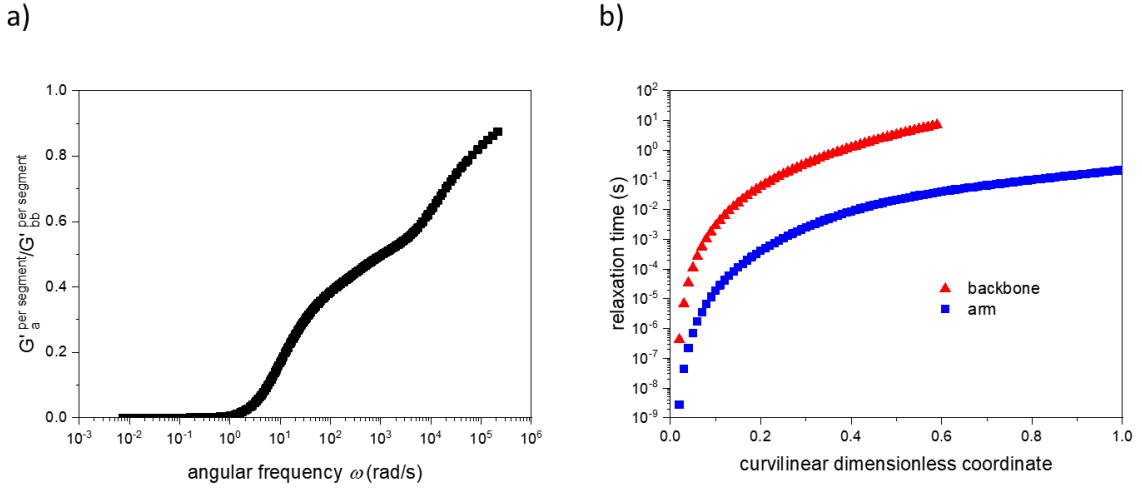
Figure 6.6: a) The ratio of storage modulus per segment in arms and backbone (contribution of arm segment in storage modulus per contribution of backbone segment in storage modulus) obtained from the best-fit model shown in Table 6.3 versus angular frequency. b) The hierarchy of the relaxation times according to the curvilinear dimensionless coordinate.

6.4. Time-dependent unrelaxed-segments fraction: DQ NMR

As discussed so far, for fitting the DQ NMR data according to the DTD model, it is necessary to use time-dependent unrelaxed-segments fraction. This time-dependent fraction can be written as:

$$\Phi(t) = \varphi_a \left[\int_0^1 \exp\left(-\frac{t}{\tau(x_a)}\right) dx_a \right] + \varphi_b \left[\int_0^{x_d} \exp\left(-\frac{t}{\tau(x_b)}\right) dx_b + (1 - x_d) \right] \quad (6.5)$$

It is divided into the arm and backbone segments. In arms, the only relaxation process is arm retraction, whereas, in the backbone, the outer part of the chain relaxes via the CLF process, and the inner part (from x_d to 1) follows reptation motion.

Since the chains are considered a set of segments, the integral can be transformed into a summation:

$$\Phi(t) = \varphi_a \left[\frac{1}{n} \sum_{i=1}^{n} \exp\left(-\frac{t}{\tau\left(\frac{i}{n}\right)} \right) \right] + \varphi_b \left[\frac{1}{n} \sum_{i=1}^{n_d} \exp\left(-\frac{t}{\tau\left(\frac{i}{n}\right)} \right) + (1 - x_d) \right] \tag{6.6}$$

The reptation motion is the final relaxation process, which means the innermost of the backbone $(1 - x_d)$, relaxes after the relaxation of all other segments. By replacing the unrelaxed-segments fraction into equation 3.32, the OACF becomes:

$$C(t, x_{a,b}) = S_{b,0}^{2} \left[\varphi_a \frac{1}{n} \sum_{i=1}^{n} \exp\left(-\frac{t}{\tau\left(\frac{i}{n}\right)} \right) + \varphi_b \frac{1}{n} \sum_{i=1}^{n_d} \exp\left(-\frac{t}{\tau\left(\frac{i}{n}\right)} \right) \right.$$
$$\left. + (1 - x_d) \right]^{\beta} \exp\left(-\frac{t}{\tau(x_{a,b})} \right) \tag{6.7}$$

The above equation represents the OACF based on the DTD model with a time-dependent unrelaxed-segments fraction. As discussed in chapter 3, β can be equal to α or 2α (depending on the relation between the order parameter and the entanglement spacing).

In chapter 3, it was extensively explained that for determining the signal functions, the phases during DQ NMR time evolution are determined by an integral over this time (resulting from AW approximation). To have explicit signal functions, we have to rewrite the OACF in the form of a summation of single exponential functions (to be able to solve the integrals analytically); otherwise, we have to fit the data by determining the signal functions via lengthy numerical integration.

It is clear that for non-integer values of β, the integrals cannot be solved analytically. Moreover, for $\beta=2$, the number of terms increases significantly, and the numerical approach would probably be a better option (in the case of expanding the summation like what we will do for $\beta=1$). Nevertheless, for $\beta=1$, the OACF can be written as the summation of a finite number of exponential functions:

$$C(t, x_{a,b}) = S_{b,0}{}^2 \varphi_a \frac{1}{n} \sum_{i=1}^{n} \exp\left(-\frac{t}{\tau_a\left(\frac{i}{n}\right)}\right) \exp\left(-\frac{t}{\tau(x_{a,b})}\right)$$

$$+ S_{b,0}{}^2 \varphi_b \left[\frac{1}{n} \sum_{i=1}^{n_c} \exp\left(-\frac{t}{\tau_b\left(\frac{i}{n}\right)}\right) \exp\left(-\frac{t}{\tau(x_{a,b})}\right)\right. \tag{6.8}$$

$$\left. + (1 - x_d)\exp\left(-\frac{t}{\tau(x_{a,b})}\right)\right]$$

Then, two exponentials, multiplied within the summation, can be replaced by the summation of a single exponential:

$$C(t, x_{a,b}) = S_{b,0}{}^2 \varphi_a \frac{1}{n} \sum_{i=1}^{n} \exp\left(-\frac{t}{\zeta_a(x_{a,b}, i)}\right)$$

$$+ S_{b,0}{}^2 \varphi_b \left[\frac{1}{n} \sum_{i=1}^{n_c} \exp\left(-\frac{t}{\zeta_b(x_{a,b}, i)}\right) + (1 - x_d)\exp\left(-\frac{t}{\tau(x_{a,b})}\right)\right] \tag{6.9}$$

And $\zeta_a(x_{a,b}, i)$ and $\zeta_b(x_{a,b}, i)$ are defined as:

$$\zeta_a(x_{a,b}, i) = \frac{\tau_a\left(\frac{i}{n}\right) \cdot \tau(x_{a,b})}{\tau_a\left(\frac{i}{n}\right) + \tau(x_{a,b})} \tag{6.10}$$

$$\zeta_b(x_{a,b}, i) = \frac{\tau_b\left(\frac{i}{n}\right) \cdot \tau(x_{a,b})}{\tau_b\left(\frac{i}{n}\right) + \tau(x_{a,b})} \tag{6.11}$$

To avoid misunderstanding, it needs to be mentioned that the fraction of unrelaxed segments and, accordingly, the order parameter only correlate with time and are identical for all segments. Nevertheless, when the summation is expanded and multiplied into the relaxation of one specific segment (whether in the arm or backbone), this OACF function is only valid for that specific segment.

According to the rewritten form of the OACF, the signal functions can be obtained according to the equations 3.35, 3.36:

$$I_{DQ}\left(\tau_{DQ}, \zeta_{a,b}(x_{a,b}, i),\ \tau_{a,b}(x_{a,b}), D_{res}\right)$$

$$= \exp\left\{0.4 D_{res}{}^2 \left[\varphi_a \sum_{i=1}^{n} \zeta_a(x_{a,b}, i)^2 \left(e^{-\frac{\tau_{DQ}}{\zeta_a(x_{a,b}, i)}} + \frac{\tau_{DQ}}{\zeta_a(x_{a,b}, i)} - 1\right)\right.\right.$$

$$+ \varphi_b \sum_{i=1}^{n_d} \zeta_b(x_{a,b}, i)^2 \left(e^{-\frac{\tau_{DQ}}{\zeta_b(x_{a,b}, i)}} + \frac{\tau_{DQ}}{\zeta_b(x_{a,b}, i)} - 1\right)$$

$$\left.\left. + \varphi_b(1 - x_d)\tau(x_{a,b})^2 \left(e^{-\frac{\tau_{DQ}}{\tau(x_{a,b})}} + \frac{\tau_{DQ}}{\tau(x_{a,b})} - 1\right)\right]\right\}$$

$$\times \sinh\left\{0.2 D_{res}{}^2 \left[\varphi_a \sum_{i=1}^{n} \zeta_a(x_{a,b}, i)^2 \left(e^{-\frac{2\tau_{DQ}}{\zeta_a(x_{a,b}, i)}} - 2e^{-\frac{\tau_{DQ}}{\zeta_a(x_{a,b}, i)}} + 1\right)\right.\right.$$

$$+ \varphi_b \sum_{i=1}^{n_d} \zeta_b(x_{a,b}, i)^2 \left(e^{-\frac{2\tau_{DQ}}{\zeta_b(x_{a,b}, i)}} - 2e^{-\frac{\tau_{DQ}}{\zeta_b(x_{a,b}, i)}} + 1\right)$$

$$\left.\left. + \varphi_b(1 - x_d)\,\tau(x_{a,b})^2 \left(e^{-\frac{2\tau_{DQ}}{\tau(x_{a,b})}} - 2e^{-\frac{\tau_{DQ}}{\tau(x_{a,b})}} + 1\right)\right]\right\}$$

(6.12)

$$I_{\Sigma MQ}\left(\tau_{DQ}, \zeta_{a,b}(x_{a,b}, i), \tau(x_{a,b}), D_{res}\right)$$

$$= exp\left\{0.2 D_{res}{}^2 \left[\varphi_a \sum_{i=1}^{n} \zeta_a(x_{a,b}, i)^2 \left(4e^{-\frac{\tau_{DQ}}{\zeta_a(x_{a,b}, i)}} - e^{-\frac{2\tau_{DQ}}{\zeta_a(x_{a,b}, i)}}\right.\right.\right.$$

$$\left. + \frac{2\tau_{DQ}}{\zeta_a(x_{a,b}, i)} - 3\right)$$

$$+ \varphi_b \sum_{i=1}^{n_d} \zeta_b(x_{a,b}, i)^2 \left(4e^{-\frac{\tau_{DQ}}{\zeta_b(x_{a,b}, i)}} - e^{-\frac{2\tau_{DQ}}{\zeta_b(x_{a,b}, i)}} + \frac{2\tau_{DQ}}{\zeta_b(x_{a,b}, i)} - 3\right)$$

$$\left.\left. + \varphi_b(1 - x_d)\,\tau(x_{a,b})^2 \left(4e^{-\frac{\tau_{DQ}}{\tau(x_{a,b})}} - e^{-\frac{2\tau_{DQ}}{\tau(x_{a,b})}} + \frac{2\tau_{DQ}}{\tau(x_{a,b})} - 3\right)\right]\right\}$$

(6.13)

The signal function predicts the signal of a segment located in a specific dimensionless coordinate *x,* whether in the arm or backbone. The overall signal would be the sum of all proton signals of the segments in arms and backbone.

$$I_{DQ}{}^{overall} = \varphi_a \sum_{j=1}^{n} I_{DQ}{}^{arm}\left(\tau_{DQ}, \zeta_{a,b}\left(\frac{j}{n}, i\right), \tau_a\left(\frac{j}{n}\right), D_{res}\right)$$

$$+ \varphi_b \left[\sum_{i=1}^{n_d} I_{DQ}{}^{backbone,CLF}\left(\tau_{DQ}, \zeta_{a,b}\left(\frac{j}{n}, i\right), \tau_b\left(\frac{j}{n}\right), D_{res}\right) \right. \tag{6.14}$$

$$\left. + (1 - x_d)I_{DQ}{}^{backbone,reptation}\left(\tau_{DQ}, \zeta_{a,b}(x_d, i), \ \tau_d(x_d), D_{res}\right) \right]$$

$$I_{\Sigma MQ}{}^{overall} = \varphi_a \sum_{i=1}^{n} I_{\Sigma MQ}{}^{arm}\left(\tau_{DQ}, \zeta_{a,b}(x_a, i), \tau(x_a), D_{res}\right)$$

$$+ \varphi_b \left[\sum_{i=1}^{n_d} I_{\Sigma MQ}{}^{backbone,CLF}\left(\tau_{DQ}, \zeta_{a,b}(x_b, i), \tau(x_b), D_{res}\right) \right. \tag{6.15}$$

$$\left. + (1 - x_d)I_{\Sigma MQ}{}^{backbone,reptation}\left(\tau_{DQ}, \zeta_{a,b}(x_d, i), \ \tau_d(x_d), D_{res}\right) \right]$$

In table 6.4, the best-fit model parameters are listed for different α, β, and p values. For β values other than 1, the fittings were done via time-consuming numerical integration. Unlike rheology, the entanglement spacing is a fitting parameter in the DQ NMR data because for writing an explicit relation between D_{res} and entanglement spacing according to equation 3.7, the k and D_{stat} values need to be determined via molecular simulation by simplified assumptions. In this light, the determined values are model-dependent and may systematically deviate from rheology results.

Table 6.4: The tube model parameters obtained by fitting the DQ NMR data via the DTD model with time-dependent unrelaxed-segments fraction.

Parameters	D_{res} (Hz)	τ_e (s)	M_e (g/mol)
$a = 4/3$			
$p^2 = 1/12$	294	$1.6 * 10^{-6}$	2584
NMR_$\beta = 1$			
$a = 1$			
$p^2 = 1/40$	287	$1 * 10^{-5}$	4154
NMR_$\beta = 1$			
$a = 1$			
$P^2 = 1/12$	251	$1.8 * 10^{-5}$	3822
NMR_$\beta = 1$			
$a = 4/3$			
$P^2 = 1/12$	279	$1.9 * 10^{-6}$	1754
NMR_$\beta = 2.66$			
$a = 1$			
$P^2 = 1/40$	291	$1.6 * 10^{-6}$	2115
NMR_$\beta = 2$			
Ref. Value	----	$0.7 - 1.5 * 10^{-5}$	4000-5000

In all the fittings, obtained D_{res} values are in a narrow range, while the other fitting parameters vary more strongly. Comparing the best-fit parameters with the reference data obtained in previous studies shows that the fittings with $\beta = 1$ provide consistent results. Surprisingly, the theoretical NMR-based $\beta = 2$ (or 8/3) failed to predict the PI-comb's dynamics. The latter exponent value has been obtained (was discussed in chapter 3) based on the relation between the order parameter and entanglement spacing (in polymer melts) or crosslink density (in polymer networks), while $\beta = 1$ has been taken from the analogy between the current system and a lowly

cross-linked polymer network studied by Lang and Sommer [136]. They reported that according to the molecular simulation, the order parameter of an entangled chain between two crosslinks correlates with the inverse square root of entanglement spacing and the number of segments between two crosslinks ($S_b \propto 1/\sqrt{N\,N_e}$), which deviates from the classical relation of the order parameter, $S_b \propto \frac{1}{N} + \frac{1}{N_e}$. Our results showed that the linear relation between the order parameter and the inverse of the entanglement spacing is indeed not fully correct. It is noted that the analogy used here is valid for backbone segments over a wide time range, while it may not be entirely correct for the arms relaxing from a free end.

Figure 6.7 shows the normalized OACF constructed using TTS by fitting DQ NMR data with time-dependent unrelaxed-segments fraction over almost 12 decades. Unlike the previous fitting approach (time-independent unrelaxed-segments fraction), it is seen that all the segments have an identical OACF until they start the relaxation process via arm retraction, CLF, or reptation. The relaxation starts from the outermost segments of the arms. As the innermost arm segment relaxes, the second plateau appears, which is governed by the inner parts of the backbone. In longer times, the whole chain relaxes via reptation.
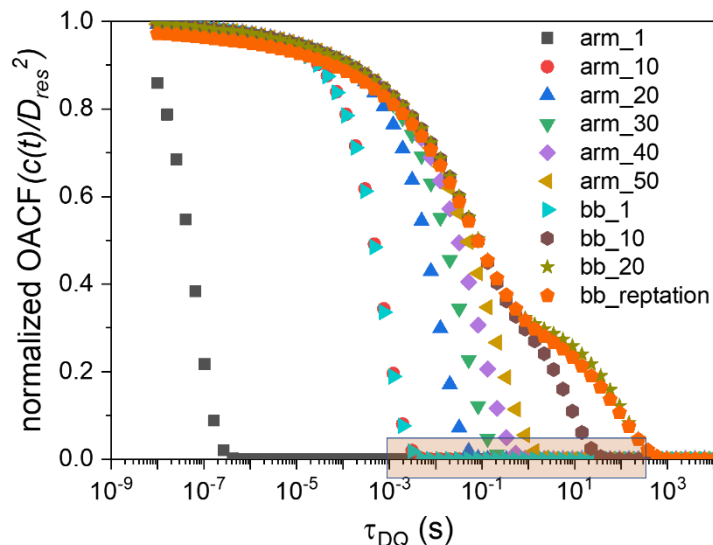
Figure 6.7: The segmental OACF based on the curvilinear dimensionless coordinate obtained at 0°C as reference temperature from the best-fit model shown in Table 6.4 ($a = 1$, $p^2 = 1/40$, NMR_$\beta = 1$). The highlighted time axis shows the covered time range by DQ NMR data using TTS. In fitting the data, 50 segmental parts have been assumed in summating for arms and backbone.

6.5. Summary

The chain dynamics of a polyisoprene comb were studied via rheology and DQ NMR. The data was analyzed using the DTD model, which predicted the chain dynamics in star and branched polymers. The core of this theory is that the dilution effect arises from the relaxed chains, increasing the entanglement spacing and tube diameter. However, the DTD model predicted the rheological behavior of the sample perfectly, but it is observed that the contribution of the backbone segments in storage modulus is significantly underestimated at high frequencies. In DQ NMR data, this leads to an unrealistic picture of the OACF when the arm segments are mainly not relaxed.

This problem arises from the assumption that considers the unrelaxed-segments fraction as a function of segmental dimensionless coordinate (time-independent function). This was modified by considering a time-dependent unrelaxed-segments fraction in the DTD model. Via this modification, the DTD model predicted the rheological behavior with a correct contribution of arm and backbone in storage modulus in the studied frequency range.

Since the relation between the OACF as the DQ NMR observable and the diluted entanglement spacing was unknown for the studied system, two possible scenarios were considered to fit the DQ NMR data. The results demonstrated that the classical relation between the order parameter and entanglement spacing is not valid in the case of a polymer comb system. Moreover, our results confirm the findings of Lang and Sommer [136], who reported that the order parameter correlates with the square-root of entanglement spacing in a lowly crosslinked polymer system.

The results showed that the DQ NMR technique can be used for probing the branched and star polymers via the DTD model. DQ NMR probes the chain dynamics on a timescale being one decade and a half faster than rheology. Moreover, the segments with very fast relaxation times (faster than the studied time window) can be probed in the MQ signal (as a tail signal). Since in polyolefins, the segmental dynamics are fast, and the rheological measurement is restricted by the crystallization of the chains at low temperatures, the DQ NMR experiment can be a complementary technique to assess these polymeric systems. The current research represents the first attempt to apply the DTD model in the DQ NMR technique. Therefore, the results can be used in further investigations on the other systems using the DQ NMR technique.

7. Summary

Characterizing polymer systems with complex architecture is a challenge in the polymer industry. The current methods usually rely on using hazardous solvents at high temperatures, making these methods pricey and unsafe. Therefore, there is a clear demand for an alternative efficient method. The core idea of the given thesis was to combine rheology and DQ NMR techniques to map out the chain dynamics precisely in complex polymer structures. In the case of polyolefins, the primary concern of our research, this combined method becomes more essential due to the limited probed frequency or time range imposed by the crystallization. Regarding chain dynamics, two systems, including a partial network and a polymer comb, were probed via rheology and DQ NMR.

As the first system, two grades of HDPE with different polydispersity were irradiated by electron beam at different doses. The crosslinking efficiency was assessed via gel content experiment, rheology, and DQ NMR. The gel fraction evolution is similar in both grades according to the gel content values. Due to the irradiation, the gel content values increase significantly at low irradiation doses, but above 84 kGy, the changes are insignificant. Via constructed OACF of the remainder network from gel content experiments obtained via DQ NMR measurements, it was revealed that beyond 84 kGy, chain scission reactions become dominant, and the crosslinking reaction keeps increasing in the remainder of the samples. Though, at very high irradiation doses, the number of crosslinks remains constant.

In the rheological measurements, the characteristic scaling law in the vicinity of the gel point was observed for all irradiated samples. Even in x-N-HDPE-1, which did not have any non-extractable gel content value, the significant amount of branched polymer structure leads to scaling-law behavior. It was seen that even in highly irradiated samples, the storage modulus decays continuously, which confirms the existence of the coupled defects in the network structure.

Two different approaches were applied to evaluate the DQ NMR data. It was observed that the model, which assumed the irradiated sample as a polymer melt with a broad spectrum of relaxation time as a consequence of being restricted by permanent and temporary topological constraints, provides more consistent results with the rheology and gel content experiment. D_{res}, as the core NMR observable, correlates with the storage modulus at different irradiation doses. Moreover, the OACF exponent κ reflected the effect of crosslinking on the chain dynamics. As for rheology, the gradual decay in highly irradiated samples was observed in the constructed OACF, which confirmed the existence of the trapped entanglements and branched polymer structures. A simple and expected factor of 2 in the obtained NMR-based OACF exponent κ and the rheological counterpart is confirmed by a direct comparison of the rheological and DQ NMR measurements. It was shown that the frequency window of rheology can be extended by about two decades into the 10 krad/s range via DQ NMR data.

In the extracted network from the gel content tests, the decay in the OACF was observed, which reveals that some of the complex architectures (star and branched polymers) are connected to the network structure via chemical bonds and relax slowly via Rouse motion, which has been observed in the irradiated network in rheology and DQ NMR-based OACF. According to the observed results, it is necessary to predict the chain dynamics of the branched polymers (either connected or not connected to the network) to develop a precise approach to assess these kinds of network structures.

Concerning observations in partially network polyethylene and the importance of the characterization of the complex polymer architectures, the chain dynamics in a polyisoprene comb as a defined model system were probed via rheology and DQ NMR. The rheological moduli of the comb-PI were well analyzed using the DTD model, which considers the constraint release effect of the relaxed segments as the dilation of the tube (leading to an increase in the tube diameter and entanglement spacing). However, we identified an unrealistic relative contribution of arm vs. backbone segments in rheological moduli and NMR-based OACF, leading to the suggestion of a time-dependent unrelaxed-segments fraction rather than a time-independent one (time independent at times shorter than the corresponding

relaxation time). By using the time-dependent unrelaxed-segments fraction, DQ NMR as well as rheology, predicts the dynamic behavior of the comb-PI over five decades of time via TTS newly quantitatively.

The correlation between the unrelaxed-segments fraction and OACF was investigated. It was shown that the order parameter correlates with the inverse square root of the entanglement spacing in polymer combs which confirms the findings of Lang and Sommer [136] in lowly crosslinked systems, though this may not be valid for the arms due to their free ends. Further works on the analogous systems are necessary to clarify the relation between order parameters and the unrelaxed-segments fraction.

A central goal of the given thesis was to introduce a safe and economically efficient method to assess the crosslinking reaction in irradiated polyethylene. It was shown that there is an empirical relation between the gel content values and the rheological power-law exponent. Though, the gel content values and rheological power-law exponent are insensitive to the density of crosslinks being important in highly irradiated samples (after reaching the maximum gel content value). On the other hand, DQ NMR observables (D_{res} and κ) clearly illustrate the effect of the post crosslinking and local overcrosslinking in highly irradiated samples on the chain dynamics, unlike to gel content experiment.

According to our findings, distinguishing the chain dynamics of entangled (particularly branched) defects and the network structure to precisely determine the gel content with DQ NMR in irradiated PE requires an accurate prediction of the dynamic behavior of the entangled and thus relaxing defect. For this purpose, along with the presented results in this thesis for monodisperse PI-comb, studying the polydisperse branched polymers with the DQ NMR technique is a viable option. For a partially crosslinked network, the suggested correlation function should be a combination of a plateau (the A-l model) representing the network structure and a hierarchy of relaxation times (the AWexp model) for entangled defects (branched polymer structures). It is noted that considering polydispersity in the mentioned DTD model for use in DQ NMR measurements leads to complex equations and time-consuming fitting procedures that are not readily available for routine use.

Appendices

A. Supplementary DQ NMR data for backbone-deuterated PI-comb:

A backbone deuterated PI-comb with identical architectures as the sample probed in chapter 6 was studied via DQ NMR.
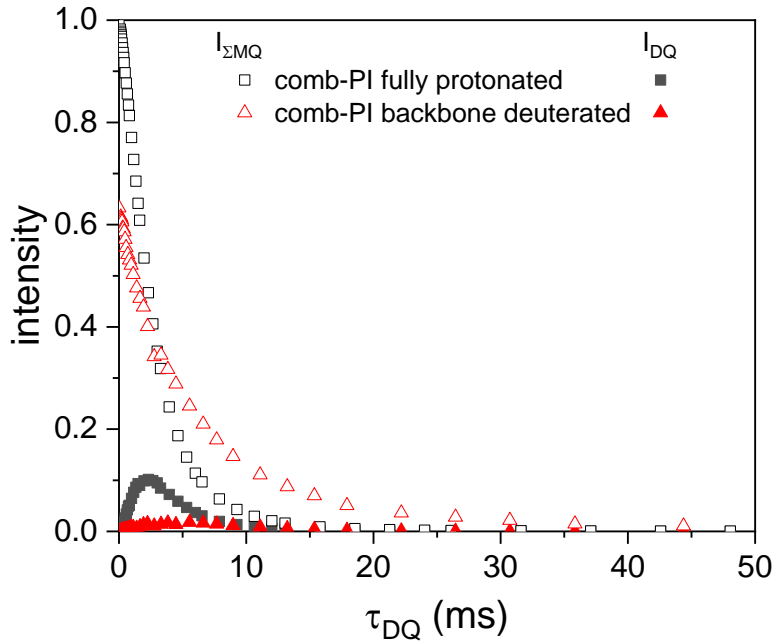
Figure A.1: DQ NMR data for two identical protonated and deuterated samples. As 63% of the signal comes from arms' segments, the signal from the backbone-deuterated sample multiplied to 0.63 to be comparable with the fully protonated sample.

It is seen in figure A.1 that the build-up curve in the fully protonated sample is much higher than in the deuterated one. Also in the $I_{\Sigma MQ}$ signal the amount of isotropically mobile material (slowly decaying signal at long times) is much higher in the deuterated sample. By considering the fraction of the arms' segments, it is possible to subtract the contribution of the arms' signal, but it is observed at around 5 ms that the $I_{\Sigma MQ}$ signal in the deuterated sample is significantly higher than the signal obtained from the fully protonated sample (by considering the fraction of arm protons in the PI-comb). This means that by subtraction of the arms' signal, we would obtain a negative signal, which does not have any physical meaning.

Therefore, this shows that the deuterated sample is not identical to the fully protonated sample and probably is degraded. Since only a few milligrams of this sample were produced to be probed by DQ NMR, it was not possible to probe the possible degradation of this sample with standard methods.

B. Python codes for fitting DQ NMR data based on the AWPl model

The code needs the DQ data as a text file in a folder. By giving the address of the folder, the code automatically finds text files (data) and makes a new folder with the file's name, and saves all results in that folder.

"
```
def weight_dist_AWPL_twocomp(inputaddress, output):
    n = 50 # number of points for distribution calculation
    outputadress = output + "\weighted-distribution-PWLW-twocomp-SQRT-Norm"
    if not os.path.exists(outputadress):
        os.makedirs(outputadress)
    # ASSIGN DIRECTORY FOR SAVING THE FIGURE
    my_path = os.path.abspath(outputadress)
    # READING THE TEXT FILE AND COPY IT TO DATA
    data = np.loadtxt(inputaddress)
    xmq = data[:, 0]
    x = data[:, 0]
    # IN XDQ WE OMIT ZERO, THE BOUNDRY IS NOT ACCOUNT TO AND IT IS CORRECT
    dq = abs(data[:, 2])
    maxim = np.where(dq == np.amax(dq))
    maxdq = np.amax(dq)
    # limited the fitting interval to the DQ maximum
    i= 1
    while dq[i] < 1 * maxdq:
        i+=1
    boundry = i
    xdq = data[1:boundry,0]
    ref = abs(data[:, 1])
    # NORMALIZING THE DATA
    mq = dq+ref
    maximum = mq[0]
    mq = (mq/maximum)
    dq = (dq/maximum)
    mqreal = mq
    maxdq = maxdq/maximum
    normalization_factor = 1
    dqreal = np.zeros(len(dq), dtype=float)
    for i in range (len(dq)):
        dqreal[i]=(dq[i])
```

```
    xmqreal=xmq
    MQ = np.zeros(len(mq), dtype=float)
    for i in range (len(mq)):
        MQ[i]=(mq[i])** (1/root)
# zero can not be measured. So it assumed very close to zero
    xmq[0]= 0.000000000001
    # DELETING UNDESIRED POINT FOR FITTING
    length = len(dq)
    i =length - boundry
    dq = dq[:-i]
    dq = dq[1:]
    DQ = np.zeros(len(dq), dtype=float)
    for i in range (len(dq)):
        DQ[i]=(normalization_factor * dq[i])**(1/root)
    boundry-=1
    global ML, Dres_ML, kap_ML, f1_ML, sigma_ML, T1_ML, T2_ML
    if not ML:
        Dres_ML = firstDres
        kap_ML = firstkappa
        f1_ML = 0.85
        sigma_ML = 1
        T1_ML = firstT1
        T2_ML = 50
    pi = np.pi
    t0= xdq[0]-0.00001
    b1= 1
    b2= 1
    Dres2 = 0
    print (f1_ML)
    #DEFINING VARIABLES AND INITIAL VALUES FOR FITTING
    x_1, x_2, y_1, y_2 = variables('x_1, x_2, y_1, y_2')
    f1 = sf.Parameter('f1',value= f1_ML, min=0.001, max=0.999)
    Drs1 = sf.Parameter('Drs1',value=Dres_ML, min=0.001, max=4)
    sigma1 = sf.Parameter('sigma1',value=sigma_ML ,min=0.000001, max=5)
    kappa = sf.Parameter('kappa',value= kap_ML, min=0.00005, max= 3)
    T1 = sf.Parameter('T1',value= T1_ML, min=0.01, max=100000000)
    T2 = sf.Parameter('T2',value= T2_ML, min=0.1, max=8000)
    res1=0
    norm1=0
    resmq=0
    lnDres1= sf.log(Drs1)
    for i in range(0,n+1):
        lnDtemp1= (lnDres1+ ((i-(n/2))*3*sigma1/(n/2)))
        Dres1= sf.exp(lnDtemp1)
        gauss1= sf.exp(-0.5*((i-(n/2))*3/(n/2))**2)/(sf.sqrt(2*pi*(sigma1**2)))
        res1= res1+ f1 * gauss1* ((sf.exp(-(x_1/T1)**b1)* sf.exp( -(0.2*(2*pi*Dres1)**2)/((kappa-
2)*(kappa-1))*(kappa*(2*(kappa-2)*x_1/t0-(kappa-1))*t0**2 + 2*x_1**(2-kappa)*t0**kappa) )*
sf.sinh( 0.5*(0.2*(2*pi*Dres1)**2)/((kappa-2)*(kappa-1))*(kappa*(kappa-1)*t0**2+(2**(3-kappa)-
4)*x_1**(2-kappa)*t0**kappa) )))
```

```
        resmq= resmq + f1* gauss1 * sf.exp(-(x_2/T1)**b1)* sf.exp( -(0.2*(2*pi*Dres1)**2)/((kappa-
2)*(kappa-1))*(t0**2 * kappa* ((2* (kappa-2)* x_2/ t0)- 1.5* (kappa-1)) + 4* x_2** (2-kappa)*
t0**kappa * (1-2**(-kappa)))))
        norm1= norm1 + gauss1
        if i== n :
            firstres= res1
            firstnorm= norm1
            firstresmq = resmq
            res1= 0
            norm1= 0
            resmq= 0


    # DEFINING MODEL FOR FITTING
    funfit = CallableModel({
        y_1: (normalization_factor * firstres/firstnorm) ** (1/root) ,
        y_2: ((firstresmq/firstnorm) +(1-f1)* sf.exp(-(x_2/T2)**b2)) **(1/root),
        })
    # DOING FITTING, FIRST FIND A GOOD GUESS WITH NELDERMEAD METHOD AND
FINALLY FIT WITH BFGS METHOD
    # in BasinHopping method symfit will choose BFGS. When bounds are provided, symfit will switch
to using L-BFGS-B instead.

    fit = Fit(funfit, x_1= xdq1, x_2=xmq, y_1=DQ1, y_2=MQ, minimizer=[NelderMead, BasinHopping])
    fit_result = fit.execute()
    # Y_R IS THE FITTING LINE
    y_r = funfit(x_1=xdq, x_2=xmq, **fit_result.params)
    y_r_complete = funfit(x_1=xmq, x_2=xmq, **fit_result.params)
    dqfit = y_r[0]
    MQfit = y_r_complete[1]
    DQfit = y_r_complete[0]
    for i in range(len(dq)):
        dqfit[i] = (dqfit[i]**root)/normalization_factor
    for i in range (len(xmq)):
        DQfit[i] = (DQfit[i]**root)/normalization_factor
        MQfit[i] = (MQfit[i]**root)
    #measuring residue
    residue_DQ= (dq - dqfit)
    residue_MQ= (mq - MQfit)
    RsquareDQ= 1-(np.sum(residue_DQ**2) / np.sum(((dq-np.mean(dq))**2)))
    RsquareMQ= 1-(np.sum(residue_MQ**2) / np.sum(((mq-np.mean(mq))**2)))
    # PRINT THE RESULTS AND SAVING IT TO A FILE IN OUTADDRESS. 'a' is reffered to
appending the file. it means it add new results to previous ones. if you want to delete previous you
shod use 'w'
    print("last point to fit",boundry+1, '\n', "duplication number", m, '\n', " Best-Fit Parameters: ",
fit_result, '\n', "R^2DQ", RsquareDQ, '\n', "R^2MQ", RsquareMQ)
    f = open(outputadress + "\Weighted-distribution-PWLW-RESULT.txt","a")
    print("last point to fit", boundry+1, '\n', "duplication number", m, '\n', fit_result, '\n', "R^2DQ",
RsquareDQ, '\n', "R^2MQ", RsquareMQ, file=f)
    f.close()
    print("t0", t0)
```

```python
# PLOT THE RESULTS
boundryliney = [0, 1]
boundrylinex = [xmq[boundry], xmq[boundry]]
fig= plt.plot(xmqreal,mqreal, 'k.', x,dqreal,'r.', xmq, DQfit,'c-.', xmq,MQfit,'c-.',boundrylinex,
boundryliney, 'y:' )
# ADD LEGEND TO THE FIGURE
plt.rcParams["legend.fontsize"]= 16
plt.gca().legend(('MQ','DQ', 'AWPL model'))
# DEFINE A LIMIT FOR FIGURE
plt.xlim(0, 40)
plt.ylim(0, 1)
# ADD TITLE AND LABELS TO THE AXIS
plt.ylabel('Intensity', fontsize= 11)
plt.xlabel('DQ-time evolution(ms)', fontsize= 11)
# ADJUST SAVE FIGURE FILE
plt.rcParams["savefig.jpeg_quality"]= 70
plt.savefig(my_path +"/Weighted-PWLW-distribution-figure.png", dpi=600)
plt.clf()
fig2= plt.plot(MQ,residue_MQ, 'r.', DQ, residue_DQ, 'b.')
plt.rcParams["savefig.jpeg_quality"]= 70
plt.savefig(my_path +"/Weighted-PWLW-residual-distribution.png", dpi=600)
plt.clf()
#Generating correlation function
Dres = fit_result.value(Drs1)
kap  = fit_result.value(kappa)
f = fit_result.value(f1)
lnDmed= sf.log(Dres)
sigma= fit_result.value(sigma1)
T_1= fit_result.value(T1)
T_2= fit_result.value(T2)
if RsquareDQ > 0.9 and T_1>0 and T_2>0 and f>0 and sigma>0 and kap>0:
    Dres_ML = Dres
    kap_ML = kap
    f1_ML = f
    sigma_ML = sigma
    T1_ML = T_1
    T2_ML = T_2
    ML= True

L= len(xdq)
correlation_deg1 = np.zeros(L)
correlation_deg2 = np.zeros(L)
correlation_fraction_deg1 = np.zeros(L)
correlation_fraction_deg2 = np.zeros(L)
for j in range (0, L):
    gauss_store = 0
    for i in range(0,n+1):
        lnDtemp= (lnDmed+ ((i-(n/2))*3*sigma/(n/2)))
        Dtemp = sf.exp(lnDtemp)
        gauss = sf.exp(-0.5*((i-(n/2))*3/(n/2))**2)/(sigma* sf.sqrt(2*pi))
```

```
        correlation_deg1[j] = correlation_deg1[j] + gauss * (Dtemp**2)*((xdq[j]/t0)**(-kap))
        correlation_deg2[j] = correlation_deg2[j] + ((gauss * Dtemp)**2)*((xdq[j]/t0)**(-kap))
        correlation_fraction_deg1[j] = correlation_fraction_deg1[j] + f * gauss *
(Dtemp**2)*((xdq[j]/t0)**(-kap))
        correlation_fraction_deg2[j] = correlation_fraction_deg2[j] + ((f * gauss *
Dtemp)**2)*((xdq[j]/t0)**(-kap))
        gauss_store = gauss_store + gauss
    correlation_deg1 [j] = correlation_deg1 [j]/ gauss_store
    correlation_fraction_deg1 [j] = correlation_fraction_deg1 [j]/ gauss_store
    correlation_deg2 [j] = correlation_deg2 [j]/ (gauss_store **2)
    correlation_fraction_deg2 [j] = correlation_fraction_deg2 [j]/ (gauss_store **2)
  g = open(outputadress + "\Wgh-dist-correlation-AWPL-deg1.txt","w")
  for i in range(len(xdq)):
    print(xdq[i],'   ',correlation_deg1[i], file=g),


  g.close()
  g = open(outputadress + "\Wgh-dist-correlation-AWPL-deg2.txt","w")
  for i in range(len(xdq)):
    print(xdq[i],'   ',correlation_deg2[i], file=g),
  g.close()
  g = open(outputadress + "\Wgh-dist-correlation-AWPL-fractiondeg1.txt","w")
  for i in range(len(xdq)):
    print(xdq[i],'   ',correlation_fraction_deg1[i], file=g),
  g.close()
  g = open(outputadress + "\Wgh-dist-correlation-AWPL-fractiondeg2.txt","w")
  for i in range(len(xdq)):
    print(xdq[i],'   ',correlation_fraction_deg2[i], file=g),
  g.close()
  h = open(outputadress + "\plot-AWPL-dist.txt","w")
  for i in range(len(xmqreal)):
    if i!=0:
      print(xmqreal[i],'   ',mqreal[i],'   ', MQfit[i],'   ', dqreal[i], '   ',DQfit[i], file=h)
    else:
      print(xmqreal[i],'   ',mqreal[i],'   ', MQfit[i],'   ', dqreal[i], file=h)
  h.close()
"
```

C. Python code for fitting AWexp model (based on the DTD)

The code fits 9 data sets simultaneously according to the DTD model via TTS (fitting DQ data for PI-comb). The code gets the address of text files (DQ NMR data), automatically finds the text files, and saves all results including text files and jpg files in the same folder.

```
"
import numpy as np
import matplotlib.pyplot as plt
```

```python
from scipy.optimize import curve_fit
import os
from datetime import datetime
def pre(Dres, t0):
    return 0.2*(np.pi**2 * Dres**2)*(t0**2)
def relaxation (x, T):
    return np.exp(-(x/T))
def exp_term_DQ (x_dq, Dres, t0, shift_factor):
    return np.exp(-2* pre (Dres, t0)* (np.exp(-x_dq*shift_factor/t0) +x_dq*shift_factor/t0 -1))
def sinh_term_DQ (x_dq, Dres, t0, shift_factor):
    return np.sinh(pre (Dres, t0)* (np.exp(-2*x_dq*shift_factor/t0)-2*np.exp(-x_dq*shift_factor/t0)+1))
def exp_term_MQ(x_mq, Dres, t0, shift_factor):
    return np.exp(-pre (Dres, t0)* (4* np.exp(-x_mq*shift_factor/t0)- np.exp(-2*x_mq*shift_factor/t0)+
2* x_mq*shift_factor/t0- 3 ))
def inside_exp_term_dq (x_dq, Dres, t0):
    return -2 * pre (Dres, t0)* (np.exp(-x_dq/t0) +x_dq/t0 -1)
def inside_sinh_term_dq (x_dq, Dres, t0):
    return pre (Dres, t0)* (np.exp(-2* x_dq/t0) -2*np.exp(-x_dq/t0)+ 1)
def inside_exp_term_mq (x_mq, Dres, t0):
    return -pre (Dres, t0)* (4* np.exp(-x_mq/t0)- np.exp(-2*x_mq/t0)+ 2* x_mq/t0- 3 )


def residue (dat, fit_dat):
    return (dat - fit_dat)
def R_square (dat, fit_dat):
    return  1-(np.sum(residue(dat, fit_dat)**2) / np.sum(((dat-np.mean(dat))**2)))
def chi_squared (expec_val,comboY):
    return np.sum((comboY-expec_val)**2/abs(expec_val))
def data_preparation() :
    p = 1
    for file in os.listdir(loc):
        if file.endswith(".txt"):
            inputaddress = os.path.join(loc, file)
# The file name is the temperature that data were measured at
            namefile = os.path.join(file)
            namefile = namefile[:-4]
            #addressfile = loc[:] + "\\" + namefile
            temp[p] = int(namefile) #each file should named the associated teperature
            shift_factor[p] = 10**(c1*temp[p]/(c2 + temp[p])) #rheological shift factor based on WLF
            # READING THE TEXT FILE AND COPY IT TO DATA
            data1 = np.loadtxt(inputaddress)
            #data1 = data1[data1.min(axis=1)>=0,:]
            num_rows, num_cols = data1.shape
            maxim = np.where(data1[:,2] == np.amax(data1[:,2]))
            #print (num_rows, num_cols)
            boundry[p] = int(maxim[0]) + 0
            length_MQ[p] = num_rows
            data[p,0:num_rows,0] = np.round(data1[:,0],4)
            data[p,0:num_rows,1] = (data1[:,1] + data1[:,2])/(data1[0,1] + data1[0,2])
            data[p,0:num_rows,2] = data1[:,2]/(data1[0,1] + data1[0,2])
            p=p+1
    return p-1
def print_result(fittedParameters,R2_DQ,  R2_MQ, chi_2, outputadress):
```

```
    f = open(outputadress + "\Awexp-RESULT-prediction.txt","a")
    print("#----------------------------------------------------------------------------", file = f)
    print("#fitting at", start_time, file= f)
    print("#alpha_NMR = ", alpha_NMR," ", "#root =", root, file= f)
    print("Dres= ", round(fittedParameters[0],3), '\n', "M_e= ", round(fittedParameters[1],3), '\n',
"tau_e= ", round(fittedParameters[2],5), '\n', file= f)
    #print("fi_bb ", round(fittedParameters[2]/(fittedParameters[2]+
fittedParameters[3]*fittedParameters[1]),3), '\n', "fi_a ",
round(fittedParameters[3]*fittedParameters[1]/(fittedParameters[2]+
fittedParameters[3]*fittedParameters[1]),3), '\n', file= f)
    for i in range (1, n+1):
        print("f1_", str(i), "=", round(f1[i], 2),'\n', file=f)
        print("T1_", str(i), "=", round(fittedParameters[2+i],1), "      ", "T2_", str(i), "=",
round(fittedParameters[9+i],1),'\n', file=f)
        #print("T2_", str(i), "=", round(fittedParameters[10+i],1),'\n', file=f)

    #print("Tmed_1: ", fittedParameters[3], '\n', "Tmed_2: ", fittedParameters[4], '\n', "Tmed_3: ",
fittedParameters[5], '\n', file= f)
    #print("sigma1: ", fittedParameters[6], '\n', "sigma2: ", fittedParameters[7], '\n', "sigma3: ",
fittedParameters[8], '\n', file= f)
    for i in range (1, n+1):
        print ("R2_DQ_" +str(i)+ "_"+ str(temp[i]) +"C=", round(R2_DQ[i],5), '\t', "R2_MQ_" +str(i) + "_"+
str(temp[i]) +"C=", round(R2_MQ[i],5), '\t', "chi-squared_" +str(i) + "_"+ str(temp[i]) +"C=",
round(chi_2[i],6), file=f)
    f.close()
def plot_result ( yy, outputadress):
    pointer = 0
    for i in range(1,n+1):
        boundryliney = [0, 1]
        boundrylinex = [data[i,boundry[i],0], data[i,boundry[i],0]]
        plt.plot(data[i,0:length_MQ[i],0],data[i,0:length_MQ[i],1], 'k.',
data[i,1:length_MQ[i],0],data[i,1:length_MQ[i],2],'r.', data[i,1:length_MQ[i],0],
yy[pointer:pointer+length_MQ[i]-1],'c-.', data[i,1:length_MQ[i],0],yy[pointer+length_MQ[i]-1:pointer+
2*(length_MQ[i]-1)],'c-.',boundrylinex, boundryliney, 'y:')
        pointer = pointer + 2*(length_MQ[i]-1)
        plt.rcParams["legend.fontsize"]= 10
        plt.gca().legend(('MQ','DQ', 'simultaneous fitting-DTD theory'))
        plt.ylim(0.001, 1)
        plt.ylabel('Intensity', fontsize= 8)
        plt.xlabel('DQ-time evolution(ms)', fontsize= 8)
        plt.yscale('log')
        # ADJUST SAVE FIGURE FILE
        #plt.rcParams["savefig.jpeg_quality"]= 70
        plt.savefig(outputadress +"/" + str(temp[i]) + "C-AW-arm-retraction.png", dpi=600)
        #plt.show()
        plt.clf()
def combine_data (data_c, s):
    if s == 0 :
        return np.array([]), np.array([])
    else:
```

```python
        return np.concatenate((combine_data (data_c, s-1)[0] ,data_c[s,1:boundry[s],0],
data_c[s,1:length_MQ[s],0])), np.concatenate((combine_data (data_c, s-1)[1] ,data_c[s,1:boundry[s],2],
data_c[s,1:length_MQ[s],1]))
def U_bb_xb(x_b):
    return (1-((1-x_b)**(alpha+1) * (1+(1+alpha)*x_b)))
def diff_1_Ub (x_b, fi_bb, s_b):
    c = 15 *(-((1 + alpha)* (1 - x_b)**(1 + alpha)) + (1 + alpha)* (1 - x_b)**alpha *(1 + (1 + alpha)* x_b))
* fi_bb**alpha * s_b / (8* (1 + alpha)* (2 + alpha))
    return c
def diff_2_Ub(x_b, fi_bb, s_b):
    c = 15 *(2 *(1 + alpha)**2 *(1 - x_b)**alpha - alpha* (1 + alpha)* (1 - x_b)**(-1 + alpha) *(1 + (1 +
alpha)* x_b))* fi_bb**alpha * s_b
    return c
def rett_bb(x_b, tau_a_long, p, q, s_b, fi_bb):
    #fi_bb = fi_b #* (1- (2/(q+1)))
    #tau_b early in case of lightly branched combs
    #tau_bb_early = 25/64 *(1/(p**2)) * f * s_b**2 * x_b**2 *tau_a_long * fi_bb**(2*alpha)
    tau_bb_early = 375/8192 *(np.pi/(p**2)) * q * s_b**3 * x_b**4 *tau_a_long * fi_bb**(3*alpha)
    U_b = (15*s_b*(fi_bb**alpha)/(8*(1+alpha)*(2+alpha))) * U_bb_xb(x_b)
    tau_bb_late = 25 * s_b**2 * fi_bb**(2*alpha) * q * tau_a_long * np.exp(U_b)*
((2*np.pi/(diff_2_Ub(0, fi_bb, s_b)))**0.5)/(8*p**2 * diff_1_Ub (x_b, fi_bb, s_b))
    return (tau_bb_early * np.exp(U_b))/(1+(tau_bb_early * np.exp(U_b)/tau_bb_late))


def integral_fit (comboX, *par):
    #Par[i], 0=Dres,1=Me, 2=tau_e, 3=T1, 4=T2,5=T2, 6=T2 7=T3 ,8=T4, 9=T5, 10= T6, 9=T7, 10 =
T2_1, 11= T2_2
    s_a = np.zeros(n_tau+1)
    x_bb = np.zeros(n_tau+1)
    for i in range (1, n_tau+1):
        s_a[i] = i/n_tau
        x_bb[i] = i/n_tau
    fit_sum = np.array([])
#par[] are the fitting parameters
    Me = par[1]
    tau_e = par[2]
    Z_a = M_a/Me
    Z_bb = M_bb/Me# * (1-(2/(q+1)))
    fi_b = M_bb/(M_bb + q*M_a)
    fi_a = 1-fi_b
    fi_bb = fi_b
    U_a = (15/4)* Z_a* ((1-((1-fi_a*s_a)**(alpha+1))*(1+(1+alpha)*fi_a*s_a)))/(fi_a**2 * (alpha+1) *
(alpha+2))
    tau_early = (225/256)*(np.pi**3) * tau_e* (Z_a* s_a)**4
    tau_late = (np.pi**5 *( 2/15))**0.5 * tau_e * Z_a**1.5* np.exp(U_a)/(s_a * (1-(fi_a*s_a))**alpha)
    tau_a = (tau_early * np.exp(U_a))/(1+(tau_early*np.exp(U_a)/tau_late))
    tau_a_longest = tau_a[n_tau]
    tau_clf_bb = rett_bb(x_bb, tau_a_longest, p , q, Z_bb, fi_bb)
    tau_rept_bb = (25/(8*np.pi**2 * p**2)) * (1-x_bb)**2 * Z_bb **2 * fi_bb**(2*alpha) * tau_a_longest
* q
    for i in range (1,n+1):
        x_mq = data[i,1:length_MQ[i],0]
        fit_DQ = np.zeros(len(x_mq))
```

```
        fit_MQ = np.zeros(len(x_mq))
        fit_DQ_arm = np.zeros(len(x_mq))
        fit_MQ_arm = np.zeros(len(x_mq))
        fit_DQ_bb = np.zeros(len(x_mq))
        fit_MQ_bb = np.zeros(len(x_mq))
        fit_DQ_rep = np.zeros(len(x_mq))
        fit_MQ_rep = np.zeros(len(x_mq))
        x_c = 1
        border_bb = 0
        ret_rep = True
        tau_arm = tau_a/shift_factor[i]
        j=1
        while tau_arm[j] *3 < x_mq[0]:
            j+=1
        border_arm = j-1
        tau_s = tau_clf_bb /shift_factor[i]
        tau_rept = tau_rept_bb /shift_factor[i]
        tt = 1
        while tau_s[tt] < tau_rept[tt]:
            if tau_s[tt] * 3 < x_mq[0]:
                border_bb = tt
            tt+=1
        x_c = (tt-1)/n_tau
        tail = fi_a* ((border_arm/n_tau)) + (tail_bb)+ fi_bb* (border_bb/n_tau)
        for j in range (1,n_tau+1):
            if tau_arm[j] *3 > x_mq[0]:
                fit_DQ_arm = fit_DQ_arm +  (exp_term_DQ(x_mq, par[0] * ((1-fi_a*s_a[j]))** alpha_NMR,
tau_arm[j], 1) * sinh_term_DQ(x_mq, par[0]* ((1-fi_a*s_a[j]))** alpha_NMR, tau_arm[j], 1))/(n_tau)
                fit_MQ_arm = fit_MQ_arm + (exp_term_MQ(x_mq, par[0]* ((1-fi_a*s_a[j]))** alpha_NMR,
tau_arm[j], 1))/(n_tau)
            if j/n_tau < x_c:
                if tau_s[j] * 3 > x_mq[0]:
                    fit_DQ_bb = fit_DQ_bb + (exp_term_DQ(x_mq, par[0] *(fi_bb * (1-x_bb[j]))**alpha_NMR,
tau_s[j], 1) * sinh_term_DQ(x_mq, par[0] *(fi_bb * (1-x_bb[j]))**alpha_NMR, tau_s[j], 1))/(n_tau)
                    fit_MQ_bb = fit_MQ_bb + (exp_term_MQ(x_mq, par[0] *(fi_bb * (1-
x_bb[j]))**alpha_NMR, tau_s[j], 1))/(n_tau)

        tau_rep = tau_rept[tt]
        inside_expterm_dq = np.zeros(len(x_mq))
        inside_sinhterm_dq = np.zeros(len(x_mq))
        inside_expterm_mq = np.zeros(len(x_mq))
        for tt in range(10):
            pp = 2*tt +1
            inside_expterm_dq = inside_expterm_dq + (8/(np.pi**2 * (pp)**2)) *
inside_exp_term_dq(x_mq, par[0]* (fi_bb * (1-x_c ))**alpha_NMR, tau_rep/(pp**2))
            inside_sinhterm_dq = inside_sinhterm_dq + (8/(np.pi**2 * (pp)**2))*
inside_sinh_term_dq(x_mq, par[0]* (fi_bb * (1-x_c ))**alpha_NMR, tau_rep/(pp**2))
            inside_expterm_mq = inside_expterm_mq + (8/(np.pi**2 * (pp)**2))*
inside_exp_term_mq(x_mq, par[0]* (fi_bb * (1-x_c ))**alpha_NMR, tau_rep/(pp**2))

        fit_MQ_rep = np.exp(inside_expterm_mq)
        fit_DQ_rep = np.exp(inside_expterm_dq)* np.sinh(inside_sinhterm_dq)
```

```python
    #tail = fi_a* ((border_arm/n_tau)) + (tail_bb)+ fi_bb* (border_bb/n_tau)
    f1[i] = 1-tail
    fit_DQ = (fit_DQ_arm * fi_a + fi_bb* (fit_DQ_bb + (1-x_c)* fit_DQ_rep))* relaxation(x_mq,
par[2+i]) #* f1[i]
    fit_MQ = (fit_MQ_arm * fi_a + fi_bb* (fit_MQ_bb + (1-x_c)* fit_MQ_rep)) * relaxation(x_mq,
par[2+i])  + (1-f1[i])* relaxation(x_mq, par[2+n+i]) # n is the number of data
    fit_sum = np.concatenate((fit_sum, fit_DQ[0:boundry[i]-1], fit_MQ))
  return fit_sum**(1/root)
def integral_fit_compelete (x_m, *par):
  #Par[i], 0=Dres,1=kappa,2=tau_d_0 3=f1,4=T1, 5=T2 6=T3 ,7=T4, 8=T5, 9= T6, 10=T7, 11 = T2_1,
12= T2_2
  s_a = np.zeros(n_tau+1)
  x_bb = np.zeros(n_tau+1)
  for i in range (1, n_tau+1):
    s_a[i] = i/n_tau
    x_bb[i] = i/n_tau
  fit_sum = np.array([])
  Me = par[1]
  tau_e = par[2]
  Z_a = M_a/Me
  Z_bb = M_bb/Me# * (1-(2/(q+1)))

  fi_b = M_bb/(M_bb + q*M_a)
  fi_a = 1-fi_b
  fi_bb = fi_b# * (1- (2/(q+1)))
  tail_bb = 0#fi_b * (2/(q+1))
  U_a = (15/4)* Z_a* ((1-((1-fi_a*s_a)**(alpha+1))*(1+(1+alpha)*fi_a*s_a)))/(fi_a**2 * (alpha+1) *
(alpha+2))
  tau_early = (225/256)*(np.pi**3) * tau_e* (Z_a* s_a)**4
  tau_late = (np.pi**5 *( 2/15))**0.5 * tau_e * Z_a**1.5* np.exp(U_a)/(s_a * (1-(fi_a*s_a))**alpha)
  tau_a = (tau_early * np.exp(U_a))/(1+(tau_early*np.exp(U_a)/tau_late))
  tau_a_longest = tau_a[n_tau]
  tau_clf_bb = rett_bb(x_bb, tau_a_longest, p , q, Z_bb, fi_bb)
  tau_reptation = (25/(8*np.pi**2 * p**2)) * (1-x_bb)**2 * Z_bb **2 * fi_bb**(2*alpha) *
tau_a_longest * q
  for i in range (1,n+1):
    x_mq = data[i,1:length_MQ[i],0]
    fit_DQ = np.zeros(len(x_mq))
    fit_MQ = np.zeros(len(x_mq))
    fit_DQ_arm = np.zeros(len(x_mq))
    fit_MQ_arm = np.zeros(len(x_mq))
    fit_DQ_bb = np.zeros(len(x_mq))
    fit_MQ_bb = np.zeros(len(x_mq))
    fit_DQ_rep = np.zeros(len(x_mq))
    fit_MQ_rep = np.zeros(len(x_mq))
    x_c = 1
    border_bb = 0
    ret_rep = True
    tau_arm = tau_a/shift_factor[i]
    j=1
    while tau_arm[j] *3 < x_mq[0]:
      j+=1
```

```
    border_arm = j-1
    tau_s = tau_clf_bb /shift_factor[i]
    tau_rept = tau_reptation /shift_factor[i]
    tt = 1
    while tau_s[tt] < tau_rept[tt]:
       if tau_s[tt] * 3 < x_mq[0]:
          border_bb = tt
       tt+=1
    x_c = (tt-1)/n_tau
    rep_treshold = tt
    tail = fi_a* ((border_arm/n_tau)) + (tail_bb)+ fi_bb* (border_bb/n_tau)
    for j in range (1,n_tau+1):
       if tau_arm[j] *3 > x_mq[0]:
          fit_DQ_arm = fit_DQ_arm +  (exp_term_DQ(x_mq, par[0] * ((1-fi_a*s_a[j]))** alpha_NMR,
tau_arm[j], 1) * sinh_term_DQ(x_mq, par[0]* ((1-fi_a*s_a[j]))** alpha_NMR, tau_arm[j], 1))/(n_tau)
          fit_MQ_arm = fit_MQ_arm + (exp_term_MQ(x_mq, par[0]* ((1-fi_a*s_a[j]))** alpha_NMR,
tau_arm[j], 1))/(n_tau)
       if j/n_tau < x_c:
          if tau_s[j] * 3 > x_mq[0]:
             fit_DQ_bb = fit_DQ_bb + (exp_term_DQ(x_mq, par[0] *(fi_bb * (1-x_bb[j]))**alpha_NMR,
tau_s[j], 1) * sinh_term_DQ(x_mq, par[0] *(fi_bb * (1-x_bb[j]))**alpha_NMR, tau_s[j], 1))/(n_tau)
             fit_MQ_bb = fit_MQ_bb + (exp_term_MQ(x_mq, par[0] *(fi_bb * (1-
x_bb[j]))**alpha_NMR, tau_s[j], 1))/(n_tau)

    tau_rep = tau_rept[tt]
    inside_expterm_dq = np.zeros(len(x_mq))
    inside_sinhterm_dq = np.zeros(len(x_mq))
    inside_expterm_mq = np.zeros(len(x_mq))
    for tt in range(10):
       pp = 2*tt +1
       inside_expterm_dq = inside_expterm_dq + (8/(np.pi**2 * (pp)**2)) *
inside_exp_term_dq(x_mq, par[0]* (fi_bb * (1-x_c ))**alpha_NMR, tau_rep/(pp**2))
       inside_sinhterm_dq = inside_sinhterm_dq + (8/(np.pi**2 * (pp)**2))*
inside_sinh_term_dq(x_mq, par[0]* (fi_bb * (1-x_c ))**alpha_NMR, tau_rep/(pp**2))
       inside_expterm_mq = inside_expterm_mq + (8/(np.pi**2 * (pp)**2))*
inside_exp_term_mq(x_mq, par[0]* (fi_bb * (1-x_c ))**alpha_NMR, tau_rep/(pp**2))

    fit_MQ_rep = np.exp(inside_expterm_mq)
    fit_DQ_rep = np.exp(inside_expterm_dq)* np.sinh(inside_sinhterm_dq)
    #tail = fi_a* ((border_arm/n_tau)) + (tail_bb)+ fi_bb* (border_bb/n_tau)
    f1[i] = 1-tail
    fit_DQ = (fit_DQ_arm * fi_a + fi_bb* (fit_DQ_bb + (1-x_c)* fit_DQ_rep))* relaxation(x_mq,
par[2+i]) #* f1[i]
    fit_MQ = (fit_MQ_arm * fi_a + fi_bb* (fit_MQ_bb + (1-x_c)* fit_MQ_rep)) * relaxation(x_mq,
par[2+i])  + (1-f1[i])* relaxation(x_mq, par[2+n+i])
    fit_sum = np.concatenate((fit_sum, fit_DQ, fit_MQ))

    fit_DQ_arm_report = (fit_DQ_arm * fi_a )* relaxation(x_mq, par[2+i])
    fit_DQ_bb_report = fi_bb* (fit_DQ_bb + (1-x_c)* fit_DQ_rep)* relaxation(x_mq, par[2+i])
    f = open(outputadress + "\\" + str(temp[i])+ "C-fitdata.txt","w")
    g = open(outputadress + "\\" + str(temp[i])+ "C-fit-arm and backbone contribution(first am-
secon bb).txt","w")
```

```
    for j in range (1 ,length_MQ[i]):
        print(x_mq[j-1],'   ',data[i,j,1],'   ', data[i,j,2],'   ', fit_MQ[j-1],'   ', fit_DQ[j-1],'   ',
data[i,boundry[i],0], file=f)
        print(x_mq[j-1],'   ', fit_DQ_arm_report [j-1] ,'   ',fit_DQ_bb_report [j-1], file=g)
    f.close()
    g.close()
  tau_a = tau_a / 1000
  tau_clf_bb = tau_clf_bb /1000
  tau_reptation = tau_reptation /1000
  h = open(outputadress + "\\relaxation spectrum at 0C-arm-CLFbb-reptation.txt","w")
  for j in range (1,n_tau+1):
    print(j,'   ', tau_a [j] ,'   ',tau_clf_bb[j],'   ',tau_reptation[j], file=h)
  h.close()
  time_correlation = np.logspace (-8, 4, 60)
  #fi_unrelaxed = v_frac_unrelaxed_segment(time_correlation , tau_reptation[rep_treshold], x_c,
fi_a, fi_bb, rep_treshold)
  corr_address_arm = outputadress + "\\correlation functions_arm"
  corr_address_bb = outputadress + "\\correlation functions_bb"
  corr_fun_bb_rept = np.zeros (len(time_correlation))
  if not os.path.exists(corr_address_arm):
    os.makedirs(corr_address_arm)
  if not os.path.exists(corr_address_bb):
    os.makedirs(corr_address_bb)
  for j in range(1, n_tau+1):
    x= j/n_tau
    corr_fun_arm = ((1-fi_a*x))** (2*alpha_NMR) * np.exp(-time_correlation/tau_a[j])
    f = open(corr_address_arm + "\\arm_Seg_No_" + str(j)+ ".txt","w")
    for cc in range (len(time_correlation)):
      print(time_correlation[cc], '   ',corr_fun_arm[cc], file=f)
    if j <= rep_treshold:
      if j < rep_treshold:
        g = open(corr_address_bb + "\\clf_bb_Seg_No_" + str(j)+ ".txt","w")
        corr_fun_bb_clf = (fi_bb*(1-x))** (2*alpha_NMR) * np.exp(-time_correlation/tau_clf_bb[j])
        for t in range(len(time_correlation)):
          print(time_correlation[t], '   ',corr_fun_bb_clf[t], file=g)

      else:
        g = open(corr_address_bb + "\\rept_bb_Seg_No_" + str(j)+ ".txt","w")
        for tt in range(count_rep):
          pp = 2*tt+1
          corr_fun_bb_rept = corr_fun_bb_rept + (fi_bb*(1-x))** (2*alpha_NMR) * (8/(np.pi**2 *
(pp)**2))* np.exp(-time_correlation/(tau_reptation[rep_treshold]/(pp)**2))
        for t in range(len(time_correlation)):
          print(time_correlation[t], '   ',corr_fun_bb_rept[t], file=g)
      g.close()
    f.close()
  init_range = x_mq[0]* shift_factor[1]/1000
  upper_range = x_mq[len(x_mq)-1] * shift_factor [n]/1000
  f = open(outputadress + "\\NMR-covered range.txt","w")
  print("initial range=", init_range, file=f)
  print("end range=", upper_range, file=f)
```

```python
    f.close()
    return fit_sum
def fitting_scipy(comboX, comboY,initialParameters, outputadress):
    #initialParameters = np.array([0.1, 2, 0.2])
    bnd= [[0.00001, 68, 0.00001, 0.01, 0.01, 0.01, 0.01, 0.01, 0.01, 0.01, 0.01, 0.01, 0.01, 0.01, 0.01, 0.01,
0.01],[2, 9000, 2000, "inf", "inf", "inf", "inf", "inf", "inf", "inf", "inf", "inf", "inf", "inf", "inf", "inf", "inf" ]]
    # curve fit the combined data to the combined function
    fittedParameters, pcov = curve_fit(integral_fit, comboX, comboY, initialParameters, bounds= bnd)
    standard_dev = np.sqrt(np.diag(pcov)) # compute one standard deviation errors on the parameters
    return fittedParameters
def AWEXP_fit ():
    global outputadress
    outputadress = loc + "\hierarchical-sb-modified-by-Mcleisch"
    if not os.path.exists(outputadress):
        os.makedirs(outputadress)
    # ASSIGN DIRECTORY FOR SAVING THE FIGURE
    combo = combine_data (data,n)
    comboX = combo[0]
    comboY = combo[1]
    initial_par= np.array([0.24, 4500, 0.15, 4 , 5 ,7 , 9, 9 , 10, 11, 15, 25, 35, 45, 45, 45, 50])
    #T2_i = np.array([21, 88, 5, 14, 6.6, 23, 8.5, 32, 12, 34, 16, 35, 15, 54, 17, 70])
    #initial_par = np.append(initial_par, T2_i)
    results = fitting_scipy(comboX, abs(comboY) **(1/root), initial_par, outputadress)
    y_r =(integral_fit(comboX, *results) )**root
    R2_DQ = np.zeros(n+1)
    R2_MQ = np.zeros(n+1)
    chi_2 = np.zeros(n+1)
    pointer = 0
    for i in range (1,n+1):
        R2_DQ[i] = R_square ((comboY[pointer:pointer + boundry[i]-1]), y_r[pointer: pointer +
boundry[i]-1])
        R2_MQ[i] = R_square ((comboY[pointer + boundry[i]-1:pointer + boundry[i]-1 + length_MQ[i]-1]),
y_r[pointer + boundry[i]-1:pointer + boundry[i]-1 + length_MQ[i]-1])
        chi_2[i] = chi_squared (y_r[pointer: pointer + boundry[i]-1 + length_MQ[i]-1],comboY[pointer:
pointer + boundry[i]-1 + length_MQ[i]-1])
        pointer = pointer + boundry[i]-1 + length_MQ[i]-1


    print_result(results,R2_DQ,  R2_MQ, chi_2, outputadress)
    #comboX_compelete = time
    y_r_compelete =(integral_fit_compelete(data[1,1:length_MQ[1], 0], *results) )
    plot_result (y_r_compelete, outputadress)
    # PRINT THE RESULTS AND SAVING IT TO A FILE IN OUTADDRESS. 'a' is reffered to
appending the file. it means it add new results to previous ones. if you want to delete previous you
shod use 'w'
    # build the correlation function

    #plt.plot(correlation[:,0], correlation[:,1] , 'k.')
    #plt.xscale('log')
    #plt.yscale('log')
    #plt.savefig(outputadress +"/streched-exp-correlation.png", dpi=600)

    #plt.clf()
```

```
    #return correlation
start_time = datetime.now()
M_0 = 68.1
M_a = 13800
M_bb = 68800
N_a = int(round(M_a / M_0,0))
N_bb = int(round(M_bb / M_0,0))
fi_a = 0.633
fi_b = 1 - fi_a
alpha = 4/3
alpha_NMR = 4/3
p = (12)**-0.5
q = 8.5
count_rep = 10 # number mods for determining reptation motion
n_tau = 100  #number of segments in backbone or side chain
root = 2 # all data fitted in the squared-root form
c1 = 6.14015 #WLF constant
c2 = 114.791 #WLF constant
temp = np.zeros(10)
files = 10 # maximum number of text file in the folder
shift_factor = np.zeros(10)
data_real = np.zeros(shape = (files,100,3))
data = np.zeros(shape = (files,100,3))
boundry =  np.zeros(10, dtype= int)
length_MQ =  np.zeros(10, dtype=int)
loc = input("please give me the address of the folder which contains your data")
n = data_preparation()
f1 = np.zeros(n+1)
time = data[1,0:length_MQ[1],0]
AWEXP_fit ()
end_time = datetime.now()
print('Duration: {}'.format(end_time - start_time))
"
```

For fitting the data with the time-dependent fraction of unrelaxed segments (Dres~Ne^-0.5), just two functions are changed in the previous code:

```
"
def fi_timedependent_calculator (x_mq, Dres, t0, tau_arm, tau_bb, tau_rep, x_c, fi_a, fi_bb):
    DQ_exp_term= np.zeros(len(x_mq))
    DQ_sinh_term= np.zeros(len(x_mq))
    MQ_exp_term= np.zeros(len(x_mq))
    zeta_arm = np.zeros(n_tau)
    zeta_bb = np.zeros(n_tau)
    for i in range(1,n_tau+1):
        x_ab = i/n_tau
        zeta_arm = (t0* tau_arm[i])/(t0+ tau_arm[i])
        zeta_bb = (t0* tau_bb[i])/(t0+ tau_bb[i])
        DQ_exp_term= DQ_exp_term + fi_a* inside_exp_term_dq (x_mq, Dres, zeta_arm)/n_tau
        DQ_sinh_term= DQ_sinh_term + fi_a* inside_sinh_term_dq (x_mq, Dres, zeta_arm)/n_tau
        MQ_exp_term= MQ_exp_term + fi_a* inside_exp_term_mq (x_mq, Dres, zeta_arm)/n_tau
```

```python
    if x_ab <= x_c:
        DQ_exp_term= DQ_exp_term + fi_bb* inside_exp_term_dq (x_mq, Dres, zeta_bb)/n_tau
        DQ_sinh_term= DQ_sinh_term + fi_bb* inside_sinh_term_dq (x_mq, Dres, zeta_bb)/n_tau
        MQ_exp_term= MQ_exp_term + fi_bb* inside_exp_term_mq (x_mq, Dres, zeta_bb)/n_tau
    zeta_rep = t0
    DQ_exp_term= DQ_exp_term + fi_bb * (1-x_c)* inside_exp_term_dq(x_mq, Dres, zeta_rep)
    DQ_sinh_term= DQ_sinh_term + fi_bb * (1-x_c)* inside_sinh_term_dq(x_mq, Dres, zeta_rep)
    MQ_exp_term= MQ_exp_term + fi_bb * (1-x_c)* inside_exp_term_mq(x_mq, Dres, zeta_rep)

    return DQ_exp_term, DQ_sinh_term, MQ_exp_term
def integral_fit (comboX, *par):
    #Par[i], 0=Dres,1=Me, 2=taue, 3=q, 4=T1,5=T2, 6=T2 7=T3 ,8=T4, 9=T5, 10= T6, 9=T7, 10 = T2_1,
11= T2_2
    #x_dq = comboX[:boundry] # first data
    #x_mq = time[1:length_MQ[1]] # second data
    s_a = np.zeros(n_tau+1)
    x_bb = np.zeros(n_tau+1)
    for i in range (1, n_tau+1):
        s_a[i] = i/n_tau
        x_bb[i] = i/n_tau
    fit_sum = np.array([])
    Me = par[1]
    tau_e = par[2]
    #q = par[3]
    Z_a = M_a/Me
    Z_bb = M_bb/Me * (1-(2/(q+1)))
    #p = (12)**-0.5
    fi_b = M_bb/(M_bb + q*M_a)
    fi_a_real = 1-fi_b
    fi_bb = fi_b# * (1- (2/(q+1)))
    fi_a = 1-fi_bb
    tail_bb = 0 #fi_b * (2/(q+1))
    U_a = (15/4)* Z_a* ((1-((1-fi_a*s_a)**(alpha+1))*(1+(1+alpha)*fi_a*s_a)))/(fi_a**2 * (alpha+1) *
(alpha+2))
    tau_early = (225/256)*(np.pi**3) * tau_e* (Z_a* s_a)**4
    tau_late = (np.pi**5 *( 2/15))**0.5 * tau_e * Z_a**1.5* np.exp(U_a)/(s_a * (1-(fi_a*s_a))**alpha)
    tau_a = (tau_early * np.exp(U_a))/(1+(tau_early*np.exp(U_a)/tau_late))
    tau_a_longest = tau_a[n_tau]
    tau_clf_bb = rett_bb(x_bb, tau_a_longest, p , q, Z_bb, fi_bb)
    tau_reptation = (25/(8*np.pi**2 * p**2)) * (1-x_bb)**2 * Z_bb **2 * fi_bb**(2*alpha) *
tau_a_longest * q

    for i in range (1,n+1):
        x_mq = data[i,1:length_MQ[i],0]
        fit_DQ = np.zeros(len(x_mq))
        fit_MQ = np.zeros(len(x_mq))
        fit_DQ_arm = np.zeros(len(x_mq))
        fit_MQ_arm = np.zeros(len(x_mq))
        fit_DQ_bb = np.zeros(len(x_mq))
        fit_MQ_bb = np.zeros(len(x_mq))
        fit_DQ_rep = np.zeros(len(x_mq))
        fit_MQ_rep = np.zeros(len(x_mq))
```

```
    #x_c = 1
    border_bb = 0
    #ret_rep = True
    tau_arm = tau_a/shift_factor[i]
    tau_s = tau_clf_bb/ shift_factor[i]
    tau_rept = tau_reptation/ shift_factor[i]
    j=1
    ss = True
    while tau_arm[j] *tail_factor < x_mq[0] and ss:
       j+=1
       if j>n_tau:
          ss= False
          j-=1
    border_arm = j-1

    tt = 1
    while tau_s[tt] < tau_rept[tt]:
       if tau_s[tt] * tail_factor < x_mq[0]:
          border_bb = tt
       tt+=1
    x_c = (tt-1)/n_tau
    tail = fi_a_real* ((border_arm/n_tau)) + (tail_bb)+ fi_bb* (border_bb/n_tau)
    tau_rep = tau_rept[tt]
    for j in range (1,n_tau+1):
       if tau_arm[j] *tail_factor > x_mq[0]:
          inside_signalterms= fi_timedependent_calculator(x_mq, par[0], tau_arm[j], tau_arm, tau_s,
tau_rep, x_c, fi_a, fi_bb)
          fit_DQ_arm = fit_DQ_arm + np.exp(inside_signalterms[0]) *
np.sinh(inside_signalterms[1])/(n_tau)
          fit_MQ_arm = fit_MQ_arm + np.exp(inside_signalterms[2])/(n_tau)
       if j < tt:
          if tau_s[j] * tail_factor > x_mq[0]:
             inside_signalterms= fi_timedependent_calculator(x_mq, par[0], tau_s[j], tau_arm, tau_s,
tau_rep, x_c, fi_a, fi_bb)
             fit_DQ_bb = fit_DQ_bb + np.exp(inside_signalterms[0]) *
np.sinh(inside_signalterms[1])/(n_tau)
             fit_MQ_bb = fit_MQ_bb + np.exp(inside_signalterms[2])/(n_tau)

    inside_expterm_dq = np.zeros(len(x_mq))
    inside_sinhterm_dq = np.zeros(len(x_mq))
    inside_expterm_mq = np.zeros(len(x_mq))
    for tt in range(count_rep):
       pp = 2*tt +1
       inside_signalterms= fi_timedependent_calculator(x_mq, par[0], tau_rep/(pp**2), tau_arm,
tau_s, tau_rep, x_c, fi_a, fi_bb)
       inside_expterm_dq = inside_expterm_dq +  (8/(np.pi**2 * (pp)**2))* inside_signalterms[0]
       inside_sinhterm_dq = inside_sinhterm_dq + (8/(np.pi**2 * (pp)**2))* inside_signalterms[1]
       inside_expterm_mq = inside_expterm_mq + (8/(np.pi**2 * (pp)**2))* inside_signalterms[2]

    fit_MQ_rep = np.exp(inside_expterm_mq)
    fit_DQ_rep = np.exp(inside_expterm_dq)* np.sinh(inside_sinhterm_dq)
    #tail = fi_a* ((border_arm/n_tau)) + (tail_bb)+ fi_bb* (border_bb/n_tau)
```

```
    f1[i] = 1-tail
    fit_DQ = (fit_DQ_arm * fi_a_real + fi_bb* (fit_DQ_bb + (1-x_c)* fit_DQ_rep))* relaxation(x_mq,
par[2+i]) #* f1[i]
    fit_MQ = (fit_MQ_arm * fi_a_real + fi_bb* (fit_MQ_bb + (1-x_c)* fit_MQ_rep)) * relaxation(x_mq,
par[2+i])  + (1-f1[i])* relaxation(x_mq, par[2+n+i])

    fit_sum = np.concatenate((fit_sum, fit_DQ[0:boundry[i]-1], fit_MQ))
    return fit_sum**(1/root)
"
```

It is noted that the *"integral_fit_complete"* function should be written similarly to the *"integral_fit"* function. In the case of $D_{res} \sim N_e^{-1}$, numerical integration is applied for fitting the data. The functions being needed to be changed, are written in the following.

```
"
def frac_unrelaxed_segment(t, tau_rep, x_c, fi_a, fi_bb):
  #print(tau_arm)
  unrelaxed_fraction = fi_a * relaxed_segments_counter (t, tau_arm[1:])/n_tau +
fi_bb*(relaxed_segments_counter (t, tau_s[1:rep_treshold])/n_tau + (1-x_c))#* rep_tube_survival(t,
tau_rep))
  return unrelaxed_fraction
def frac_unrelaxed_segment_final(t, tau_rep, x_c, fi_a, fi_bb, rep_treshold):
  #print(tau_arm)
  unrelaxed_fraction = fi_a * relaxed_segments_counter (t, tau_a[1:])/n_tau +
fi_bb*(relaxed_segments_counter (t, tau_clf_bb[1:rep_treshold])/n_tau + (1-x_c))#*
rep_tube_survival(t, tau_rep))
  return unrelaxed_fraction
def relaxed_segments_counter (t, tau):
  #count= np.zeros(len(tau))
  count = np.exp(-t/tau)
  return sum(count)
def rep_tube_survival(t, tau_rep):
  tube_survival = 0
  for i in range(count_rep):
    pp= 2*i+1
    tube_survival = tube_survival + (8/(np.pi**2 * (pp)**2))* relaxation (t, tau_rep/(pp**2))
  return tube_survival

def integration(x_mq, Dres, tau_d, tau_rep, x_c, fi_a, fi_bb):
  integrand_fi_1 = lambda t: frac_unrelaxed_segment(t, tau_rep, x_c, fi_a, fi_bb)**NMR_alpha * 0.2*
(np.pi**2)* (Dres**2 * np.exp(-t/tau_d))
  integrand_fi_2 = lambda t: frac_unrelaxed_segment(t, tau_rep, x_c, fi_a, fi_bb)**NMR_alpha * t*
0.2* (np.pi**2)* (Dres**2 * np.exp(-t/tau_d))
  #integrand_fi1_2 = lambda t: (x_mq-t)* 0.2* 2* (np.pi**2)* ((Dstat**2 - Dres**2) *np.exp(-
(t/tf)**B_f) + Dres**2 * np.exp(-(t/ts)**B_s))
  #integrand_fi1_fi2_1 = lambda t: t* 0.2* (np.pi**2)* ((Dstat**2 - Dres**2) *np.exp(-(t/tf)**B_f) +
Dres**2 * np.exp(-(t/ts)**B_s))
  integrand_fi1_fi2_2 = lambda t: frac_unrelaxed_segment(t, tau_rep, x_c, fi_a, fi_bb)**NMR_alpha *
(2*x_mq-t)* 0.2* (np.pi**2)* (Dres**2 * np.exp(-t/tau_d))
```

```
    f_1 = integration_opt_fi1 (integrand_fi_1, x_mq)
    f_2 = integration_opt_fi2 (integrand_fi_2, x_mq)
    #f_1_check = quad(integrand_fi_1, 0, x_mq)[0]
    #f_2_check = quad(integrand_fi_2, 0, x_mq)[0]
    #print(x_mq," ",f_1, "  ", f_1_check)
    #print(f_2, "  ", f_2_check)
    return 2*(x_mq*f_1 - f_2), (f_2 + quad(integrand_fi1_fi2_2, x_mq, 2*x_mq)[0])
```
and the signal within the function *integral_fit* is measured as follows:
```
for j in range (1,n_tau+1):
        if tau_arm[j] * tail_factor > x_mq[0]:
            fi1_2 , fi1_fi2 = v_integration(x_mq, par[0], tau_arm[j], tau_rep, x_c, fi_a, fi_bb) # V_... is
the vectorized form of the function
            fit_DQ_arm = fit_DQ_arm + np.sinh(fi1_fi2) * np.exp(-fi1_2)/n_tau
            fit_MQ_arm = fit_MQ_arm + (np.exp(fi1_fi2) * np.exp(-fi1_2))/n_tau

        if j < rep_treshold:
            if tau_s[j] * tail_factor > x_mq[0]:
                fi1_2 , fi1_fi2 = v_integration(x_mq, par[0], tau_s[j], tau_rep, x_c, fi_a, fi_bb)
                fit_DQ_bb = fit_DQ_bb + np.sinh(fi1_fi2) * np.exp(-fi1_2)/n_tau
                fit_MQ_bb = fit_MQ_bb + (np.exp(fi1_fi2) * np.exp(-fi1_2))/n_tau

    fi1_2_sum = np.zeros(len(x_mq))
    fi1_fi2_sum = np.zeros(len(x_mq))
    for tt in range(count_rep):
        pp = 2*tt +1
        fi1_2 , fi1_fi2 = v_integration(x_mq, par[0], tau_rep/(pp**2), tau_rep, x_c, fi_a, fi_bb)
        fi1_2_sum = fi1_2_sum + (8/(np.pi**2 * (pp)**2))* fi1_2
        fi1_fi2_sum = fi1_fi2_sum + (8/(np.pi**2 * (pp)**2))* fi1_fi2
```
and this line has to be added to the main code
```
v_integration = np.vectorize(integration)
```

D. Python codes for fitting rheological data

The following code was used for fitting rheological data of the comb-PI sample The code gets the address where the text file (data) is saved. The data is loaded and fit based on the DTD model (time-dependent unrelaxed-segments fraction) then the final results are saved in the same folder.

"
```
import numpy as np
import matplotlib.pyplot as plt
import os
from scipy.optimize import curve_fit, minimize
import os
from scipy.integrate import quadrature, quad
from datetime import datetime
import math
def data_preparation() :
```

```python
    for file in os.listdir(loc):
        if file.endswith(".txt"):
            inputaddress = os.path.join(loc, file)
            namefile = os.path.join(file)
            namefile = namefile[:-4]
            global outputadress
            outputadress = loc +"\\" + namefile + "\\time dependent unrelaxed fraction"
            # READING THE TEXT FILE AND COPY IT TO DATA
            data1 = np.loadtxt(inputaddress)
            data1 = data1[data1.min(axis=1)>=0,:]
    return data1
def R_square (dat, fit_dat):
    return  1-(np.sum((dat - fit_dat)**2) / np.sum(((dat-np.mean(dat))**2)))
def residue (dat, fit_dat):
    return (dat - fit_dat)
def rouse_mode(w, tau_e, Z_a, N):
    rouse_arm_stor = 0
    rouse_arm_loss = 0
    for i in range (1, N):
        if i < int(round(Z_a,0)):
            rouse_arm_stor = rouse_arm_stor + (0.2/Z_a)*(((tau_e*w*Z_a**2)**2)/((tau_e*w*Z_a**2)**2 +
i**4))
            rouse_arm_loss = rouse_arm_loss + (0.2/Z_a)*((tau_e*w*Z_a**2 * i**2)/((tau_e*w*Z_a**2)**2
+ i**4))
        else:
            rouse_arm_stor = rouse_arm_stor + (1/(Z_a))*(((tau_e*w*Z_a**2)**2)/((tau_e*w*Z_a**2)**2 +
4*i**4))
            rouse_arm_loss = rouse_arm_loss + (1/(Z_a))*((tau_e*w*Z_a**2 * i**2 *
2)/((tau_e*w*Z_a**2)**2 + 4*i**4))
    return rouse_arm_stor, rouse_arm_loss


def retraction_mode_arm (w, tau_e, Z_a):
    retrac_arm_stor = 0
    retrac_arm_loss = 0
    for i in range(1, n_tau+1):
        s_a = i/n_tau
        U_a = (15/4)* Z_a* ((1-((1-fi_a*s_a)**(alpha+1))*(1+(1+alpha)*fi_a*s_a)))/(fi_a**2 * (alpha+1) *
(alpha+2))
        tau_early = (225/256)*(np.pi**3) * tau_e* (Z_a* s_a)**4
        tau_late = (np.pi**5 *( 2/15))**0.5 * tau_e * Z_a**1.5* np.exp(U_a)/(s_a * (1-(fi_a*s_a))**alpha)
        tau_arm = (tau_early * np.exp(U_a))/(1+(tau_early*np.exp(U_a)/tau_late))
        relaxation_time_arm[i] = tau_arm
        retrac_arm_stor = retrac_arm_stor + (((tau_arm*w)**2)/((tau_arm*w)**2+1))/n_tau
        retrac_arm_loss = retrac_arm_loss + (((tau_arm*w))/((tau_arm*w)**2+1))/n_tau
    return retrac_arm_stor, retrac_arm_loss
def U_bb_xb(x_b):
    return (1-((1-x_b)**(alpha+1) * (1+(1+alpha)*x_b)))
def diff_1_Ub (x_b, fi_bb, s_b):
    c = 15 *(-((1 + alpha)* (1 - x_b)**(1 + alpha)) + (1 + alpha)* (1 - x_b)**alpha *(1 + (1 + alpha)* x_b))
* fi_bb**alpha * s_b / (8* (1 + alpha)* (2 + alpha))
    return c
```

```
def diff_2_Ub(x_b, fi_bb, s_b):
    c = 15 *(2 *(1 + alpha)**2 *(1 - x_b)**alpha - alpha* (1 + alpha)* (1 - x_b)**(-1 + alpha) *(1 + (1 +
alpha)* x_b))* fi_bb**alpha * s_b/ (8* (1 + alpha)* (2 + alpha))
    return c
def rett_bb(x_b, tau_a_long, p, q, s_b):
    fi_bb = fi_b #* (1- (2/(q+1)))
    #tau_b early in case of lightly branched combs
    #tau_bb_early = 25/64 *(1/(p**2)) * f * s_b**2 * x_b**2 *tau_a_long * fi_bb**(2*alpha)
    tau_bb_early = 375/8192 *(np.pi/(p**2)) * q * s_b**3 * x_b**4 *tau_a_long * fi_bb**(3*alpha)
    U_b = (15*s_b*(fi_bb**alpha)/(8*(1+alpha)*(2+alpha))) * U_bb_xb(x_b)
    tau_bb_late = 25 * s_b**2 * fi_bb**(2*alpha) * q * tau_a_long * np.exp(U_b)*
((2*np.pi/(diff_2_Ub(0, fi_bb, s_b)))**0.5)/(8*p**2 * diff_1_Ub (x_b, fi_bb, s_b))
    return (tau_bb_early * np.exp(U_b))/(1+(tau_bb_early * np.exp(U_b)/tau_bb_late))
def retract_rep_bb (w, tau_e, Z_bb, Z_a, q):
    fi_bb = fi_b #* (1- (2/(q+1)))
    i = 1
    s_a = 1
    p = (12)**-0.5
    U_a = (15/4)* Z_a* ((1-((1-fi_a*s_a)**(alpha+1))*(1+(1+alpha)*fi_a*s_a)))/(fi_a**2 * (alpha+1) *
(alpha+2))
    tau_early = (225/256)*(np.pi**3) * tau_e* (Z_a* s_a)**4
    tau_late = (np.pi**5 *( 2/15))**0.5 * tau_e * Z_a**1.5* np.exp(U_a)/(s_a * (1-(fi_a*s_a))**alpha)
    tau_a_longest = (tau_early * np.exp(U_a))/(1+(tau_early*np.exp(U_a)/tau_late))


    retrac_bb_stor = 0
    retrac_bb_loss = 0
    rep_bb_stor = 0
    rep_bb_loss = 0
    ret_rep = True
    while ret_rep:
        x_bb = i/n_tau
        tau_s = rett_bb(x_bb, tau_a_longest, p , q, Z_bb)
        relaxation_time_clf_bb[i] = tau_s
        tau_rep = (25/(8*np.pi**2 * p**2)) * (1-x_bb)**2 * Z_bb **2 * fi_bb**(2*alpha) * tau_a_longest *
q
        relaxation_time_rep_bb[i] = tau_rep
        if tau_s < tau_rep :
            retrac_bb_stor = retrac_bb_stor + (((tau_s*w)**2)/((tau_s*w)**2+1))
            retrac_bb_loss = retrac_bb_loss + (((tau_s*w))/((tau_s*w)**2+1))
            i = i+1
        else:
            ret_rep = False
        if i == n_tau+1 :
            ret_rep = False
            i=n_tau
    global rep_treshold
    if i!=n_tau :
        x_c = (i-1)/n_tau
        rep_treshold = i
        tau_rep = relaxation_time_rep_bb[rep_treshold]
        for j in range (count_rep):
```

```
        pp = 2*j+1
        rep_bb_stor = rep_bb_stor + ( (8/(np.pi**2 *
(pp)**2))*(((tau_rep*w/(pp)**2))**2)/((tau_rep*w/(pp)**2))**2 + 1)))
        rep_bb_loss = rep_bb_loss + ( (8/(np.pi**2 * (pp)**2))* ((tau_rep*w/ (pp)**2)/((tau_rep*w/
(pp)**2)**2 + 1)))

    return (retrac_bb_stor/n_tau) + (1-x_c)* rep_bb_stor, (retrac_bb_loss/n_tau) + (1-x_c)* rep_bb_loss
def frac_unrelaxed_segment(w, fi_a, fi_bb):
    x_c = (rep_treshold-1)/n_tau
    unrelaxed_fraction = fi_a * relaxed_segments_counter (w, relaxation_time_arm[1:])/n_tau +
fi_bb*(relaxed_segments_counter (w, relaxation_time_clf_bb[1:rep_treshold])/n_tau + (1-x_c))
    return unrelaxed_fraction
def relaxed_segments_counter (w, tau):
    count = np.zeros(len(tau))
    for i in range(len(tau)):
        if w*tau[i] >= 1:
            count[i]= 1 *np.exp(-1/(w*tau[i]))
        else:
            count[i]=np.exp(-1/(w*tau[i]))
    return sum(count)


def combinedFunction_result(comboData, G0_e, G0_N, tau_e, N_e):
    for i in range(n_tau):
        relaxation_time_arm[i] = 0
        relaxation_time_clf_bb[i] = 0
        relaxation_time_rep_bb[i] = 0
    Z_a = N_a/N_e
    Z_bb = N_bb * (1-(2/(q+1))) /N_e
    fi_bb = fi_b #* (1- (2/(q+1)))
    w = comboData[0:length] # first data
    retreac_rep = retract_rep_bb (w, tau_e, Z_bb, Z_a, q)
    rouse_arm = rouse_mode(w, tau_e, Z_a, N_a)
    rouse_bb = rouse_mode(w, tau_e, Z_bb, N_bb)
    retraction_arm = retraction_mode_arm (w, tau_e, Z_a)
    fi_t = v_frac_unrelaxed_segment(w, fi_a, fi_bb)
    result_arm_1 = G0_e* fi_a* rouse_arm[0] + (fi_t**alpha_rheo)* G0_N* retraction_arm[0]
    result_arm_2 = G0_e* fi_a* rouse_arm[1] + (fi_t**alpha_rheo)* G0_N* retraction_arm[1]
    result_bb_1 = G0_e* fi_bb* rouse_bb[0]+ (fi_t**alpha_rheo)* G0_N* retreac_rep[0]
    result_bb_2 = G0_e* fi_bb* rouse_bb[1] + (fi_t**alpha_rheo)* G0_N* retreac_rep[1]
    result1 = (G0_e* fi_a* rouse_arm[0] + G0_e* fi_bb* rouse_bb[0]+ (fi_t**alpha_rheo)* fi_a*
(1+alpha)* G0_N* retraction_arm[0] + (fi_t**alpha_rheo)* fi_bb* (1+alpha)* G0_N* retreac_rep[0])
    result2 = (G0_e* fi_a* rouse_arm[1] + G0_e* fi_bb* rouse_bb[1]+ (fi_t**alpha_rheo)* fi_a*
(1+alpha)* G0_N* retraction_arm[1] + (fi_t**alpha_rheo)* fi_bb* (1+alpha)* G0_N* retreac_rep[1])
    print_data_result(result_arm_1, result_arm_2, result_bb_1, result_bb_2, result1, result2)
    return np.append(result1, result2)


def combinedFunction(comboData, G0_e, G0_N, tau_e, N_e):
    Z_a = N_a/N_e
    Z_bb = N_bb * (1-(2/(q+1))) /N_e
    fi_bb = fi_b #* (1- (2/(q+1)))
    w = comboData[0:length] # first data
```

```python
    #fi_t is the fraction of unrelaxed segments as a function of t
    retreac_rep = retract_rep_bb (w, tau_e, Z_bb, Z_a, q)
    rouse_arm = rouse_mode(w, tau_e, Z_a, N_a)
    rouse_bb = rouse_mode(w, tau_e, Z_bb, N_bb)
    retraction_arm = retraction_mode_arm (w, tau_e, Z_a)
    fi_t = v_frac_unrelaxed_segment(w, fi_a, fi_bb)
    result1 = (G0_e* fi_a* rouse_arm[0] + G0_e* fi_bb* rouse_bb[0]+ (fi_t**alpha_rheo)* (1+alpha)*
fi_a* G0_N* retraction_arm[0] + (fi_t**alpha_rheo)* fi_bb* (1+alpha)* G0_N* retreac_rep[0])
    result2 = (G0_e* fi_a* rouse_arm[1] + G0_e* fi_bb* rouse_bb[1]+ (fi_t**alpha_rheo)* fi_a*
(1+alpha)* G0_N* retraction_arm[1] + (fi_t**alpha_rheo)* fi_bb* (1+alpha)* G0_N* retreac_rep[1])

    return np.append(np.log(result1), np.log(result2))
def combine_data (data_x1, data_y1, data_x2, data_y2):
    combo_x = np.append(data_x1, data_x2)
    combo_y = np.append(data_y1, data_y2)
    return combo_x , combo_y
def print_data_result(result_arm_1, result_arm_2, result_bb_1, result_bb_2, result1, result2):
    f = open(outputadress + "\Result-data-arm.txt","w")
    g = open(outputadress + "\Result-data-bb.txt","w")
    h = open(outputadress + "\Resultdata.txt","w")
    k = open(outputadress + "\Result-relaxation-times-arm-clf-rep.txt","w")
    frc = data1[:,0]
    for i in range (len(frc)):
        print(frc[i], '    ',result_arm_1[i], '    ' , result_arm_2[i], file=f)
        print(frc[i], '    ',result_bb_1[i], '    ' , result_bb_2[i], file=g)
        print(frc[i], '    ',result1[i], '    ' , result2[i], file=h)
    for i in range (n_tau):
        print(relaxation_time_arm[i], '    ',relaxation_time_clf_bb[i], '    ' , relaxation_time_rep_bb[i],
file=k)
    f.close()
    g.close()
    h.close()
    k.close()
def chi_squared (variables):
    G0_1, G0_2, G0_3, Tmed1, Tmed2, Tmed3, sigma1, sigma2, sigma3 = variables
    expec_val = combinedFunction(comboX, G0_1, G0_2, G0_3, Tmed1, Tmed2, Tmed3, sigma1,
sigma2, sigma3)
    return np.sum((comboY-expec_val)**2)
def print_result(fittedParameters,R2_G_stor,  R2_G_loss):
    f = open(outputadress + "\Log-Maxwell-RESULT.txt","a")
    print("fitting at", start_time, file= f)
    print("G0_e: ", fittedParameters[0], '\n', "G0_N: ", fittedParameters[1], file= f)
    print("tau_e: ", fittedParameters[2], '\n', "N_e: ", fittedParameters[3], '\n', file= f)
    print ("R2_G_stor", R2_G_stor, '\t', "R2_G_loss", R2_G_loss, file=f)
    f.close()
def plot_result (X, Y, xx, yy):
    plt.clf()
    plt.plot(X[0:length],Y[0:length], 'k.', X[length:],Y[length:],'r.', xx[0:length], yy[0:length],'c-.',
xx[length:], yy[length:],'c-.' )
    plt.rcParams["legend.fontsize"]= 10
    plt.gca().legend(('storage modulus','loss modulus', 'dynamic dilution model'))
```

```python
    plt.ylabel('modulus(Pa)', fontsize= 8)
    plt.xlabel('angular frequency(w)', fontsize= 8)
    plt.yscale('log')
    plt.xscale('log')
    # ADJUST SAVE FIGURE FILE
    plt.savefig(outputadress +"/" + "Maxwell-model.png", dpi=600)
    plt.clf()
    f = open(outputadress + "\\datafit.txt","w")
    for i in range(length):
        print(X[i], Y[i], Y[i + length], yy[i], yy[i+length], file= f)
    f.close()


def fitting_scipy(frc, G_storage, G_loss):
    if not os.path.exists(outputadress):
        os.makedirs(outputadress)
    global length
    length = len (frc)
    initialParameters = np.array([523284, 352974, 0.0001, 65])
    combo = combine_data (frc, G_storage,frc, G_loss)
    global comboX, comboY
    comboX = combo[0]
    comboY = combo[1]
    bnd= [[0, 0, 0.0000000001, 1],[np.inf, np.inf, 100, 150]]
    # curve fit the combined data to the combined function
    fittedParameters, pcov = curve_fit(combinedFunction, comboX, comboY, initialParameters,
bounds= bnd)
    y_r =(combinedFunction_result(comboX, *fittedParameters) )
    R2_G_stor = R_square (np.exp(comboY[0:length]), y_r[0:length])
    R2_G_loss = R_square (np.exp(comboY[length:]), y_r[length:])
    print_result(fittedParameters,R2_G_stor,  R2_G_loss)
    plot_result (comboX, np.exp(comboY), comboX, y_r)
    print (np.sqrt(np.diag(pcov)))
    return fittedParameters


M_0 = 68.1
M_a = 13800
M_bb = 68000
q = 8.5
N_a = int(round(M_a / M_0,0))
N_bb = int(round(M_bb / M_0,0))
fi_a = 0.633
fi_b = 1 -fi_a
alpha = 4/3
alpha_rheo = 4/3
f = 1
v_frac_unrelaxed_segment = np.vectorize(frac_unrelaxed_segment)
v_retract_rep_bb = np.vectorize(retract_rep_bb)
v_retraction_mode_arm = np.vectorize(retraction_mode_arm)
v_rouse_mode =np.vectorize(rouse_mode)
n_tau = 100
count_rep = 10
```

```
relaxation_time_arm = np.zeros(n_tau+1)
relaxation_time_clf_bb = np.zeros(n_tau+1)
relaxation_time_rep_bb = np.zeros(n_tau+1)
root =2
dist_num = 50
start_time = datetime.now()
loc = input("please give me the address of the folder which contains your data")
data1 = data_preparation()
result = fitting_scipy(data1[:,0], np.log(data1[:,1]),np.log(data1[:,2]))
end_time = datetime.now()
print('Duration: {}'.format(end_time - start_time))
```

References

[1]   D.I. Bower, *An Introduction to Polymer Physics*, American Association of Physics Teachers, 2003.

[2]   R.O. Ebewele. *Polymer Science and Technology*, CRC, Boca Raton, London, 2000.

[3]   D. Feldman, Polymer History. *Designed Monomers and Polymers* 11 (2008) 1–15.

[4]   H. Staudinger, J. Fritschi, Über isopren und kautschuk. 5. Mitteilung. Über die hydrierung des kautschuks und über seine konstitution. *Helvetica Chimica Acta* 5 (1922) 785–806.

[5]   H. Staudinger, Über die Konstitution des Kautschuks (6. Mitteilung). *Berichte der deutschen chemischen Gesellschaft (A and B Series)* 57 (1924) 1203–1208.

[6]   H. Staudinger, On Polymerization, in: A Source Book in Chemistry, 1900-1950, Harvard University Press, 2013, pp. 259–264.

[7]   M.A.-A. AlMa'adeed, I. Krupa, Polyolefin compounds and materials. *Springer Series on Polymer and Composite Materials; Springer: Cham, Switzerland* (2016) 271–284.

[8]   D.W. Sauter, M. Taoufik, C. Boisson, Polyolefins, a Success Story. *Polymers* 9 (2017).

[9]   P.J. Flory. *Principles of Polymer Chemistry*, Cornell University Press, 1953.

[10] P.-G. de Gennes, Reptation of a polymer chain in the presence of fixed obstacles. *The Journal of Chemical Physics* 55 (1971) 572–579.

[11] M. Doi, S.F. Edwards. *The Theory of Polymer Dynamics*, Oxford University Press, 1988.

[12] P.J. FLORY. *Statistical Mechanics of Chain Molecules*, NY, Interscience Publishers, 1969.

[13] M. Dole, History of the irradiation cross-linking of polyethylene. *Journal of Macromolecular Science—Chemistry* 15 (1981) 1403–1409.

[14] A. Charlesby, Cross-linking of polythene by pile radiation. *Proceedings of the Royal Society of London. Series A. Mathematical and Physical Sciences* 215 (1952) 187–214.

[15] H. Meng, G. Li, A review of stimuli-responsive shape memory polymer composites. *Polymer* 54 (2013) 2199–2221.

[16] A. Lendlein, S. Kelch, Shape-memory polymers. *Angewandte Chemie International Edition* 41 (2002) 2034–2057.

[17] C. Liu, H. Qin, P.T. Mather, Review of progress in shape-memory polymers. *Journal of Materials Chemistry* 17 (2007) 1543–1558.

[18] R. Boldt, U. Gohs, U. Wagenknecht, M. Stamm, Effect of electron-induced reactive processing on morphology and structural properties of high-density polyethylene. *Polymer* 95 (2016) 1–8.

[19] R. Boldt, U. Gohs, U. Wagenknecht, M. Stamm, Process-induced morphology and mechanical properties of high-density polyethylene. *Polymer* 136 (2018) 179–186.

[20] H.A. Khonakdar, J. Morshedian, U. Wagenknecht, S.H. Jafari, An investigation of chemical crosslinking effect on properties of high-density polyethylene. *Polymer* 44 (2003) 4301–4309.

[21] J. Thomas, B. Joseph, J.P. Jose, H.J. Maria, P. Main, A. Ali Rahman, B. Francis, Z. Ahmad, S. Thomas, Recent advances in cross-linked polyethylene-based nanocomposites for high voltage engineering applications: a critical review. *Industrial & Engineering Chemistry Research* 58 (2019) 20863–20879.

[22] A.A. Basfar, Flammability of radiation cross-linked low density polyethylene as an insulating material for wire and cable. *Radiation Physics and Chemistry* 63 (2002) 505–508.

[23] Y. Ohki, Development of XLPE-insulated cable for high-voltage dc ubmarine transmission line (1) [News from Japn]. *IEEE Electrical Insulation Magazine* 29 (2013) 65–67.

[24] S. Rouif, Radiation cross-linked polymers: Recent developments and new applications. *Nuclear Instruments and Methods in Physics Research Section B: Beam Interactions with Materials and Atoms* 236 (2005) 68–72.

[25] C. Meola, G.M. Carlomagno, G. Giorleo, Cross-linked polyethylene. *Encyclopedia of Chemical Processing* 1 (2005) 577–588.

[26] P. Pokharel, W. Jian, S. Choi, Evaluation of fatigue crack behavior in electron beam irradiated polyethylene pipes. *Radiation Physics and Chemistry* 126 (2016) 103–110.

References

[27] M.D. Ries, L. Pruitt, Effect of cross-linking on the microstructure and mechanical properties of ultra-high molecular weight polyethylene. *Clinical Orthopaedics and Related Research®* 440 (2005) 149–156.

[28] S.M. Kurtz, O.K. Muratoglu, M. Evans, A.A. Edidin, Advances in the processing, sterilization, and crosslinking of ultra-high molecular weight polyethylene for total joint arthroplasty. *Biomaterials* 20 (1999) 1659–1688.

[29] J.P. Collier, B.H. Currier, F.E. Kennedy, J.H. Currier, G.S. Timmins, S.K. Jackson, R.L. Brewer, Comparison of cross-linked polyethylene materials for orthopaedic applications. *Clinical Orthopaedics and Related Research (1976-2007)* 414 (2003) 289–304.

[30] J.S. Bookman, I.D. Kaye, K.K. Chen, F.F. Jaffe, R. Schwarzkopf, 10-year follow-up wear analysis of marathon highly cross-linked polyethylene in primary total hip arthroplasty. *The Journal of Arthroplasty* 32 (2017) 2587–2589.

[31] E.M. Kampouris, Andreopoulos, AG, Benzoyl peroxide as a crosslinking agent for polyethylene. *Journal of Applied Polymer Science* 34 (1987) 1209–1216.

[32] K.A. Kunert, H. Soszyńska, N. Piślewski, Structural investigation of chemically crosslinked low density polyethylene. *Polymer* 22 (1981) 1355–1360.

[33] S.-Q. Liu, W.-G. Gong, B.-C. Zheng, The effect of peroxide cross-linking on the properties of low-density polyethylene. *Journal of Macromolecular Science, Part B* 53 (2014) 67–77.

[34] W. Zhou, S. Zhu, ESR study of peroxide-induced cross-linking of high density polyethylene. *Macromolecules* 31 (1998) 4335–4341.

[35] M. Liu, C. Zhou, W. Yu, Rheokinetics of the cross-linking of melt polyethylene initiated by peroxide. *Polymer Engineering & Science* 45 (2005) 560–567.

[36] R. Anbarasan, O. Babout, M. Dequiel, B. Maillard, Functionalization and cross-linking of high-density polyethylene in the presence of dicumyl peroxide—An FTIR study. *Journal of Applied Polymer Science* 97 (2005) 766–774.

[37] S. Venkatraman, L. Kleiner, Properties of three types of crosslinked polyethylene. *Advances in Polymer Technology: Journal of the Polymer Processing Institute* 9 (1989) 265–270.

References

[38] D.J. Bullen, G. Capaccio, C.J. Frye, T. Brock, Crosslinking reactions during processing of silane modified polyethylenes. *British Polymer Journal* 21 (1989) 117–123.

[39] M. Narkis, A. Tzur, A. Vaxman, H.G. Fritz, Some properties of silane-grafted moisture-crosslinked polyethylene. *Polymer Engineering & Science* 25 (1985) 857–862.

[40] Atkinson JR, R.Z. Cicek, Silane cross-linked polyethylene for prosthetic applications Part I. Certain physical and mechanical properties related to the nature of the material. *Biomaterials* 4 (1983) 267–275.

[41] J. Barzin, H. Azizi, J. Morshedian, Preparation of silane-grafted and moisture cross-linked low density polyethylene: Part I: Factors affecting performance of grafting and cross-linking. *Polymer-Plastics Technology and Engineering* 45 (2006) 979–983.

[42] Y.-T. Shieh, C.-M. Liu, Silane grafting reactions of LDPE, HDPE, and LLDPE. *Journal of Applied Polymer Science* 74 (1999) 3404–3411.

[43] G.S. Ahmed, M. Gilbert, S. Mainprize, M. Rogerson, FTIR analysis of silane grafted high density polyethylene. *Plastics, Rubber and Composites* 38 (2009) 13–20.

[44] H. Azizi, J. Morshedian, M. Barikani, M.H. Wagner, Correlation between molecular structure parameters and network properties of silane-grafted and moisture cross-linked polyethylenes. *Advances in Polymer Technology: Journal of the Polymer Processing Institute* 30 (2011) 286–300.

[45] Q. Li, T. Chen, L. Sun, W. Guo, C. Wu, Cross-linked ultra-high-molecular-weight polyethylene prepared by silane-induced cross-linking under in situ development of water. *Advances in Polymer Technology: Journal of the Polymer Processing Institute* 37 (2018) 2859–2865.

[46] A.K. Sen, B. Mukherjee, A.S. Bhattacharyya, P.P. De, A.K. Bhowmick, Kinetics of silane grafting and moisture crosslinking of polyethylene and ethylene propylene rubber. *Journal of Applied Polymer Science* 44 (1992) 1153–1164.

[47] R. Salovey, Irradiation of crystalline polyethylene. *Journal of Polymer Science* 61 (1962) 463–473.

References

[48]   R.J. Yan, Y. Luo, B. Jiang, The effect of radiation-induced cross-linking on the relaxation of taut tie molecules during annealing of drawn LDPE. *Journal of Applied Polymer Science* 47 (1993) 789–796.

[49]   E. Oral, O.K. Muratoglu, Radiation cross-linking in ultra-high molecular weight polyethylene for orthopaedic applications. *Nuclear Instruments and Methods in Physics Research Section B: Beam Interactions with Materials and Atoms* 265 (2007) 18–22.

[50]   R. Kitamaru, L. Mandelkern, Irradiation cross linking of polyethylene. The temperature dependence of cross linking in the crystalline and amorphous states. *Journal of the American Chemical Society* 86 (1964) 3529–3534.

[51]   R.M. Black, Effect of temperature upon the cross-linking of polyethylene by high-energy radiation. *Nature* 178 (1956) 305–306.

[52]   H.Y. Kang, O. Saito, M. Dole, The radiation chemistry of polyethylene. IX. temperature coefficient of cross-linking and other effects. *Journal of the American Chemical Society* 89 (1967) 1980–1986.

[53]   A. Charlesby, S. Pinner, Analysis of the solubility behaviour of irradiated polyethylene and other polymers. *Proceedings of the Royal Society of London. Series A. Mathematical and Physical Sciences* 249 (1959) 367–386.

[54]   E.M. Kampouris, Andreopoulos, AG, Gel content determination in cross-linked polyethylene. *Biomaterials* 10 (1989) 206–208.

[55]   A. Smedberg, T. Hjertberg, B. Gustafsson, Effect of molecular structure and topology on network formation in peroxide crosslinked polyethylene. *Polymer* 44 (2003) 3395–3405.

[56]   A. Smedberg, T. Hjertberg, B. Gustafsson, The role of entanglements in network formation in unsaturated low density polyethylene. *Polymer* 45 (2004) 4867–4875.

[57]   H.A. Khonakdar, S.H. Jafari, U. Wagenknecht, D. Jehnichen, Effect of electron-irradiation on cross-link density and crystalline structure of low- and high-density polyethylene. *Radiation Physics and Chemistry* 75 (2006) 78–86.

[58]   J.H. Choi, S.-W. Ko, B.C. Kim, J. Blackwell, W.S. Lyoo, Phase behavior and physical gelation of high molecular weight syndiotactic poly (vinyl alcohol) solution. *Macromolecules* 34 (2001) 2964–2972.

[59] F. Liu, F. Li, G. Deng, Y. Chen, B. Zhang, J. Zhang, C.-Y. Liu, Rheological images of dynamic covalent polymer networks and mechanisms behind mechanical and self-healing properties. *Macromolecules* 45 (2012) 1636–1645.

[60] T. Nicolai, H. Randrianantoandro, F. Prochazka, D. Durand, Viscoelastic relaxation of polyurethane at different stages of the gel formation. 2. sol− gel transition dynamics. *Macromolecules* 30 (1997) 5897–5904.

[61] M.E. de Rosa, H.H. Winter, The effect of entanglements on the rheological behavior of polybutadiene critical gels. *Rheologica acta* 33 (1994) 220–237.

[62] E.M. Vallés, J.M. Carella, H.H. Winter, M. Baumgaertel, Gelation of a radiation crosslinked model polyethylene. *Rheologica acta* 29 (1990) 535–542.

[63] M. Mours, H.H. Winter, Relaxation Patterns of Nearly Critical Gels. *Macromolecules* 29 (1996) 7221–7229.

[64] C.P. Lusignan, T.H. Mourey, J.C. Wilson, R.H. Colby, Viscoelasticity of randomly branched polymers in the vulcanization class. *Physical review. E* 60 (1999) 5657–5669.

[65] S.T. Milner, T.C.B. McLeish, Arm-Length Dependence of Stress Relaxation in Star Polymer Melts. *Macromolecules* 31 (1998) 7479–7482.

[66] S.T. Milner, T.C. McLeish, Parameter-free theory for stress relaxation in star polymer melts. *Macromolecules* 30 (1997) 2159–2166.

[67] A.L. Frischknecht, S.T. Milner, A. Pryke, R.N. Young, R. Hawkins, T.C.B. McLeish, Rheology of three-arm asymmetric star polymer melts. *Macromolecules* 35 (2002) 4801–4820.

[68] J.H. Lee, L.J. Fetters, L.A. Archer, Branch-point motion in asymmetric star polymers. *Macromolecules* 38 (2005) 4484–4494.

[69] Daniels, T.C. McLeish, B.J. Crosby, R.N. Young, C.M. Fernyhough, Molecular rheology of comb polymer melts. 1. Linear viscoelastic response. *Macromolecules* 34 (2001) 7025–7033.

[70] M. Kapnistos, D. Vlassopoulos, J. Roovers, L.G. Leal, Linear rheology of architecturally complex macromolecules: Comb polymers with linear backbones. *Macromolecules* 38 (2005) 7852–7862.

[71] M. Kapnistos, G. Koutalas, N. Hadjichristidis, J. Roovers, D.J. Lohse, D. Vlassopoulos, Linear rheology of comb polymers with star-like backbones: Melts and solutions. *Rheologica Acta* 46 (2006) 273–286.

[72] N.J. Inkson, R.S. Graham, T.C. McLeish, D.J. Groves, C.M. Fernyhough, Viscoelasticity of monodisperse comb polymer melts. *Macromolecules* 39 (2006) 4217–4227.

[73] T.C. McLeish, J. Allgaier, D.K. Bick, G. Bishko, P. Biswas, R. Blackwell, B. Blottiere, N. Clarke, B. Gibbs, D.J. Groves, Dynamics of entangled H-polymers: Theory, rheology, and neutron-scattering. *Macromolecules* 32 (1999) 6734–6758.

[74] D.R. Daniels, T.C.B. McLeish, R. Kant, B.J. Crosby, R.N. Young, A. Pryke, J. Allgaier, D.J. Groves, R.J. Hawkins, Linear rheology of diluted linear, star and model long chain branched polymer melts. *Rheologica Acta* 40 (2001) 403–415.

[75] E. van Ruymbeke, K. Orfanou, M. Kapnistos, H. Iatrou, M. Pitsikalis, N. Hadjichristidis, D.J. Lohse, D. Vlassopoulos, Entangled dendritic polymers and beyond: Rheology of symmetric Cayley-tree polymers and macromolecular self-assemblies. *Macromolecules* 40 (2007) 5941–5952.

[76] R.J. Blackwell, O.G. Harlen, T.C.B. McLeish, Theoretical linear and nonlinear rheology of symmetric treelike polymer melts. *Macromolecules* 34 (2001) 2579–2596.

[77] H. Watanabe, Y. Matsumiya, E. van Ruymbeke, D. Vlassopoulos, N. Hadjichristidis, Viscoelastic and dielectric relaxation of a Cayley-tree-type polyisoprene: Test of molecular picture of dynamic tube dilation. *Macromolecules* 41 (2008) 6110–6124.

[78] S.T. Milner, T.C. McLeish, R.N. Young, A. Hakiki, J.M. Johnson, Dynamic dilution, constraint-release, and star− linear blends. *Macromolecules* 31 (1998) 9345–9353.

[79] J.H. Lee, L.J. Fetters, L.A. Archer, A.F. Halasa, Tube dynamics in binary polymer blends. *Macromolecules* 38 (2005) 3917–3932.

[80] Z. Wang, X. Chen, R.G. Larson, Comparing tube models for predicting the linear rheology of branched polymer melts. *Journal of Rheology* 54 (2010) 223–260.

[81] A. Jurkiewicz, J. Tritt-Goc, N. Piślewski, K.A. Kunert, N.m.r. study of molecular dynamics in chemically crosslinked polyethylene. *Polymer* 26 (1985) 557–560.

[82] K. Saalwächter, B. Herrero, M.A. López-Manchado, Chain order and cross-link density of elastomers as investigated by proton multiple-quantum NMR. *Macromolecules* 38 (2005) 9650–9660.

[83] K. SAALWACHTER, Proton multiple-quantum NMR for the study of chain dynamics and structural constraints in polymeric soft materials. *Progress in Nuclear Magnetic Resonance Spectroscopy* 51 (2007) 1–35.

[84] W. Chassé, J. López Valentín, G.D. Genesky, C. Cohen, K. Saalwächter, Precise dipolar coupling constant distribution analysis in proton multiple-quantum NMR of elastomers. *The Journal of Chemical Physics* 134 (2011) 44907.

[85] J.L. Valentín, J. Carretero-González, I. Mora-Barrantes, W. Chassé, K. SAALWACHTER, Uncertainties in the determination of cross-link density by equilibrium swelling experiments in natural rubber. *Macromolecules* 41 (2008) 4717–4729.

[86] W. Chasse, M. Lang, J.-U. Sommer, K. Saalwachter, Cross-link density estimation of PDMS networks with precise consideration of networks defects. *Macromolecules* 45 (2012) 899–912.

[87] F. Lange, K. Schwenke, M. Kurakazu, Y. Akagi, U. Chung, M. Lang, J.-U. Sommer, T. Sakai, K. Saalwächter, Connectivity and Structural Defects in Model Hydrogels: A Combined Proton NMR and Monte Carlo Simulation Study. *Macromolecules* 44 (2011) 9666–9674.

[88] K. Saalwächter, A. Heuer, Chain Dynamics in Elastomers As Investigated by Proton Multiple-Quantum NMR. *Macromolecules* 39 (2006) 3291–3303.

[89] F. Vaca Chávez, K. Saalwächter, NMR observation of entangled polymer dynamics: tube model predictions and constraint release. *Physical Review Letters* 104 (2010) 198305.

[90] F. Vaca Chávez, K. Saalwächter, Time-Domain NMR Observation of Entangled Polymer Dynamics: Universal Behavior of Flexible Homopolymers and Applicability of the Tube Model. *Macromolecules* 44 (2011) 1549–1559.

[91] M.-L. Trutschel, A. Mordvinkin, F. Furtado, L. Willner, K. Saalwächter, Time-domain NMR observation of entangled polymer dynamics: Focus on all tube-model regimes, chain center, and matrix effects. *Macromolecules* 51 (2018) 4108–4117.

References

[92] A. Mordvinkin, D. Döhler, W.H. Binder, R.H. Colby, K. Saalwächter, Terminal Flow of Cluster-Forming Supramolecular Polymer Networks: Single-Chain Relaxation or Micelle Reorganization? *Physical Review Letters* 125 (2020) 127801.

[93] A. Mordvinkin, M. Suckow, F. Böhme, R.H. Colby, C. Creton, K. Saalwächter, Hierarchical sticker and sticky chain dynamics in self-healing butyl rubber ionomers. *Macromolecules* 52 (2019) 4169–4184.

[94] F. Shahsavan, M. Beiner, K. Saalwächter, Chain dynamics in partially cross-linked polyethylene by combined rheology and NMR-based molecular rheology. *Journal of Polymer Science* 60 (2022) 1266–1276.

[95] G.R. Strobl. *The Physics of Polymers*, Springer, 1997.

[96] H.B. Bohidar. *Fundamentals of Polymer Physics and Molecular Biophysics*, Cambridge University Press, 2015.

[97] U.L. Gedde. *Polymer Physics*, Springer Science & Business Media, 1995.

[98] L.H. Sperling. *Introduction to Physical Polymer Science*, John Wiley & Sons, 2005.

[99] P.E. Rouse Jr, A theory of the linear viscoelastic properties of dilute solutions of coiling polymers. *The Journal of Chemical Physics* 21 (1953) 1272–1280.

[100] M. Rubinstein, R.H. Colby. *Polymer Physics*, Oxford University Press New York, 2003.

[101] R.C. Ball, P.T. Callaghan, E.T. Samulski, A simplified approach to the interpretation of nuclear spin correlations in entangled polymeric liquids. *The Journal of Chemical Physics* 106 (1997) 7352–7361.

[102] R.C. Ball, T.C. McLeish, Dynamic dilution and the viscosity of star-polymer melts. *Macromolecules* 22 (1989) 1911–1913.

[103] D.S. Pearson, E. Helfand, Viscoelastic properties of star-shaped polymers. *Macromolecules* 17 (1984) 888–895.

[104] M. Rubinstein, R.H. Colby, Gillmor JR, Space-Time Organization in Macromolecular Fluids. *Tanaka, F., Doi, M., Ohta, T., Eds* (1989) 66.

[105] C. Das, N.J. Inkson, D.J. Read, M.A. Kelmanson, T.C.B. McLeish, Computational linear rheology of general branch-on-branch polymers. *Journal of Rheology* 50 (2006) 207–234.

[106] R.G. Larson, T. Sridhar, L.G. Leal, G.H. McKinley, A.E. Likhtman, T.C. McLeish, Definitions of entanglement spacing and time constants in the tube model. *Journal of Rheology* 47 (2003) 809–818.

[107] A.E. Likhtman, T.C.B. McLeish, Quantitative theory for linear dynamics of linear entangled polymers. *Macromolecules* 35 (2002) 6332–6343.

[108] F. Chambon, H.H. Winter, Linear viscoelasticity at the gel point of a crosslinking PDMS with imbalanced stoichiometry. *Journal of Rheology* 31 (1987) 683–697.

[109] H.H. Winter, F. Chambon, Analysis of linear viscoelasticity of a crosslinking polymer at the gel point. *Journal of Rheology* 30 (1986) 367–382.

[110] M. Daoud, Distribution of relaxation times near the gelation threshold. *Journal of Physics A: Mathematical and General* 21 (1988) L973.

[111] J.E. Martin, D. Adolf, J.P. Wilcoxon, Viscoelasticity near the sol-gel transition. *Physical Review A* 39 (1989) 1325.

[112] H.H. Winter, Evolution of rheology during chemical gelation, in: Permanent and Transient Networks, Springer, 1987, pp. 104–110.

[113] M. Rubinstein, R.H. Colby, J.R. Gillmor, Dynamic scaling for polymer gelation. *American Chemical Society, Polymer Preprints, Division of Polymer Chemistry* 30 (1989) 81–82.

[114] H.H. Winter, M. Mours, Rheology of polymers near liquid-solid transitions. *Neutron spin echo spectroscopy viscoelasticity rheology* (1997) 165–234.

[115] C.P. Lusignan, T.H. Mourey, J.C. Wilson, R.H. Colby, Viscoelasticity of randomly branched polymers in the critical percolation class. *Physical Review E* 52 (1995) 6271.

[116] R.H. Colby, J.R. Gillmor, M. Rubinstein, Dynamics of near-critical polymer gels. *Physical Review E* 48 (1993) 3712.

[117] D. Durand, M. Delsanti, M. Adam, J.M. Luck, Frequency dependence of viscoelastic properties of branched polymers near gelation threshold. *EPL (Europhysics Letters)* 3 (1987) 297.

[118] D. Adolf, J.E. Martin, Time-cure superposition during crosslinking. *Macromolecules* 23 (1990) 3700–3704.

[119] D. Adolf, J.E. Martin, J.P. Wilcoxon, Evolution of structure and viscoelasticity in an epoxy near the sol-gel transition. *Macromolecules* 23 (1990) 527–531.

[120] H. Gunther. *NMR Spectroscopy: An Introduction*, Wiley Chichester, 1980.

[121] M.H. Levitt. *Spin Dynamics: Basics of Nuclear Magnetic Resonance*, John Wiley & Sons, 2013.

[122] J. Keeler. *Understanding NMR Spectroscopy*, John Wiley & Sons, 2010.

[123] M.J. Duer. *Solid State NMR Spectroscopy: Principles And Applications*, John Wiley & Sons, 2008.

[124] K. Saalwächter, H.W. Spiess, 2.07 Solid-State NMR of Polymers, in: Reference Module in Materials Science and Materials Engineering. Polymer Science: A Comprehensive Reference, Elsevier, 2012, pp. 185–219.

[125] K. Schäler, M. Roos, P. Micke, Y. Golitsyn, A. Seidlitz, T. Thurn-Albrecht, H. Schneider, G. Hempel, K. Saalwächter, Basic principles of static proton low-resolution spin diffusion NMR in nanophase-separated materials with mobility contrast. *Solid state nuclear magnetic resonance* 72 (2015) 50–63.

[126] J. Baum, A. Pines, NMR studies of clustering in solids. *Journal of the American Chemical Society* 108 (1986) 7447–7454.

[127] K. Saalwächter, P. Ziegler, O. Spyckerelle, B. Haidar, A. Vidal, J.-U. Sommer, 1 H multiple-quantum nuclear magnetic resonance investigations of molecular order distributions in poly (dimethylsiloxane) networks: Evidence for a linear mixing law in bimodal systems. *The Journal of Chemical Physics* 119 (2003) 3468–3482.

[128] P.-W. Anderson, P.R. Weiss, Exchange narrowing in paramagnetic resonance. *Reviews of Modern Physics* 25 (1953) 269.

[129] R. Kimmich. *NMR: Tomography, Diffusometry, Relaxometry*, Springer Science & Business Media, 2012.

[130] K. Saalwächter, 1 H multiple-quantum nuclear magnetic resonance investigations of molecular order in polymer networks. II. Intensity decay and restricted slow dynamics. *The Journal of Chemical Physics* 120 (2004) 454–464.

[131] K. Saalwächter, M. Klüppel, H. Luo, H. Schneider, Chain order in filled SBR elastomers: a proton multiple-quantum NMR study. *Applied Magnetic Resonance* 27 (2004) 401.

[132] K. Saalwächter, F. Kleinschmidt, J.-U. Sommer, Swelling heterogeneities in end-linked model networks: a combined proton multiple-quantum NMR and computer simulation study. *Macromolecules* 37 (2004) 8556–8568.

[133] Z. Wang, A.E. Likhtman, R.G. Larson, Segmental dynamics in entangled linear polymer melts. *Macromolecules* 45 (2012) 3557–3570.

[134] A. Mordvinkin, K. Saalwächter, Microscopic observation of the segmental orientation autocorrelation function for entangled and constrained polymer chains. *The Journal of Chemical Physics* 146 (2017) 94902.

[135] I.V. Brekotkin, N.F. Fatkullin, K. Lindt, C. Mattea, S. Stapf, On the theory of the spin I = 1/2 double quantum NMR: Effects of spins spatial displacements between RF pulses. *The Journal of Chemical Physics* 157 (2022) 224108.

[136] M. Lang, J.-U. Sommer, Analysis of entanglement length and segmental order parameter in polymer networks. *Physical Review Letters* 104 (2010) 177801.

[137] J.H. Lee, L.J. Fetters, L.A. Archer, Stress relaxation of branched polymers. *Macromolecules* 38 (2005) 10763–10771.

[138] H. Mitsui, F. Hosoi, T. Kagiya, γ-radiation-induced cross-linking of polyethylene. *Polymer journal* 4 (1973) 79–86.

[139] A. Singh, Irradiation of polyethylene: Some aspects of crosslinking and oxidative degradation. *Radiation Physics and Chemistry* 56 (1999) 375–380.

[140] G.N. Patel, A. Keller, Crystallinity and the effect of ionizing radiation in polyethylene. II. Crosslinking in chain-folded single crystals. *Journal of Polymer Science: Polymer Physics Edition* 13 (1975) 323–331.

[141] A. Vieyres, R. Pérez-Aparicio, P.-A. Albouy, O. Sanseau, K. Saalwächter, D.R. Long, P. Sotta, Sulfur-cured natural rubber elastomer networks: correlating cross-link density, chain orientation, and mechanical response by combined techniques. *Macromolecules* 46 (2013) 889–899.

[142] L.J. Tung, S. Buckser, The effects of molecular weight on the crystallinity of polyethylene. *The Journal of Physical Chemistry* 62 (1958) 1530–1534.

[143] L. Mandelkern, The effect of molecular weight on the crystallization, melting, and morphology of long-chain molecules, Journal of Polymer Science: Part C 15 (1967) 129–162.

[144] S.J. Park, S. Shanbhag, R.G. Larson, A hierarchical algorithm for predicting the linear viscoelastic properties of polymer melts with long-chain branching. *Rheologica Acta* 44 (2005) 319–330.

[145] R.G. Larson, Combinatorial rheology of branched polymer melts. *Macromolecules* 34 (2001) 4556–4571.

Erklärung

Hiermit versichere ich, die vorliegende Arbeit selbstständig und ohne fremde Hilfe verfasst und keine anderen als die von mir angegeben Quellen und Hilfsmittel verwendet zu haben. Die den benutzten Werken wörtlich oder inhaltlich entnommenen Stellen habe ich als solche kenntlich gemacht.

Ich erkläre, keine anderweitigen Promotionsversuche unternommen und die vorliegende issertation weder in der jetzigen noch in einer anderen Fassung einer anderen wissenschaftlichen Einrichtung vorgelegt zu haben.

Halle (Saale), den

Farhad Shahsavan

Acknowledgements

List of Publications

1. F. Shahsavan, M. Beiner, K. Saalwächter, Chain dynamics in partially cross-linked polyethylene by combined rheology and NMR-based molecular rheology. *Journal of Polymer Science* 60 (2022) 1266–1276.

Curriculum vitae

Personal data

Family name:	Shahsavan
First name:	Farhad
Date of birth:	21.05.1988
Place of birth:	Tehran
Nationality:	Iranian

Education

10/2017-present	Doctoral studies Martin-Luther Universtität Halle-Wittenberg Institute of Physics (NMR group)
9/2011 – 10/2013	Master of Science in polymer engineering AMIRKABIR University of Technology, Tehran
9/2006 – 4/2011	Bachelor of Science in polymer engineering AMIRKABIR University of Technology, Tehran
9/1999-7/2006	NODET(National organization department of exceptional talents) School, Karaj

Work experience

10/2017-present	Research assistant Martin-Luther Universtität Halle-Wittenberg
1/2016 – 5/2017	Process engineer Daryasahel Co., Tehran

Halle (Saale), den   Farhad Shahsavan